Acoustic Modelling of Bat Pinnae Utilising the TLM method

by

Gordon Leonard, B. Eng(Hons) DIS.

A Doctoral Thesis submitted in partial fulfilment of the requirements

for the award of

Doctor of Philosophy of Loughborough University

October 2006

To my mum and dad

ABSTRACT

THIS thesis describes the numerical modelling of bioacoustic structures, the focus being the outer ear or *pinnae* of the Rufous Horseshoe bat (*Rhinolophus rouxii*).

There have been several novel developments derived from this work including:

- A method of calculating directionality based on the sphere with a distribution of measuring points such that each lies in an equal area segment.
- Performance estimation of the pinna by considering the directionality of an equivalent radiating aperture.
- A simple synthetic geometry that appears to give similar performance to a bat pinna.

The outcome of applying the methods have yielded results that agree with measurements, indeed, this work is the first time TLM has been applied to a structure of this kind. It paves the way towards a greater understanding of bioacoustics and ultimately towards generating synthetic structures that can perform as well as those found in the natural world.

ACKNOWLEDGEMENTS

First and foremost I have to give huge thanks to my primary supervisor, Dr James Flint for agreeing to take me on as a research student and lend me his expertise and experience while successfully guiding me through my PhD.

There have been many other academic members of staff who have given me encouragement and passed on their knowledge. These included; Dr Paul Lepper, Dr Simon Pomeroy, Prof Bryan Woodward, Dr Sekharjit Datta, Dr Andrew Armstrong and last but no means least David Goodson with whom I had the pleasure of working with during the first year of my studies, he is greatly missed.

The measurements could not have been achieved without Graham Tromans and Dr Guy Bingham from Mechanical Engineering to whom we are grateful for manufacturing the test pinna specimens. Gratitude is also expressed to Dr Rolf Muller and the CIRCE project who supplied data which made the project possible.

Thanks must be passed on to fellow research students who have assisted me with various aspects of the project; Simon Dible, Steven Beesley, Trevor Rawlings, Dr Emmanuel Touloupis and Douglas Rankin.

On a personal note, I would like to thank my mum and dad for supporting me throughout my undergraduate and postgraduate days at Loughborough University and to Laura Elliott for the continued encouragement she gave me whilst writing up.

Final acknowledgement must go to the Electronic and Electrical Engineering Department of Loughborough University for funding the work.

CONTENTS

LIST OF ABBREVIATIONS AND SYMBOLS

CIRCUIT THEORY AND TLM NOTATION

Symbol	Denotes
C	Capacitance (F)
G	Conductance (S)
Γ	Acoustical reflection coefficient
$\hat{G}_s$	Normalised characteristic conductance $= \frac{G_s}{G_o}$
$\mathrm{I}_x, \mathrm{I}_y, \mathrm{I}_z$	Axial current (A)
k	Time step iteration number
$\delta\ell$	Unit length of lumped transmission line (m)
$\Delta\ell$	Node separation (m)
L	Inductance (H)
R	Resistance (Ω)
S	Scatter matrix
t	Time (s)
δt	Time step (s)
$\mathrm{u}_x, \mathrm{u}_y, \mathrm{u}_z$	Axial particle velocity (m s^{-1})
V_z	Total voltage on a node (V)
${}^{i}V$	Incident voltage (V)
ρ	Reflection coefficient (voltage or pressure, depending on context)
${}^{r}V$	Reflected voltage (V)
x, y, z	Axial distances along the transmission line (m)
$\hat{Y}_s$	Normalised characteristic admittance $= \frac{Y_s}{Y_0}$
Z	Impedence (Ω)
Z_o	Characteristic impedance (Ω)
Z_{TL}	Transmission line impedance (Ω)

ACOUSTICS, THE PHYSICAL PROPERTIES OF MATERIALS, AND WAVES

Symbol	Denotes
a, d, c	Geometrical shape dimensions (m)
(BW_ϕ)	Azimuthal beamwidth (radians, unless stated otherwise)
(BW_θ)	Elevation beamwidth (radians, unless stated otherwise)
c	Speed of sound in air ≈ 331.4 m s^{-1}
d	Distance (m)
$d(\theta)$	Elevation directionality (radians, unless stated otherwise)
dB	Decibel
f	Frequency (Hz)
f_{max}	Cutoff frequency (Hz)
k	Wavenumber (m^{-1})
L	Length of radiating source (m)
λ	Wavelength (m)
l,m,n	Mode indices
P	Acoustic pressure (Pa)
P_{max}	Maximum pressure of a source (Pa)
Z_A	Acoustic impedance. 410 Ns m^{-3} in air
ρ	Equilibrium density. 1 2 kg m^{-3} in air
σ	Coefficient of compressibility. 7.65×10^{-6} m^2 N^{-1} in air
ω	Angular frequency $=2\pi$ f (rads s^{-1})
μ	Permeability (H m^{-1})
ε	Permittivity (dielectric constant, F m^{-1})

MATHEMATICS

Symbol	Denotes
A	Amplitude of Gaussian signal
σ	Standard deviation

ABBREVIATIONS

Abbreviation	Expansion
ABC	Absorbing boundary condition
BEM	Boundary element method
CF	Constant frequency
CIRCE	Chiroptera Inspired Robotic CEphaloid
CNC	Computerised numerically controlled
CT	Computer tomography
DI	Directionality index
DFT	Discrete Fourier transform
DRL	Defence research labratory (US)
FDM	Fused deposition modelling
FDTD	Finite element time domain
FEA	Finite element analysis
FFT	Fast Fourier transform
FM	Frequency modulated
HRTF	Head related transfer function
IAD	Interaural amplitude difference
IID	Interaural intensity difference
IST	Information society technologies
ITD	Interaural time difference
LOM	Laminated object manufacturing
MLDB	Monkey lips/dorsal bursae
NFFF	Near to far field transformation
PML	Perfectly match layer
PPM	Portable pixel map
RMRG	Rapid manufacturing research group
RP	Rapid prototyping
SCN	Symetrical condensed node
SONAR	Sound navigation and ranging
STL	Stereolithography
VTK	Visualization toolkit

LIST OF FIGURES

LIST OF TABLES

CHAPTER 1:
INTRODUCTION

ACOUSTICS is the study of sound generation, transmission and wave interaction with objects. There are many applications of acoustic theory ranging from simple transducer design for audible sound generation (e.g. a car horn) to significantly more complex systems capable of imaging (e.g. ultrasonic imaging of unborn babies). This thesis focuses on a particular application which has been exploited in the animal kingdom - echolocation.

1.1 Utilising acoustics

Echolocation is a process where the portion of an object can be detected by means of measuring the wave which reflects from it. One mechanism for generating this reflection (or echo) is due to an impedance mismatch in the wave propagation medium.

$$Z = \rho c \tag{1.1}$$

Equation 1.1 describes the acoustic impedance (Z in Ns m^{-3}) of a material where ρ is the density in kg m^{-3} and c is the speed of sound through that material in m s^{-1}. Equation 1.2 shows the reflection coefficient (Γ), which describes the fraction of original acoustical energy that will reflect compared to the amount that will pass through the boundary (Equation1.3 τ) between two different materials, where Z_1 and Z_2 represent the impedance of each material. Figure 1.1 graphically represents the aforementioned situation.

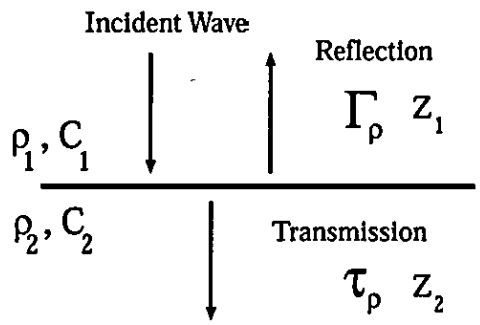

Figure 1 1: Visualisation of wave transmission between two different materials

$$\Gamma = \frac{1 - Z_1}{1 + Z_2} \tag{1.2}$$

$$\tau = \frac{2Z_2}{Z_1 + Z_2} \tag{1.3}$$

The most common boundary interface considered in airborne ultrasonics is when the impedance of the transmission medium increases, i.e. $Z_2 \rightarrow \infty$. When $\Gamma = +1$ there is total reflection of the sound wave in the same phase, if $\Gamma = -1$ there is total reflection in anti-phase. When $-1 < \Gamma < +1$ there is partial transmission and reflection at the boundary. Ultrasonography is a further adaptation of this phenomena and utilises the determination of the reflection coefficient (the partial transmission) to show the change in acoustic impedance. This could be to scan an unborn baby as previously mentioned or to detect flaws in rail tracks. This remains true both in the synthetic and natural world where marine mammals have particularly well developed echolocation systems. Dolphins have the ability to determine the difference between cylinders of varying thicknesses [1.1] and identical objects made of different materials [1.2]. Both of these phenomena rely on more than just the detection of a simple reflection. Bats also use echolocation, with a particularly wide variety of techniques that will be detailed in the next chapter. It has been shown how these animals can discriminate between objects separated by three tenths of a millimeter [1.3] which is where human systems aspire

to. There are many other interesting features of bat echolocation systems that will be considered in this thesis.

1.1.1 Numerically modelling acoustics

Numerical modelling provides an efficient method for investigating the performance of hypothetical systems designed by engineers before they are actually built. It can also be used to simulate existing systems such as biological ones in an attempt to understand and recreate them. One of the earliest examples of full wave based numerical modelling in underwater acoustics dates back to 1960 [1.4] when much early work was driven by defence applications. Researchers in these areas, such as anti-submarine warfare (ASW) have modelled typical situations and been able to investigate sound propagation in varying meteorological conditions [1 4] not always available in laboratory facilities.

Modelling more complex and large systems has become possible through the development of digital computers as they have the ability to solve the huge number of necessary calculations. Computers have also made it easier to analyse the results through visual representations with the ability to quickly plot graphs and complex 3D images being invaluable.

Ray-based methods were the most popular techniques used for modelling in the early 1960's [1.5]. Currently the method has fallen out of favour due to inaccuracies at higher frequencies although it is still a popular method for acquiring quick results in simple situations. Volume element methods are currently very popular due to computer technology and the availability of commercial software which can be used in many fields whether it be wave based modelling or structural analysis.

1.2 Objectives

The aims of this thesis is to implement acoustical transmission line matrix modelling (TLM) for investigating the receiving properties of bat pinnae (the outer ear). Work

is currently being undertaken by the CIRCE (Chiroptera Inspired Robotic CEphaloid, see Chapter 2.2) project who's main objective is to produce a life sized, working synthetic bat head. One particular aspect of the project is understanding the pinna and how its shape and operating parameters effect the complete echolocation system. Typical artificial SONAR (SOund Navigation And Ranging) systems use arrays of transducers for receiving sound rather than baffle type receivers. These arrays take up space, add weight to the system and rely on signal processing on each individual transducer to detect sound. The use of a baffle to replace this array could have many advantages including the reduction of cost, processing time and system complexity. From the investigation of the biological baffle the aim is to understand why the pinna is the shape it is and how it can be synthesized for use in a human made systems. Directional properties of the pinna such as directionality index (DI) and beamwidth will be measured and examined for results not explainable by way of traditional analytical theory.

1.3 Thesis Overview

Chapter 2 introduces the bat as a flying mammal with a highly complex echolocation system that is far superior to any human made SONAR system. It also introduces and discusses several numerical modelling techniques and various properties used to quantify the pinnas performance.

Chapter 3 introduces the TLM method and how it has been developed and implemented in the acoustic domain and provides validation exercises including a brief study of the Harbour Porpoise melon; the only other application of TLM to non-human acoustic sensory systems.

Chapter 4 examines far field acoustics and explains the near to far field (NFFF) transformation for use in conjunction with TLM generated near field results. There are validation exercises and a discussion into the parameters used to describe the recep-

tion performance of the pinna. There is a novel alternative to calculating directionality introduced, and validation exercises performed to demonstrate its feasibility.

Chapter 5 explains how the pinna was modelled using the TLM procedure and presents results which are compared with radiating apertures with similar dimensions. Directionality is visualised by means of 2D polar plots and 3D surfaces which can assist in the estimation of directionality index. It then goes on to detail the measurement apparatus and the procedure used to gather the measurement data.

Chapter 6 discusses approximations to the real pinna shape and its directionality. It analyses acoustical scattering from circular and triangular patches and briefly looks at the electromagnetic case. It then moves on to 3D approximations where the pinna is considered similar in shape and form to an enclosed equilateral triangle wrapped around an imaginary cylinder.

Chapter 7 concludes the findings and proposes further areas of research.

References

[1.1] W. W. L. Au and D. A. Pawloski, "Cylinder wall thickness discrimination by an echolocating dolphin," *Journal of Computational Physiology*, vol. 72, pp. 41–47, 1992.

[1.2] W. W. L. Au and C. W. Turl, "Material composition discrimination of cylinders at different aspect angles by an echolocating dolphin," *Journal of the Acoustical Society of America*, vol. 89, pp. 2448–2451, May 1991.

[1.3] J. A. Simmons, M. J. Ferragamo, and C. F. Moss, "Echo-delay resolution in sonar images of the Big Brown bat," *Proceedings of the National Academy of Sciences*, vol. 95, pp. 12647–12652, 1998.

[1.4] P. C. Etter, *Underwater Acoustic Modeling: Principles, Techniques and Applications*. Elsevier Applied Science, 1991.

[1.5] F. B. Jensen, W. A. Kuperman, M. B. Portor, and H. Schmidt, *Computational Ocean Acoustics*. AIP in Modern Acoustics and Signal Processing, Springer-Verlag, 1993.

CHAPTER 2:

BAT ECHOLOCATION AND NUMERICAL MODELLING

THERE has been much research interest in the performance and functionality of echolocating bats. Some of the major research topics explored include sound production and the received echo processing (typically performed by neuron detectors and determining their interaction with the brain). There has been relatively little research carried out on the "antenna properties" of bat ears or *pinnae*. Historical references in this field include Grinnell and Schnitzler [2.1] who measured the directionality pattern of the pinna of the Greater Horseshoe bat and Jen and Chen [2.2] who examined sound transformation at the pinna of an echolocating bat. To date, there have been few attempts to mathematically model and determine the acoustic properties of the pinna. Aroyan [2 3] and Flint *et al.* [2.4] have however successfully carried out research on marine mammals with numerical techniques.

This chapter overviews bat echolocation and examines some of the modelling methods which are candidates for its study. The performance metrics related to the pinna are also reviewed and related back to the basic theory of antennas.

2.1 Bats

Bats are the only known flying mammals and belong to a species called Chiroptera (Greek for "hand-wing") Most varieties are nocturnal and they are found world wide

dwelling in caves, trees, buildings or almost anything that keeps them protected and sheltered. They eat a wide variety of foods from static objects such as fruit to highly agile prey such as insects and frogs. There are over one thousand species of bats making them the most common of all mammal species and they themselves are split into two sub categories: the megachiroptera and the microchiroptera. As the name suggests megachiroptera are generally the bigger bat and they navigate by sight rather than echolocation, although this is not true in every case. *Rousettus* are the only genus of megachiroptera that have the ability to echolocate [2.5] and they use it to navigate in and around their usual roosting areas such as caves [2.6]. Their echolocation in general is similar to that of the microchiroptera but the clicks are produced by flicking their tongue as opposed to using the larynx. Megachiroptera use sight and smell to find fruit and plants and from this choice of food are responsible for pollinating flowers. Where possible, hunting by microchiroptera bats is performed using a combination of their acute eye sight and SONAR systems; this is usually the case until vision becomes ineffectual in the dark. It has been shown that some bats use sounds produced by prey in order to detect them, in other words a passive approach as opposed to active detection. For example, *Trachops cirrhosus* detects edible frogs from their calls [2.7] and *Plecotus auritus* among other bats rely exclusively on prey generated sounds [2.8]. These bats are also known as *gleaning* bats.

2.1.1 Evolution

Bats and other echolocating animals such as Dolphins have evolved over millions of years. During this time the SONAR systems of the animals have been forced to develop in order to survive in their everchanging environment. Prey themselves have evolved in order to protect themselves from the hunters so the situation turns full circle and the hunters are forced to adapt to overcome these defensive tactics. Factors outside the natural world also affect the animal's need to evolve. An obvious example of this is humans and the way they have affected nearly every aspect of the entire ecosystem. The introduction of human made noise into the natural world is currently of great interest

to scientists and how this noise is disrupting echolocating animals. This is especially true for marine mammals where SONAR systems on ships are constantly introducing artificial noise into the oceans. Recently it has been suggested that a particular variant of human made noise has been responsible for giving beaked whales the "bends" and actually killing the animal [2.9]. It is assumed these changes in animal habitats will give the animals another situation in which they will have to adapt to, unless more laws are passed to protect the animals. It is the evolution that scientists are interested in and the reasons why natural mechanisms, such as echolocation are so effective and functional.

Every functional element of an animal's echolocating system has been perfected over time for a reason. Inadequate elements or actions cost animals time and energy in their quest to survive, hence anything non-beneficial will be overlooked and gradually adapted until they are optimised. This thesis is primarily interested in the particular shape and functionality of the bat pinnae as an acoustic receiver. Bat pinnae between species are different but so is the size of the animal, the prey it consumes and the echolocation technique implemented. From this it can be deduced that collectively all of these factors define what shape the pinna should be. It is up to scientists and engineers to investigate all of these parameters and explain why the echolocation system of the bats is so effective. It is then their goal to try and utilise this functionality and introduce it to synthetic SONAR systems created by humans.

2.1.2 Echolocation

For many years humans observing bats at night and in dark caves speculated as to how they managed to navigate and track prey so accurately. However, it was not really understood until the 1790's when Spallanzani preformed scientific experiments on microchiroptera species concluding sound was a more important factor than sight for navigation. In 1938 Donald Griffin used the first ultrasonic microphone created by an American physicist to solve the mystery of the bat's ability to navigate in the dark and coined the phrase, *echolocation* [2.10].

Figure 2 1· A simple example of echolocation as a bat detects its prey, in this case a moth

Echolocation is the ability to use the reflection of sound from objects to detect them. Sound is emitted from a source and detectors listen for any possible reflection that may occur if it meets a barrier. Figure 2.1 shows the basic principle in its most simplistic form. Knowing the speed of sound ($c, \approx 331$ ms^{-1} in air) in the particular medium and the time taken (t) for an emission launched at $t = 0$ to return to the source, the distance (d) between the source and object can be calculated from the simple expression:

$$d = \frac{1}{2}(c \times t) \tag{2.1}$$

This principle is also applied to the SONAR systems as implemented by marine mammals such as dolphins, submarine detectors used by the Navy, and ultrasound scanners used in hospitals. Sound reflects due to the impedance mismatch between objects of different density, as has already been explained.

2.1.3 Emission type and structure of echolocating bats

The primary species of focus in this thesis is the bat *Rhinolophus rouxii* (Rufous Horseshoe bat Figure 2.2) which is a microchiroptera species and uses echolocation to hunt and navigate in its surroundings. As with the majority of other mammals, microchiroptera bats generate their calls in the larynx. Sound passes over the vocal chords

causing them to vibrate which in turn induces sound. The emission frequency is modulated by tightening and relaxing the muscles around them. The click is then projected into space via the mouth or nostrils which have developed with the growth of large skin folds and cartilage. These adapted nostril are termed *noseleaves*. It has been suggested [2.6] that these act to beamform the sound rather like the melon in the head of Cetaceans [2.11]. This increases the directionality of the call increasing the sound pressure in a desired direction.

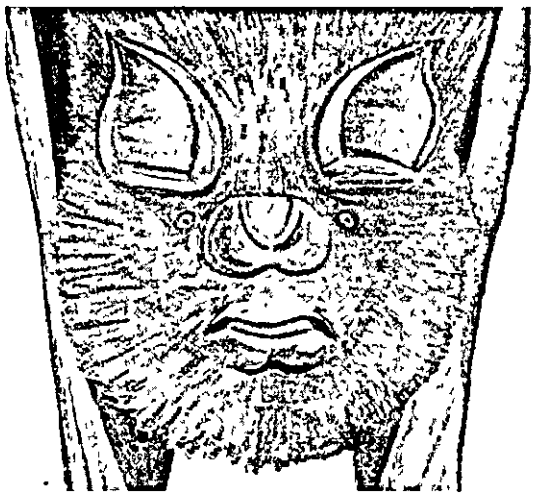

Figure 2.2: The Rufous Horseshoe bat (*Rhinolophus rouxii* (adapted from Altringham [2.6]))

Bats emit sound in pulses which are either narrowband, constant frequency (CF) or broadband, frequency modulated (FM) types. Some animals use a combination of the two- being termed CF-FM bats. An FM pulse sweeps through a range of frequencies and is of short duration so the returning echo does not interfere with the next emitted click. Figure 2 3 shows an example of an FM sweep signal from a *Pipistrellus pipistrellus* with two higher frequency harmonics. These harmonics are expected because pure tone emissions are very rare in the natural world. FM sweeps are particularly useful for 3D imaging of cluttered environments and will give a better definition of the target than CF [2.6]. This is achieved by broadening the bandwidth of the signal either by increasing the frequency sweep spectrum using modulation or adding harmonics by using a broadband signal. Whether sound bends around an object or reflects off it depends on

the wavelength of the sound compared to the object size. In general, higher frequencies (shorter wavelengths) will reflect off smaller objects than lower frequencies, hence the improved resolution in target detection. The disadvantage with this phenomena is that higher frequencies tend to be absorbed more in air than lower ones leading to a reduced echolocation range. Another benefit with higher frequencies is that when two or more bats are echolocating in the same region the sound does not travel so far and consequently there will be less interference between bats.

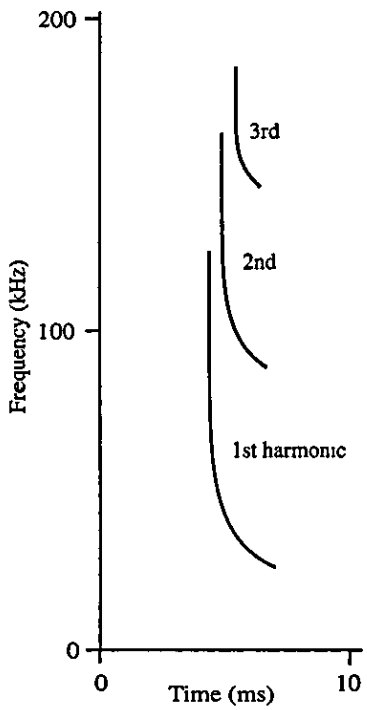

Figure 2.3: FM Sweep of the *Pipistrellus Pipistrellus* adapted from Jones *et al.* [2.12]

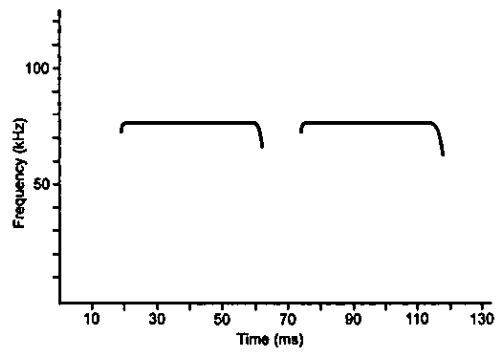

Figure 2.4: CFFM echolocation click of the *Rhinolophus rouxii* showing the CF portion to be approximately 78 kHz

CF calls usually begin, end or are sandwiched between a short FM sweep. Figure 2.4 shows two example clicks from the *Rhinolophus rouxii*, where Neuweiler *et al.* [2.13] measured the CF frequency component to be 79 kHz. Two important features of this type of call is the use of Doppler shift [2.14] to detect and track prey and the ability to examine their target's wing beat and structure [2.15] [2.16]. The Doppler shift causes

the frequency of the returning echo to increase if the bat is closing in on the target or decrease if the target is moving away. This happens as the wave is compressed due to there being the same number of wavelengths in a shorter space, hence the distance between each wave decreases which increases frequency. Doppler compensation [2.17] is used by bats to alter the emission frequency so the returning echo has the same frequency normally implemented by the bat. For example if the target is moving away from the bat, the Doppler effect means the frequency of the returning echo is lower than that of the emitted one so the bat has to increase its emitted frequency which in turn increases the returning echo to the original CF frequency. This optimises the bats hearing ability as the acoustic fovea [2.18] and pinna shape are tuned to a predominant frequency [2.19] [2.20].

Insect wing beats are thought to be detected in one of two ways. Firstly the moving wing modulates the amplitude of the CF call [2.21] as the strength of reflection varies due to the wing angle changing relative to that of the incoming signal. The second is by Doppler shift in a similar manner to that of a moving target. A beating wing mimics a moving target which as discussed acts to modulate the amplitude of the signal which is detectable by the bat [2.6].

Figure 2.5. A selection of bat pinna from various species (adapted from Altringham [2 6])

2.1.4 *The reception of signals by echolocating bats*

Bats have relatively large pinna compared to their body size, often bigger than the head itself, some examples of this can be seen in the representative species in Figure 2.5. Important features of the pinna are the height and width of the aperture and the tragus

(labelled T on Figure 2.5) and antitragus (labelled A on Figure 2.5). The importance of the size of the aperture is explained by Guppy and Coles [2.22] where they show a strong correlation between wavelength of sound and aperture size between different species. Through evolution it could be expected the dimensions of the pinna would closely relate to the echolocation method implemented, either for the fundamental frequencies or filtered harmonics the bat may choose to process. Larger pinnae may be used for the listening to prey in the passive sense of target location or they could be used to receive lower frequency harmonics as these reflect differently off targets than high frequency ones. Obrist *et al.* [5.1] have performed a full study of pinna size and echolocation methods for several species of bats, from which their conclusions show how difficult it is to make many general observations due to the diversity in specific details of each echolocation system. Human made systems can use broadband transmit and receive systems to increase their versatility in most situations as a wider band will accommodate a greater variation in target shape and range. Filters at the receiver alter the frequency response enabling variable listening conditions, however these manipulations take time and energy to perform, reducing system efficiency. The inner ear of the bat uses passive filtering within the cochlea, whereby different areas are excited by different frequencies with these results relayed to the brain. This micro and neuro biology is very complex. An overview of some of the basic concepts and recent research is provided in [2.6]. Combining research into both neural processing and passive reception of the pinna may lead to an explanation in one field that has previously not been answered because each system was independently examined.

The tragus is the obvious flap of skin that sits on the outer edge towards the bottom of the pinna (labelled T on Figure 2.5). They are less conspicuous in humans but vary greatly in bats suggesting evolution has had a part in their development. Lawrence and Simmons [2.24] performed experiments with the tragus and found it affects the animal's ability to detect horizontal obstacles, thereby demonstrating that the tragus substantially affects vertical discrimination. An investigation using numerical modelling techniques has recently been carried on the role of the tragus by Muller [2.25]. He found it significantly varied the angle of the major sidelobe on the beam pattern of the pinna, as the

tragus was numerically manipulated in the finite element model.

Although not a direct feature of the pinna itself, pinna movement is also a very important for target localisation and navigation. Mogdans *et al.* [2.26] performed experiments to investigate its role in perceiving vertical and horizontal wire obstacles. They found restricting pinna movement in the Greater Horseshoe bat (*Rhinolophus ferrumequinum*) greatly affected the animal's ability to discriminate objects in the vertical plane. Although the two experiments ([2.24] and [2.26]) demonstrated the same outcome, they were for different bats with different echolocation mechanisms. The tragus causes spectral differences which allow FM bats to discriminate in the vertical plane whereas CF bats use pinna movement to vary the IID (interaural intensity difference) for the detection. IID quantifies the difference in sound intensity between two or more receiving devices; for bats these are their pinnae. The head related transfer function (HRTF) is also occasionally mentioned in bat literature. Although typically used for the auralisation in humans, it includes the effects of diffraction and reflection surrounding the head and pinna and can be used to extract more information of sound localisation than that of traditional IID and ITD which usually only detail azimuthal information. See [2.27] for further details.

2.2 Chiroptera inspired artificial echolocation systems

There have been several attempts to recreate or simulate the bat receiving system. An early attempt was by Barshan and Kuc [2.28] who employed a simple 2D system for detecting simple objects in an uncluttered environment. This system was then mounted on a mobile robot for use in detecting mobile moth-type targets [2.29]. They were able to detect target range and azimuth angle from traditional methods using the time taken for an echo to return to the transmitter/receiver. This system however does not utilise the directionality that comes with a pinna or other type of acoustic baffle which could improve efficiency and accuracy. Instead, a wideband system was used which has reduced spatial resolution due to a higher beam angle on the receiver. With increased

sensitivity over a narrower angle, actual target detection is more accurate. With greater directionality comes greater range as the same amount of "energy" is not spread over as great an area.

To achieve desired directionality patterns in synthetic systems such as submarines or ships, an array of transducers would normally be used. These such arrays can be *steered* and their directionality controlled by altering the phase and timings of the signal for each individual element. They do, however, suffer from ambiguity problems meaning it is often difficult to deduce from which of the two 180° hemispheres the sound originated from. A pinna or baffle would be an economical option and would not require any additional processing of the received signal. A limitation of this approach is the need to fix a mechanical object to the external body of the vessel, potentially leaving it liable to damage. One example of an acoustic baffle being implemented in a similar way are ear trumpets; used before the invention of the electronic hearing aid. Another famous use of the acoustic baffles, or more accurately, reflector are the "acoustic mirrors" built on the south and east coasts of the United Kingdom during World War 1 and 2 for listening to incoming aeroplanes. These were large concrete walls with a concave surface that reflected sound to a focal point where operators could listen for the planes. Sound mirrors provided a valuable early warning system detecting planes between about 8 and 15 miles from the coast. Unfortunately they became obsolete as planes became faster since they could be spotted in the air before they were heard. Artificial acoustic baffles are rarely seen elsewhere although the theory and implementation behind them is often used where noise is a problem such as on air intakes and outlets on mechanical machines.

In 1998 Peremens *et al.* [2.30] created a bat-inspired bionic sonarhead for 3D localisation of objects, known as a RoBat. They used the theory of interaural intensity differences (IID, also known as interaural amplitude difference, IAD) [2.31], to spatially resolve targets. The maximum interaural time difference (ITD) is approximately 50 μs for a bat head which according to Horiuchi and Hynna [2.32] is too small to be used by the bat. Peremens *et al.* [2.30] mimicked this calculation to facilitate their on-going

attempt to recreate the neural processing mechanism of the bat.

Similarly, in 2001 Müller [2.33] created a "biosonar-observer" in an attempt to view the world through the hearing of bats. The brief was to create a working model with as much realistic functionality as possible, such as moveable receivers. Among the limiting factor were the unsuitable, off-the-shelf components available. For instance the transducers were too narrowband, both for transmitting and receiving. Neither of these systems utilised pinnae although the intention was to try and use them on RoBat. Carmena *et al.* [2.34] investigated the shape of the biological pinna with intentions of replicating it in the bionic world. This work evolved that of Peremens *et al* [2.30] of the same institute who orientated three reflectors in such away to mimic the pinna of a bat.

2.2.1 *The European CIRCE project*

The most recent substantial attempt to recreate the echolocation system of a bat is by the CIRCE project [2.35]. CIRCE is a European project under the larger heading of "Information Society Technologies" (IST) where the project partners summarised their aims in the following statement;

> "The goal of the CIRCE project is to reproduce, at a functional level, the echolocation system of bats by constructing a bionic bat head that can then be used to systematically investigate how the world is not just perceived but actively explored by bats."

CIRCE partners are from all over Europe, each having their own technological expertise in areas such as signal processing, ultrasonic sensors and biosonar systems. This thesis has approached the problem of modelling the bat pinna using the TLM method, whereas the CIRCE project itself has implemented finite element analysis. In the following sections some commonly used finite modelling techniques will be reviewed and their relative merits discuss for the geometry under consideration.

2.3 Generic modelling methods in acoustics

There are many techniques capable of mathematically solving acoustical problems, including numerical and in special cases, analytical approaches. The numerical approaches are divided into more specific categories such as:

- Surface element methods like boundary element modelling (BEM)
- Volume element methods such as finite difference (FD) and finite element analysis (FEA)
- Ray based methods such as ray tracing using physical or geometric optics

2.3.1 Surface element methods

Surface element methods perform numerical calculations on elements lying only on the surface of the element and not on the space between them. Each surface is subdivided into elements, each having a size sufficiently small relative to the wavelength to ensure the surface fields are accurately represented. One significant advantage over other methods is that large areas of free space can be accommodated with very high efficiency, unlike in volume element methods where the space between objects also has to be meshed.

Boundary Element Method (BEM)

The boundary element method uses similar mathematics to that of the near to far field transformation which will be explained later. The pressure at a point is formulated using the Kirchhoff-Helmholtz integral which is then used to sum the contribution to that pressure from adjacent points (see Section 4.1). The application of integral equations to formulate boundary value problems was initiated in 1903 by Fredholm [2.36] who demonstrated solutions to these equations using a discretised procedure. The first realistic use of the method using digital computers was by Massonnet [2.37] in 1965 for

investigating elasticity problems. A thorough analysis of acoustical BEM can be found in [2.38] which gives a brief history and formulates routines for acoustical scattering of rigid bodies and acoustic analysis of ducts and mufflers.

2.3.2 Volume element methods

Volume element methods utilise a mathematical procedure for calculating approximate solutions to partial differential equations which predict the response of the system when subjected to a change in energy. Some of the most popular examples are briefly detailed in this section. TLM is a type of volume method as it approximates the system and solves it exactly, whereas the system in FEA and FDTD is described exactly by the equations which are then discretised, hence they are solved approximately. FEA solutions are most commonly found in the frequency domain whereas FDTD and TLM are formulated in time. One advantage of solving in the time domain is the ability to implement many different excitation techniques such as random noise or impulses. The solutions can then be used to examine transient phenomena or non-linear effects.

Finite Difference Time Domain (FDTD)

The space-time gridding which forms the basis of this method was first proposed by Yee [2.39] for isotropic, nondispersive media in 1966. This algorithm was later combined with an accurate absorbing boundary condition proposed by Mur [2.40] in 1981 to formulate a robust and computationally efficient method of studying the interaction of electromagnetic waves with arbitrary geometrical structures. The routine was converted for use in acoustics by Bottledooren [2.41] in 1994 for general use implementing nonuniform grids.

Finite Element Analysis (FEA)

FEA uses triangular meshing in 2D situations and tetrahedral geometry in 3D cases as opposed to quadrilateral meshing found in conventional FDTD and TLM. Thus, in

general FEA is more complicated and the formulation slightly more difficult due to the non-parallel or perpendicular nature of node locations. However, it has the advantage of adapting well to complex boundary shapes, and to spatially varying properties of the medium; permittivity (ε) and permeability (μ) in the electromagnetic case and compressibility (σ) and density (ρ) in acoustics. The key advantage of triangular or tetrahedral meshes is their superiority in mapping boundaries or material interfaces that are curved, where FDTD and TLM methods based on Cartesian coordinates are (in the normal case) forced to employ staircase approximations to such boundaries, specifically the curved ones (see Chapter 3.5) or those inclined at an angle to the mesh. The formulation of FEA was initially considered in the early 1900's but it was not until 1943 when Courant [2.42] proposed the full methodology. Young and Crocker [2.43] were among the first people to use FEA in the acoustic domain for analysing the performance of acoustic mufflers. With the invention of computers came practicality and the ability to solve the huge number of simultaneous equations needed to find solutions to problems using FEA. The software solver can be written manually or commercial packages such as NASTRAN, SYSNOISE or ANSYS can be used which have built in graphical routines to show results.

2.3.3 Ray based modelling

Ray tracing models acoustical energy emitted by a source that is considered to be composed of a large number of energy packages or pulses, concentrated along rays. The energy content of these pulses can be defined as a function of the direction in which each ray is emitted. Each time a ray hits one of the surrounding surfaces the energy content of the pulse decreases; the decrease depending on the reflection coefficient of that particular surface.

Figure 2.6 depicts the fundamental concept of ray tracing. S is the source with as many single transmission paths as the situation warrants and R is the receiver where sound pressure is to be measured. In the example there are barriers that would reflect the wave totally or partially and sections of the transmission medium defined by the shaded area

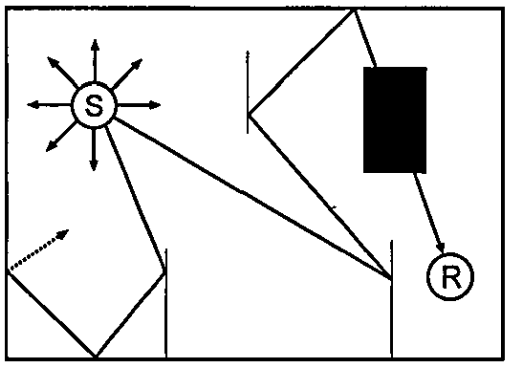

Figure 2.6: A simplified example of ray tracing

will affect the speed of propagation and hence the amount of reflection and refraction as described by Snell's Law when describing optical systems.

One of the most popular implementations of ray tracing has been in the acoustic design of rooms. One of the earliest practical implementations was by Krokstad *et al.* [2.44] with some of the most important work carried out by Schroeder [2.45] of whom the "Schroeder frequency" is named after. The "Schroeder frequency is the maximum frequency at which low order resonant modes an be expected; above this frequency the wavelength becomes short enough for resonance to become unpredictable. Another popular implementation is seen in large area underwater acoustics where low frequency sound travels great distances. In general, the wavelength of sound being considered should be substantially smaller than the baffles or reflectors interfering with the sound as diffraction is difficult to accommodate, however to some extent this can be dealt with. The limitations of memory were addressed by several people including Kulowski [2.46] back in 1985 where even small models took a substantial amount time to solve owing to the huge number of ray paths to be considered. Although the modern day PC allows for much more complex models, the ray tracing method has generally been superseded by volume element methods and general purpose commercial software, although it is still a valuable tool for long distance, far field models.

2.3.4 Why the TLM method?

Any of the aforementioned mathematical routines could have been considered for the project. TLM was chosen for many reasons which are summarised below;

- TLM is usually based in the time domain and is well-understood and to some extent, validated. This allows broadband excitation allowing a large number of frequencies to be captured (via FFT or similar) in a single simulation. Frequency domain analysis, effectively requires one complete simulation per frequency. For example, if time domain analysis can capture information about 10 frequencies in one simulation, frequency domain analysis would require 10 separate ones as it captures data for only one frequency at a time.
- Generally TLM performs simulations quicker than other volume element methods (though FDTD is similar).
- With CIRCE using FEA methods already, using an FDTD/TLM approach is an alternative method with which results could be compared.
- TLM has already been successfully implemented in underwater, biological acoustic systems as will be discussed, so there is a natural progression to airborne bio-acoustic systems.

2.4 An introduction into pinna performance parameters

When investigating the acoustical properties of bat pinnae, it is helpful to consider them in terms of the theory of antennas. Directionality index and beamwidth are two important parameters that describe the performance of pinna. Quantifying these properties between species is necessary when comparing different echolocation types and will give some understanding of the reception method. One resultant factor determined by the beamwidth of the pinna is how much detail a bat can detect, in other words reso-

lution. A high resolution (and small beam size) is helpful to the animal in accurately pinpointing a small object, however a lower resolution gives a wider "field of view".

2.5 Discussion

Echolocating bats display some of the most complex navigation systems in the natural world and are still the subject of active research. In this chapter a small number of selected publication on the functions of bats and on possible modelling techniques have been reviewed. This thesis takes the view that there is a substantial amount of signal processing needed to track prey flying at high speed with a completely random flight path. It seems reasonable to suggest that some of the processing is carried out passively in the bats ears to assist the brain in resolving targets.

There are several modelling techniques available to analyse this passive beamforming apparatus. TLM has a proven record with acoustics although use is limited compared with other methods such as FEA and FDTD so there is still scope for novel research. This thesis therefore aims to achieve a better understanding of the passive beamforming operation of bat pinnae and will implement the TLM technique as a means of achieving this.

References

[2.1] A. D. Grinnell and H. U. Schnitzler, "Directional sensitivity of echolocation in the Horseshoe bats, *Rhinolophus ferrumequinum*. ii. behavioral directionality of hearing," *Journal of Computational Physiology*, vol. 116, pp. 63–76, 1977.

[2.2] P. H. Jen and D. M. Chen, "Directionality of sound pressure transformation at the pinna of echolocating bats," *Hearing Research*, vol. 34, no. 2, pp. 101–117, 1988.

[2.3] J. L. Aroyan, *Three- Dimentional Numerical Simulation of Biosonar Signal Emission and Reception in the Common Dolphin.* PhD thesis, University of California at Santa Cruz, 1996.

[2.4] J. A. Flint, A. D. Goodson, G. Leonard, and S. C. Pomeroy, "Transmission line modelling of the Harbour Porpoise *(Phocoena Phocoena)* melon," *Journal of Acoustical Society of India*, vol. 30, no. 3-4, pp. 294–297, 2002.

[2.5] F. P. Mohres and E. Kulzer, "Uber die orientierung der flughund (chiroptera-pteropodidae)," *Z. Vgl. Physilogy*, vol. 38, pp. 1–29, 1956.

[2 6] J. D. Altringham, *Bats Biology and Behaviour.* Oxford University Press, 1996.

[2.7] M. J. Ryan, M. D. Tuttle, and R. M. R. Barclay, "Behavioural responses of the frog-eating bat, *Trachops cirrosus*, to sonic frequencies," *Journal of Computational Physiology A*, vol. 150, pp. 413–418, 1983.

[2.8] R. Coles, A. Guppy, M E. Anderson, and P. Schlegel, "Frequency sensitivity and directional hearing in the gleaning bat, *Plecotus auritus* (linnaeus 1758)," *Journal of Computational Physiology*, vol. 165, no. 2, pp. 269–280, 1989.

[2.9] P. D. Jepson, M. Arbelo, R. Deaville, I. A. P. Patterson, P. Castro, J. R. Baker, E. Degollada, H. M. Ross, P. Herráez, A. M. Pocknell, F. Rodríguez, F. E. Howie, A. Espinosa, R. J. Reid, J. R. Jaber, V. Martin, A. A. Cunningham,

and A. Fernández, "Gas-bubble lesions in stranded cetaceans," *Nature*, vol. 425, pp. 575–576, October 2003.

[2.10] D. R. Griffin, *Listening in the Dark.* Oxford University Press, 1958.

[2.11] K. S. Norris and G. W. Harvey, "Sound transmission in the Porpoise *(Phocoena Phocoena)* head," *Journal of the Acoustical Society of America*, vol. 56, pp. 659–664, August 1974.

[2.12] G. Jones and D. A. Waters, "Moth hearing in response to bat echolocation calls manipulated independently in time and frequency," *Proceedings of the Royal Society: Biological Sciences*, vol. 267, pp. 1627–1632, 2000.

[2.13] G. Neuweiler, W. Metzner, U. Heilmann, R. Rbsamen, M. Eckrich, and H. H. Costa, "Foraging behaviour and echolocation in the Rufous Horseshoe bat *(Rhinolophus rouxii)* of Sri Lanka," *Behavioural Ecology and Sociobiology*, vol. 20, pp. 53–67., 1987.

[2.14] J. A. Simmons, "The resolution of target range by echolocating bats'," *Journal of the Acoustical Society of America*, vol. 54, no. 1, pp. 157–173, 1973.

[2.15] H. U. Schnitzler, D. Menne, R. Kober, and K. Heblich, "The acoustical image of fluttering insects in echolocating bats," in *Neuroethology and Behavioral Physiology* (F. H. F and H. Markl, eds.), Springer Berlin Heidelberg New York, 1983.

[2.16] G. Neuweiler, V. Bruns, and G. Schuller, "Ears adapted for the detection of motion, or how echolocating bats have exploited the capacities of the mammalian auditory system," *Journal of the Acoustical Society of America*, vol. 68, pp. 741–753, September 1980.

[2.17] A. D. Grinnell, "Hearing in bats: An overview," in *Hearing by bats* (A. N. Popper and R. R. Fay, eds.), Springer-Verlag, 1995.

[2.18] G. S. G. Pollak, "Disproportionate frequency representation in the inferior colliculus of horsehoe bats: evidence for an acoustic fovea," *Journal of Computational Physiology*, vol. 132, pp. 47–54, 1979.

[2.19] G. Neuweiler, "Auditory adaptations for prey capture in echolocating bats," *Physiology Review*, vol. 70, pp. 615–641, 1970.

[2.20] J. A. Simmons, "Response of the Doppler echolocation system in the bat, *Rhinolophus ferrumequinum*," *Journal of the Acoustical Society of America*, vol. 56, pp. 672–682, August 1974.

[2.21] U. Firzlaff, *Processing of acoustic motion in the auditory cortex of the Rufous Horseshoe bat,* Rhinolophus rouxii. PhD thesis, an der Fakultat fur Biologie der Ludwig-Maximilians-Universität München, 2001.

[2.22] A. Guppy and R. B. Coles, "Acoustical aspects of hearing and echolocation in bats," in *Animal Sonar: Processes and Performance* (P. E Nachtigal and P. W. B. Moore, eds.), pp. 289–294, New York: Plenum Press, 1988.

[2.23] M. K. Obrist, M. B. Fenton, J. L. Eger, and P. A. Schlegel, "What ears do for bats: a comparative study of pinna sound pressure transformation in chiroptera," *Journal of Experimental Biology*, vol. 180, pp. 119–152, 1993.

[2.24] B. D. Lawrence and J. A. Simmons, "Echolocation in bats: The external ear and perception of the vertical positions of targets," *Science*, vol. 218, pp. 481–483, October 1982.

[2 25] R. Muller, "A numerical study of the role of the tragus in the big brown bat," *Journal of the Acoustical Society of America*, vol. 116, no. 6, pp. 3701–3712, 2004.

[2.26] J. Mogdans, J. Ostwald, and H. U. Schnitzler, "The role of pinna movement for the localization of vertical and horizontal wire obstacles in the Greater Horseshoe bat, *Rhinolophus ferrumequinum*," *Journal of the Acoustical Society of America*, vol. 84, pp. 1676–1679, November 1988.

[2.27] F. Filipanits Jr, "Design and implementation of an auralization system with a spectrum-based temporal processing optimization," Master's thesis, University of Miami, May 1994.

[2.28] B. Barshan and R. Kuc, "A bat-like sonar system for obstacle localization," *IEEE Transactions on Systems, Man and Cybernetics*, vol. 22, no. 4, pp. 636–646, 1992.

[2 29] B. Barshan and R. Kuc, "ROBAT: A sonar-based mobile robot for bat-like prey capture," *Proceedings of the 1992 IEEE International Conference on Robotics and Automation*, pp. 274–279, May 1992.

[2.30] H. Peremans, A. Walker, and J. C. T. Hallam, "3d object localisation with a binaural sonarhead, inspirations from biology," *Proceedings of the IEEE International Conferencen*, pp. 2795–2800, 1998.

[2.31] J. P. Oswald, A. Klug, and T. J. Park, "Interaural intensity difference processing in auditory midbrain neurons: Effects of a transient early inhibitory input," *The Journal of Neuroscience*, vol. 19, p. 11491163, February 1999.

[2.32] T. Horiuchi and K. Hynna, "Spike-based VLSI modeling of the ILD system in the echolocating bat," *Neural Networks*, vol. 14, pp. 755–762, 2001.

[2.33] R. Muller, "A synthetic biosonar-observer," in *4th Meeting of the German Neuroscience Society 2001*, vol. II of *28th Gottingen Neurobiology Conference*, (Stuttgart: Thieme), p. 1040, 2001.

[2.34] J. M. Carmena, N. Kämpchen, D. Kim, and J. C. Hallam, "Artificial ears for a biomimetic sonarhead: from multiple reflectors to surfaces," *Artificial Life*, vol. 7, no. 2, pp. 147–169, 2001.

[2.35] H. Peremans and R. Muller, "A comprehensive robotic model for neural and acoustic signal processing in bats," *Proceedings of The 1st International IEEE EMBS Neural Engineering Conference, 2003*, pp. 458–461, 2003.

[2.36] I. Fredholm, "Sur une classe d'equations fonctionelles," *Acta Mathematica*, vol. 27, pp. 365–390, 1903.

[2.37] C. Massonnet, "Solution générale du problème aux tensions de l'élasticité tridimensionelle," in *Proceedings of the 9th international congress in apoplied mechanics*, 1965.

[2.38] L. C. Wrobel, *The Boundary Element Method, Volume 1, Applications in Thermo-Fluids and Acoustics*. John Wiley and Sons, 2002.

[2.39] K. S. Yee, "Numerical solution of initial value boundary value problems involving Maxwell's equations in isotropic media," *IEEE Transactions on Antennas and Propagation*, vol. 14, no. 3, pp. 302–307, 1966.

[2.40] G. Mur, "Absorbing boundary conditions for finite-difference approximation of the time-domain electromagnetic-field equations," *IEEE Transactions on Electromagnetic Compatibility*, vol. 23, pp. 1073–1077, 1981.

[2.41] D. Botteldooren, "Acoustical finite-difference time-domain simulation in a quasi-cartesian grid," *Journal of the Acoustical Society of America*, vol. 95, pp. 2313–2319, May 1994.

[2.42] R. Courant, "Variational methods for the solution of equilibrium and vibration," *Bulletin of the American Mathematical Society*, vol. 49, pp. 1–23, 1943.

[2.43] C. Young and M. J. Crocker, "Prediction of transmission loss in mufflers by the finite element method," *Journal of the Acoustical Society of America*, vol. 57, pp. 144–148, January 1975.

[2.44] A. Krokstad, S. Strøm, and S. Sørsdal, "Calculating the acoustical room response by the use of a ray tracing technique," *Journal of Sound and Vibration*, vol. 8, pp. 118–125, 1968.

[2.45] M. R. Schroeder, "The "schroeder frequency" revisited," *The Journal of the Acoustical Society of America*, vol. 98, pp. 3240–3241, May 1995.

[2.46] A. Kulowski, "Algorithmic representation of the ray tracing technique," *Applied Acoustics*, vol. 18, no. 6, pp. 449–469, 1985.

CHAPTER 3:

THE TLM MODELLING METHOD FOR ACOUSTICS

TLM has evolved greatly since its original development by P. B. Johns and R. L. Beurle in the 1970s. Originally a tool to examine electromagnetic wave propagation, its uses have been greatly expanded due to its versatility and adaptability at the lowest level of implementation. Other uses of TLM include the modelling of microwave heat transfer [3.1], system vibration [3.2], hydraulic positioning in control systems [3.3] and diffusion modelling [3 4].

This chapter explains the method at a circuit theory level and provides some details of its implementation. Initially formulated in the electromagnetic domain it is also feasible to use analogies between the acoustical and electrical parameters in order to model acoustics. Finally there are examples given which demonstrate early applications in bioacoustics including an investigation into the Harbour Porpoise Melon.

3.1 The history of TLM

In 1970 Johns and Beurle [3.5] developed TLM in order to solve electromagnetic field problems such as Maxwell's equations. The idea arose from previous attempts by the likes of Kron [3.6] to solve field problems using electrical networks. The use of TLM for these problems was made possible by the development of digital computers as the number of numerical calculations needed were very large and too time consuming to be performed manually. The first 2D node used to simulate wave propagation was introduced by Akhtarzad and Johns in 1975 [3.7] and was an expanded node as the field components had spatial separation. The first symmetrical condensed node (SCN) was

formed by Johns [3.8] in 1987 which made all field components available at a single point which allowed for synchronised node voltage calculations. The first theoretical idea for constructing a 3D node was again by Akhtarzad and Johns [3 9] and arranged three series and three shunt connected nodes together to consider Maxwell equations in 3 dimensions. This topology again gave spatial separation between link-lines and was termed an expanded 3D node. 1984 saw the 3D node developed by Choi and Hoefer [3.10] which was symmetrical and condensed (an SCN), giving voltage synchronisation and good efficiency. This did not prove very useful as it also assumed either all the E-field or H-field had the same polarisation. This did not prove to be an issue in acoustic TLM as pressure is a scalar parameter. The first implementation of TLM in the acoustic domain was by Saleh and Blanchfield [3.11] in 1990 who created a appropriate 2D shunt node when they examined radiation patterns of arrays of acoustic transducers. This thesis considers the 3D acoustic nodes as developed by El-Masri *et al.* [5.5] and Portí and Morente [3.12], however the ability to model inhomogeneous materials using the Portí and Morente node is not required for the forthcoming models. The transition between electromagnetic and acoustical wave propagation is fundamental to understanding the TLM method and it is this that shall be addressed next.

3.2 Transmission lines

A transmission line is a guided path between two points where energy can pass. A simple example of this is a coaxial cable acting as a path for an electrical signal to propagate. There are fundamental theories that describe the energy flow passing from a transmission line of one impedance to a transmission line with a different impedance which becomes very important when implementing boundaries in a TLM mesh. If the impedance is different, part of, or the whole signal will reflect, if it is identical, i.e. a matched impedance, then it will pass with no reflections

Transmission lines are a distributed system and can be modelled using electrical circuit analogies. This entails lumping together inductors, capacitors and resistors to represent

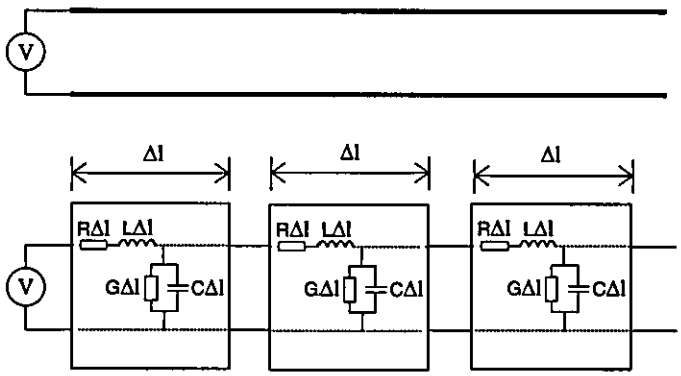

Figure 3 1: A transmission line and its lumped equivalent

a length of transmission line $\Delta\ell$. Lumped systems do not have a physical size so it does not take any time for the electrical signal to pass through them. In the real world it takes a finite amount of time for energy to flow through an electrical system, it is much simpler if lumped systems are used and time delays are ignored, although TLM has the ability to consider them. Figure 3.1 shows how a transmission line can be split into lumped sections of length Δl which is identical to $\Delta\ell$ in this case. For a TLM mesh where transmission lines intersect, the lumped electrical circuits are coupled together and a node is created.

3.3 2D nodes

Visualising waves propagating in a TLM mesh gives an impression of how the TLM routine works and how it is formulated. From Figure 3 2 it can be seen how an impulse of unity value added to one link-line propagates through the mesh. The mesh is a grid of transmission lines that are connected where they cross one another, this point is termed a node. For a 2D mesh there are four "link-lines" that all meet at a node. The impulse

arrives at a node and encounters an impedance mismatch as there are three more link-lines in parallel along its path. The signal is then split into four separate pulses, three of which propagate in a forward direction and one reflects back towards the origin of the original pulse.

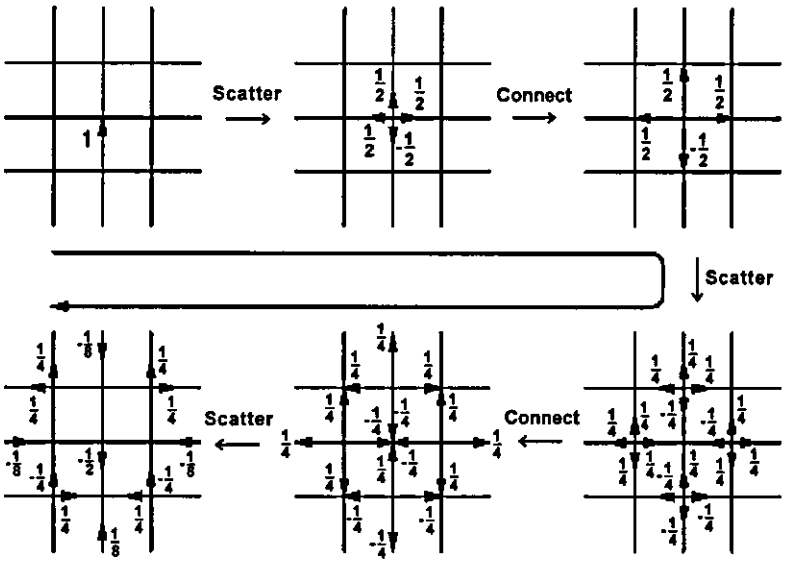

Figure 3.2. The TLM routine

Nodes can be internally connected in series or parallel. This is important in electromagnetic situations as there are two components on the propagating wave; magnetic (H-fields) and electric (E-fields) fields. Series nodes allow the modelling of TE (transverse electric) modes, i.e. with H_z, E_x and E_y where shunt (or parallel-connected) nodes model TM (transverse magnetic) situations with variation in E_z, H_X and H_Y. This thesis deals with 2D and 3D nodes connected in shunt configuration as shown in Figure 3.3. For a full derivation of series connected nodes for homogeneous and inhomogeneous materials refer to de Cogan [3.13] and Christopoulos [3.14].

3.3.1 Description of the 2D shunt node for acoustics

TLM was originally developed for use in the electromagnetic domain where parameters of transmission line signals such as voltage and current are proportional to the

field properties the mesh represents. When transforming to the acoustical domain it is important to show how the electrical parameters are equivalent to the acoustic ones.

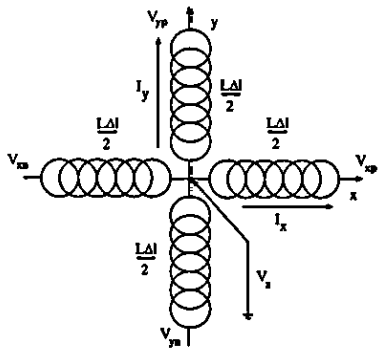

Figure 3.3: A lossless 2D shunt node at component level

From the shunt node in Figure 3.3 it can be shown how the total voltage on the node (V_z) varies in the x-axis (see Equation 3.1).

$$\Delta V_z = \Delta\ell \frac{\partial V_z}{\partial x} \tag{3.1}$$

Equation 3.2 shows the relationship between V_z and I_x.

$$\Delta V_z = -L\Delta\ell \frac{\partial I_x}{\partial t} \tag{3.2}$$

By combining Equations 3.1 and 3.2, Equation 3.3 is obtained that describes the change in voltage over a distance in terms of a change in current over time and the inductance as the constant of proportionality.

$$\frac{\partial V_z}{\partial x} = -L\frac{\partial I_x}{\partial t} \tag{3.3}$$

Note this is easily interchangeable for the y axis.

Current conservation in the circuit can be shown by Equation 3.4.

$$\frac{\partial I_x}{\partial x} + \frac{\partial I_y}{\partial y} = -2C\frac{\partial V_z}{\partial t} \tag{3.4}$$

Finally, combining Equations 3.4 and 3.3 gives the wave equation on the transmission line (Equation 3.5).

$$\Delta V_z = 2LC\frac{\partial^2 V_z}{\partial t^2} \tag{3.5}$$

From acoustical theory for a linear material with equilibrium density ρ, a coefficient of compressibility σ, and particle velocity u, the energy stored due to compression and volume change is shown in Equation 3.6 [3.15].

$$\frac{\partial u_x}{\partial x} + \frac{\partial u_y}{\partial y} = -\sigma\frac{\partial P}{\partial t} \tag{3.6}$$

Again this acoustic equation is a combined function that takes account of all cartesian directions. Equation 3.7 only represents the x direction and shows Newton's Law of the conservation of momentum of a fluid particle.

$$\frac{\partial P}{\partial x} = -\rho\frac{\partial u_x}{\partial t} \tag{3.7}$$

Combining Equation 3.6 and 3.7 gives Equation 3.8, the acoustic wave equation.

$$\Delta P = \frac{1}{c^2}\frac{\partial^2 P}{\partial t^2} \tag{3.8}$$

By examining the electrical Equations 3 4 and 3.3 and comparing them with the fundamental acoustic ones 3.6 and 3.8 the following analogies are easily seen (see Table 3.1).

3.3.2 2D lossless nodes for homogenous media

Lossless nodes (see Figure 3.3) are used to represent sound transmission in an homogenous medium. A medium is considered homogenous if the speed of wave propagation

Acoustic Theory	TLM Equivalent
P	V
u_x	$I_x \Delta \ell_x$
u_y	$I_y \Delta \ell_y$
σ	C
ρ	L

Table 3.1: Acoustic and electrical parameter equivalences

does not vary throughout the material, for instance sound travelling through air with constant temperature. The homogenous nature indicates the material properties remain constant throughout the complete path of transmission.

As a sound source excites a point in modelled space, a mathematical algorithm describes the nature of pressure dispersion and spreading as would happen in the real world. This equates to the introduction of a voltage on a node via a link-line and *scattering* due to the mismatch in impedance it meets. A scatter method is formulated to distribute the impulse voltage between the other link-lines.

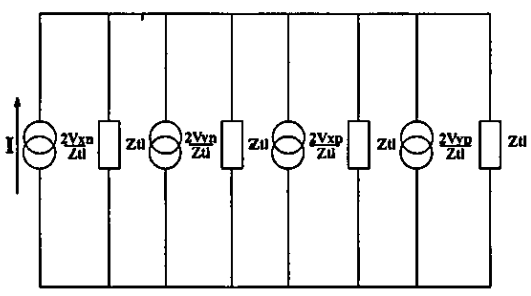

Figure 3.4: Equivalent circuit for a lossless 2D shunt node

To formulate the scatter method an equivalent circuit (see Figure 3.4) for the 2D shunt node (see Figure 3.3) is used to develop a scatter matrix. It is the scatter matrix which splits the impulse voltage (^{i}V) and generates reflected voltages (^{r}V) for impulse on to

an adjacent node on the next time step.

From the circuit (Figure 3.4) the current (I) can be seen in Equation 3.9.

$$I = \left[\frac{2V_{xn} + 2V_{xp} + 2V_{yn} + 2V_{yp}}{Z_{tl}}\right] \tag{3.9}$$

Similarly the total impedance is seen in Figure 3.10.

$$Z = \left[\frac{1}{Z_{tl}} + \frac{1}{Z_{tl}} + \frac{1}{Z_{tl}} + \frac{1}{Z_{tl}}\right]^{-1} = \left[\frac{4}{Z_{tl}}\right] = \frac{Z_{tl}}{4} \tag{3.10}$$

Finally the voltage on the node (termed "node voltage") is given in Equation 3.11.

$$V_z = I \times Z = \frac{Z_{tl}}{4}\left[\frac{2V_{xn} + 2V_{xp} + 2V_{yn} + 2V_{yp}}{Z_{tl}}\right] = 0\ 5[V_{xn} + V_{xp} + V_{yn} + V_{yp}] \tag{3.11}$$

From the node voltage (V_z) and the incident voltages that reach the node centre at a particular time step (k), the reflected voltages can be determined from the following equation (Equation 3.12).

$${}^{r}_{k}V =_{k} V_z -^{i}_{k} V \tag{3.12}$$

Reflected voltages are referred to using ${}^{r}V$ notation with incident voltages similarly labelled using ${}^{i}V$. For each link-line voltage the complete scatter process may be expressed algebraically by a scattering matrix, S, i.e.:

$${}^{r}\mathbf{V} = \mathbf{S}\,{}^{i}\mathbf{V} \tag{3.13}$$

where:

$${}^{r}\mathbf{V} = \begin{bmatrix} {}^{r}V_{xn} \\ {}^{r}V_{xp} \\ {}^{r}V_{yn} \\ {}^{r}V_{yp} \end{bmatrix}$$

$$\mathbf{S} = \frac{1}{2}\begin{bmatrix} -1 & 1 & 1 & 1 \\ 1 & -1 & 1 & 1 \\ 1 & 1 & -1 & 1 \\ 1 & 1 & 1 & -1 \end{bmatrix}$$

$$^{i}\mathbf{V} = \begin{bmatrix} ^{i}V_{xn} \\ ^{i}V_{xp} \\ ^{i}V_{yn} \\ ^{i}V_{yp} \end{bmatrix}$$

3.3.3 2D lossy nodes for inhomogeneous media

This section develops a node that allows inhomogeneous transmission mediums to be modelled. This means the node will effect the speed of wave propagation in the situation being modelled but not effect the speed of wave as it travels in the TLM mesh. Varying L and C in the circuit will have the desired effect for the modelled situation but synchronicity will be lost in the TLM network. For the TLM algorithm to behave correctly the voltages on the transmission lines must arrive at the node simultaneously. To overcome these differences in propagation arrival times a capacitive "stub" is added to the node, a concept devised by Johns in 1974 [3.16]. Stubs are widely used in microwave engineering to match antennas to specific frequencies and within microwave circuits generally. Another way to model inhomogeneous media is to implement specific boundary conditions at points where the different materials meet. This can be efficient when modelling space where material properties do not change rapidly but less so if connecting nodes represent many different parameters.

Figure 3.5 shows the 2D lossless node with capacitive stub. A capacitive stub represents an open circuit. This gives an increase in capacitance on the node and by analogy a rise in σ (compressibility) which effects wave propagation.

Figure 3.6 shows the Norton equivalent circuit of the lossy node. The stub is represented by a current source (V_s/Z_{tl}), normalised characteristic admittance ($\hat{Y}_s$) with respect to

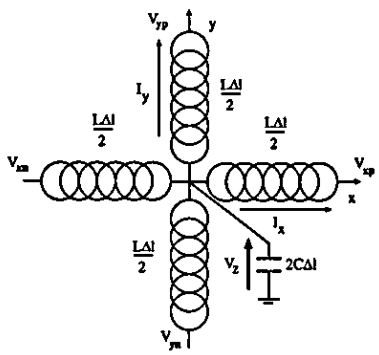

Figure 3.5: A lossy 2D shunt node at component level

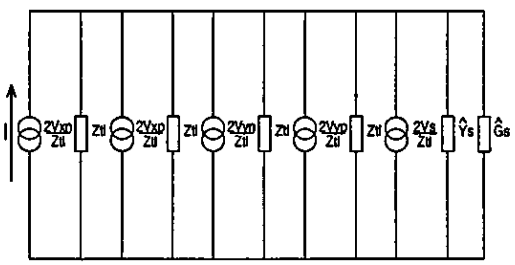

Figure 3 6: Equivalent circuit for a lossy 2D shunt node

the characteristic impedance (Z_{tl}) and normalised characteristic conductance ($\hat{G}_s$) with respect to the characteristic impedance (Z_{tl}) Although not shown in Figure 3.5, the conductance acts as an infinitely long transmission line to represent the loss of energy in the system. The amount of energy loss depends on the media being represented. The admittance and current source represent an energy store that delays wave propagation which is then reintroduced on to a node similar to the other link lines. The circuit theory is very similar to that of the lossless node which gives a node voltage (V_z) of:

$$V_z = \frac{2[V_{xn} + V_{xp} + V_{yn} + V_{yp}] + 2V_s\hat{Y}_s}{4 + \hat{Y}_s + \hat{G}_s} \tag{3.14}$$

The scattering matrix is formulated in the same way as the lossless node which gives

the following information:

$$^{r}\mathbf{V} = \mathbf{S}\,^{i}\mathbf{V} \tag{3.15}$$

where:

$$^{r}\mathbf{V} = \begin{bmatrix} ^{r}V_{xn} \\ ^{r}V_{xp} \\ ^{r}V_{yn} \\ ^{r}V_{yp} \\ ^{r}V_{s} \end{bmatrix}$$

$$\mathbf{S} = \frac{1}{\hat{Y}} \begin{bmatrix} 2-\hat{Y} & 2 & 2 & 2 & 2\hat{Y}_s \\ 2 & 2-\hat{Y} & 2 & 2 & 2\hat{Y}_s \\ 2 & 2 & 2-\hat{Y} & 2 & 2\hat{Y}_s \\ 2 & 2 & 2 & 2-\hat{Y} & 2\hat{Y}_s \\ 2 & 2 & 2 & 2 & 2\hat{Y}_s-\hat{Y} \end{bmatrix}$$

$$^{i}\mathbf{V} = \begin{bmatrix} ^{i}V_{xn} \\ ^{i}V_{xp} \\ ^{i}V_{yn} \\ ^{i}V_{yp} \\ ^{i}V_{s} \end{bmatrix}$$

Where $\hat{Y} = 4 + \hat{Y}_s + \hat{G}_s$.

3.3.4 The connect stage

The connect routine is used to shift link-line voltages from one node to another for use during the next time step. This propagates the voltages in the mesh.

In this case, voltages propagate from left to right and down to up. Using Figure 3.7 to explain the method, the reflected voltage ${}^{r}_{k}V_{xp}(x,y)$ of time step k, becomes the impulse voltage ${}^{i}_{k+1}V_{xn}(x+1,y)$ on the next node $(x+1,y)$ for the next time step $(k+1)$.

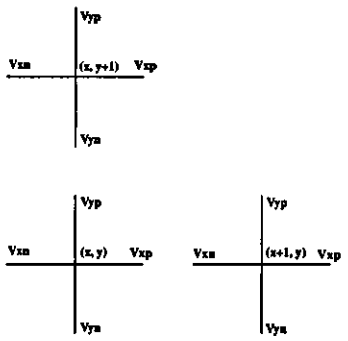

Figure 3.7: The connect routine

The same is true in the y direction. ${}^{r}_{k}V_{yp}(x, y)$ becomes the incident voltage ${}^{i}_{k+1}V_{yn}(x+1, y)$ for the node $(x, y+1)$ on the next time step $(k+1)$.

It is within the connect routine that boundaries conditions are usually implemented. This is to maintain synchronisation between propagating voltages which will be explained in a later section.

3.3.5 2D time step

The time step (Δt) of a TLM mesh describes the time taken for a pulse to travel between two nodes. This is not quite as simple as the distance over wave speed as the wave travels slower in a TLM mesh by a factor of $\sqrt{2}$ than in the real world as it takes longer for waves to reach adjacent nodes on a 45° axis. The revised time step can be seen in Equation 3.16.

$$\Delta t = \frac{\Delta \ell}{c\sqrt{2}} \tag{3.16}$$

Consequences of an incorrectly calculated time step include an under sampled sinusoidal input source which would show the effects of aliasing and give erroneous propagation

3.4 3D nodes

This section consider nodes that model space in three dimensions allowing realistic situations to be observed. 3D models allow for diffraction of sound between objects in any plane which is an important factor that adds realism. The node considered is the symmetrically condensed node (SCN) for acoustics both in homogeneous and inhomogeneous materials.

3.4.1 3D nodes for lossless, homogeneous media

El-Masri *et al.* [5.5] developed a method for modelling the human vocal tract, they formulated a simple scatter matrix that is similar to that of the 2D equivalent. The TLM mesh was constructed from equidistant nodes which meant the time step and wave propagation speed was constant in each cartesian direction as the node separation is equal (a cubic mesh). The node is lossless in performance and could only model materials with uniform compressibility and equilibrium density.

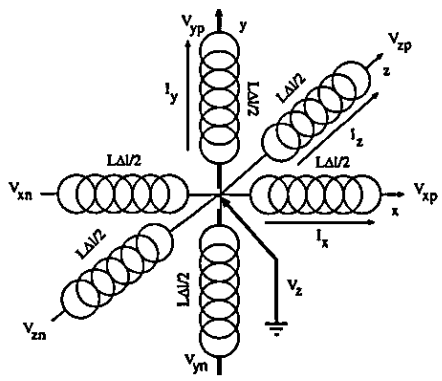

Figure 3.8: A lossless 3D scalar node at component level

Figure 3.8 shows the circuit diagram for a scalar node in a cubic mesh. The capacitance is lumped together and the inductance is constant, but for the case a parallelepipedic mesh the inductance and capacitance would be different in each cartesian direction.

The aforementioned scatter matrix is:

$$\mathbf{S} = \frac{1}{3}\begin{bmatrix} -2 & 1 & 1 & 1 & 1 & 1 \\ 1 & -2 & 1 & 1 & 1 & 1 \\ 1 & 1 & -2 & 1 & 1 & 1 \\ 1 & 1 & 1 & -2 & 1 & 1 \\ 1 & 1 & 1 & 1 & -2 & 1 \\ 1 & 1 & 1 & 1 & 1 & -2 \end{bmatrix}$$

3.4.2 3D nodes for lossy, inhomogeneous media

The node developed by Portì and Morente [3.12] can model sound in inhomogeneous materials. It can also model parallelepipedic meshes where node separation is different in each cartesian direction. The minor disadvantage over the previous method is that there are many different coefficients that need calculating before running the scatter routine. These coefficients relate to node separation and the dependent varying impedances of the transmission lines.

The scattering matrix for the lossy node is as follows:

$$\mathbf{S} = \begin{bmatrix} a_x & b_x & c & c & c & c & f & -h_x & & \\ b_x & a_x & c & c & c & c & f & h_x & & \\ c & c & a_y & b_y & c & c & f & & -h_x & \\ c & c & b_y & a_y & c & c & f & & h_x & \\ c & c & c & c & a_z & b_z & f & & & -h_z \\ c & c & c & c & a_z & b_z & f & & & h_z \\ d & d & d & d & d & d & g & & & \\ -e_x & e_x & & & & & & j_x & & \\ & & -e_y & e_y & & & & & j_y & \\ & & & & -e_z & e_z & & & & j_z \end{bmatrix}$$

A 3D representation using this node can be described by an electrical circuit constructed from one parallel and three series node, however they are only partially coupled [3.12].

The first six voltages that relate to the first six rows of the scatter matrix are the standard link-line voltages as previous(V_{xn}, V_{xp}, V_{yn}, V_{yp}, V_{zn}, V_{zp}). The next relates to the short-circuit stub (V_s) which models changes in the transmission medium. The final three voltages relate an extra short-circuited stub for each of the axial voltages, either V_x, V_y or V_z. These extra stubs again vary the density and compressibility factor in a particular cartesian direction. A description of the individual coefficients are in Appendix A with parameters for airborne ultrasonics..

The time step for the 3D node is given in Equation 3.17.

$$\Delta t = \frac{\Delta \ell}{\sqrt{3}c} \tag{3.17}$$

3.5 Dispersion

Transferring from real world models to meshed mathematical ones can lead to erroneous results due to discretisation. Physical data is continuous where the modelled world is discrete. Therefore it is important to use the correct level of digitisation when transforming between the two domains. The disadvantage to high definition digital models is that more computer memory is needed. Figure 3.9(A) shows a real world entity with an infinite number of points between the two end points. Figure 3.9, (B) and (C) are the digitised representations of this line where there is quantisation error due to the finite number of points. (B) is a better representation as it has more discrete data points to model the line than (C) but takes up more computer memory.

If the correct level of digitisation is not used, physical differences in the distances between the same points in the real and modelled world could be in the order of wavelengths of the sound source used to excite the model. This would have dramatic effects on the results as wavelength sized edges can dramatically effect propagation.

Dispersion takes place as a consequence of this discretisation process during modelling. The chief outcome of this is the limiting of the maximum frequency the mesh can handle. This in turn limits the amount of space a TLM mesh can model because as

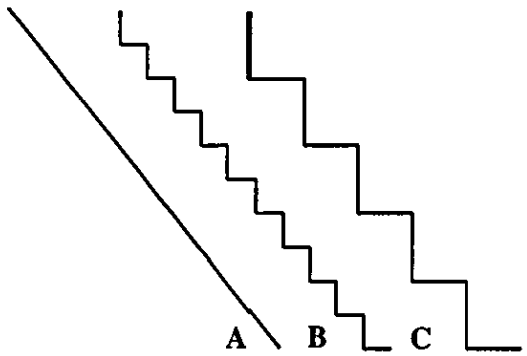

Figure 3.9: Simple discretisation

frequency goes up, the distance between nodes goes down so the same number of nodes will represent a shorter distance in space. The effects of dispersion are minimised at low frequencies where the node separation $\Delta\ell$, is much smaller than the wavelength, λ of the excitation source.

Dispersive wave propagation can be easily observed because the wave speed differs at different propagation angles. Figure 3.10 (from Equation 3.18) shows that for a 45° angle, wave propagation speed is constant in both the real and modelled world. However at 0° there is a variation in propagation speed between real and the modelled world. These variations happen because wave propagation speed is frequency dependent in an axial direction and frequency independent at 45°. A thorough analysis of the phenomena was performed by Neilson and Hoefer [3.17].

$$\frac{u_{TLM}}{u_{TL}} = \frac{\pi\left(\frac{\Delta\ell}{\lambda_0}\right)}{\sin^{-1}\left[\sqrt{2}\sin\left(\pi\frac{\Delta\ell}{\lambda_0}\right)\right]} \tag{3.18}$$

To minimise dispersion a maximum frequency is specified that the mesh can accurately model, this is the limit where the effects of dispersion can be tolerated. General consensus says at least ten nodes should represent one wavelength in the mesh [3.18]. Hence for a node separation of length $\Delta\ell$, the following identity must be true; $\Delta\ell < \frac{\lambda}{10}$. This then sets the *cutoff* frequency (f_{max}) for a mesh; $f_{max} = \frac{c}{10\Delta\ell}$ where c is the speed

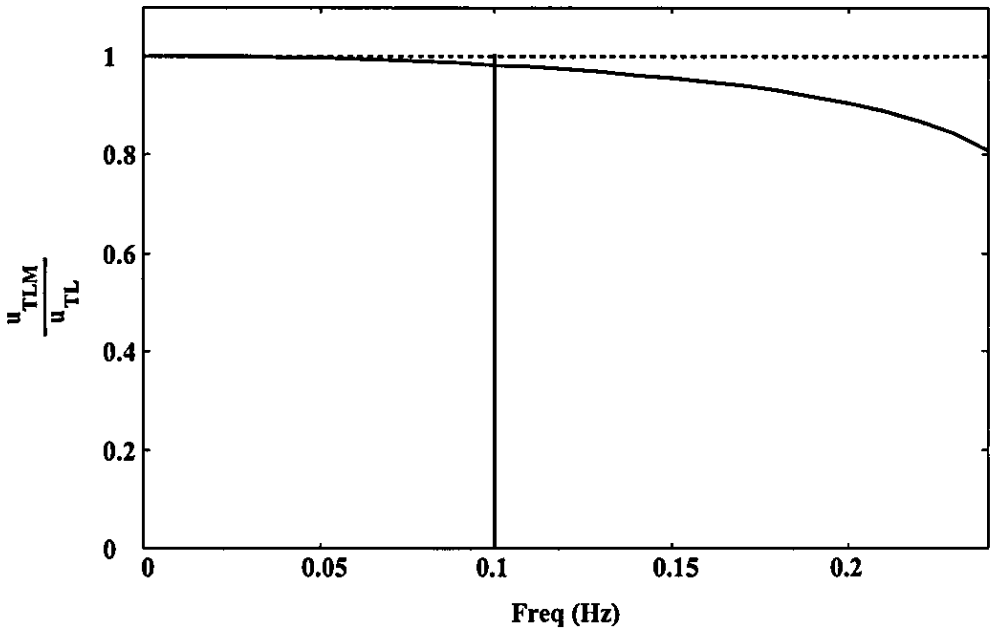

Figure 3.10: Graph showing the ratio of model to real-world wave velocity against source frequency in 2 dimensions

of sound in air. For example a 115 kHz signal has a wavelength of 0.00288 m so the maximum node separation must be 0.000288 m.

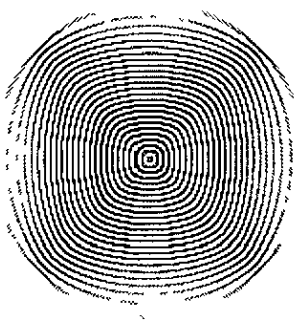

Figure 3.11: An example of dispersion causing waves to propagate fastest on the 45° axis

Figure 3.11 shows how dispersion affects propagation in a working TLM mesh. For the

mesh shown, the frequency of excitation is twice that of the mesh cutoff frequency and it can be seen that the source does not propagate spherically.

3.6 Boundaries

A TLM mesh cannot model an infinite amount of space due to computer memory limitations and realistic processing times. Hence the edge of this working space needs to be defined and wave propagation on this edge needs to be conditioned to react to give desired results. This outer surface can either absorb propagating wavefronts or reflect them, partially or totally depending on the situation being modelled.

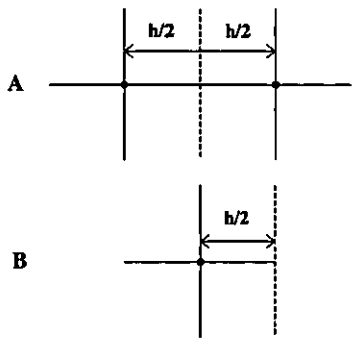

Figure 3.12. Boundary location

Boundaries are defined at the end of the link-line protruding into space on the outer most node on each face of the TLM mesh (see Figure 3.12(B), dashed line). This is an actual length of $\frac{\Delta\ell}{2}$ where $\Delta\ell$ is the node separation. To maintain synchronisation, boundary conditions are applied to the link-line at the same time as connection. This means the total distance travelled by the voltage on the edge of the mesh on that time step is $\Delta\ell$ which is the same distance between two node centers (see Figure 3.12(A)). This ensures all wavefronts on the mesh have travelled the same distance in one time step.

3 6.1 Absorbing Boundary Conditions

Absorbing boundary conditions (ABC's) aim to prevent outgoing waves reflecting back into the TLM mesh from the edge of the space being modelled. Two possible ways of achieving this are by using matched termination and perfectly matched layer (PML) type boundaries. There are several other ways of producing ABC's. These include space-time extrapolation methods that use one-way equations which were first introduced my Mur in 1981 [3.19] for use with FDTD methods, the method was developed for TLM by Morente *et al.* [3 20] in 1992. A further, yet unpopular method which allows waves to propagation in only one direction using a discrete Green's function to define an absorbing walls was devised by Hoefer [3.21] and termed the Johns Matrix. An investigation of the instabilities of these techniques and many more was performed by Banai *et al.* [3.22] which concluded they were computationally expensive and unstable compared to matched termination when an incorrect number of time steps were used.

One advantage of high performance numerical absorbing boundaries is that they can be placed much closer to the actual area of interest meaning less free space has to be modelled as in other methods, hence there are huge savings in memory to be gained.

Figure 3.13 shows absorbing boundaries in a mesh excited with a central point source. Propagation can be seen up until the boundary where it is apparent, no or very little of the wave is reflected back into the mesh. Numerical methods can be used to show these small reflections such as those demonstrated by Banai *et al.* [3.22].

Matched Termination

Matched termination boundaries function by matching the transmission line impedance with the termination impedance, theoretically allowing the voltage to propagate out of the mesh on an infinitely long transmission line. An idealised ABC would absorb all waves irrespective of frequency or incident angle. If the impedance of the termina-

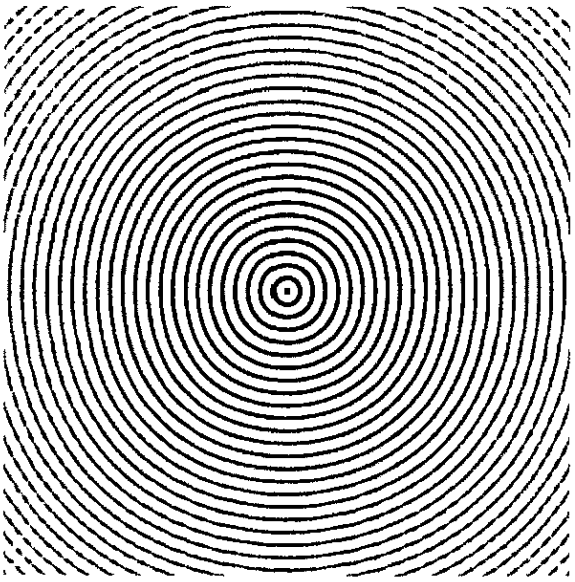

Figure 3.13: A 200 node square mesh excited with a 115 kHz sinusoid showing spherical propagation using absorbing boundary conditions

tion is not equal to that of the transmission line, the signals will reflect as in standard transmission line theory.

$$\rho = \frac{Z_A \Delta\ell_x - Z_o}{Z_A \Delta\ell_x + Z_o} \tag{3 19}$$

Portí and Morente [3.12] apply Equation 3.19 to match the impedance of a 3D transmission line with characteristic impedance (Z_o), acoustic impedance (Z_A) and variable node separation (Δl_x, Δl_y, or Δl_z) for absorbing boundaries. In the case of this thesis Z_A was constant due to the transmission medium being air as were l_x, l_y and l_z. Equation 3.20 can then be substituted into Equation 3.19 to obtain a simplified reflection coefficient (ρ, Equation 3.21).

$$Z_o = Z_A \sqrt{3} \Delta\ell \tag{3.20}$$

$$\rho = \frac{1 - \sqrt{3}}{1 + \sqrt{3}} \tag{3.21}$$

This is similar to the 2D matching condition (Equation 3.22). In fact the matched termination does give reflections since the assumption made for the transmission line is only valid for waves propagating parallel to the boundary. Hence a spherical wavefront striking a boundary will only be perfectly absorbed where the propagation is normal to the boundary.

$$ {}^{i}_{k+1}V\rho = {}^{r}_{k}V\frac{1-\sqrt{2}}{1+\sqrt{2}} \tag{3.22} $$

Perfectly Matched Layers

Perfectly matched layers were first described by Bérenger [3.23] for use with electromagnetic waves. Their first implementation was within the FDTD method [3.24] but there have been many specific TLM implementations including Peña and Ney [3 25]. The PML was adapted for acoustics by several people including Liu and Tao [3.26] and implemented in FDTD by Zhao and Cangellaris [3.27] and TLM by de Cogan *et al.* [3.28]. The technique involve adding extra nodes to the outer edge of the mesh which wavefronts penetrate, however they are not considered when obtaining results from the situation being modelled. These nodes acts as a perfectly lossy layer which absorb the propagating waves no matter the angle they strike the boundary. Despite the addition of nodes to the working space, overall they are more efficient as they can be placed much closer to the area of interest than other methods.

The implementation of PMLs would have been an acceptable method of obtaining absorbing boundary conditions, however the insensitive nature of directionality patterns meant the matched termination method was suitable. Other reasons for not using PMLs include the abundance of computer memory for this particular model so there was not too much emphasis on saving it and commercial software such as Microstripes uses matched termination as their default settings.

3.6.2 Reflecting Boundaries

Total reflection occurs in either open-circuit (capacitive) or short-circuited (inductive) boundaries. Open circuits have a reflection coefficient, ρ =+1 where boundaries are taken to have infinite acoustic impedance. As the boundary does not flex with the pressure of the travelling wave, the reflection is in the same phase as that which hits it. Short circuits have a reflection coefficient; ρ =-1 and is termed a pressure-release boundary. An example of this is an air-water boundary where the sound pressure will flex the water face which inverts the phase giving total reflection in anti-phase.

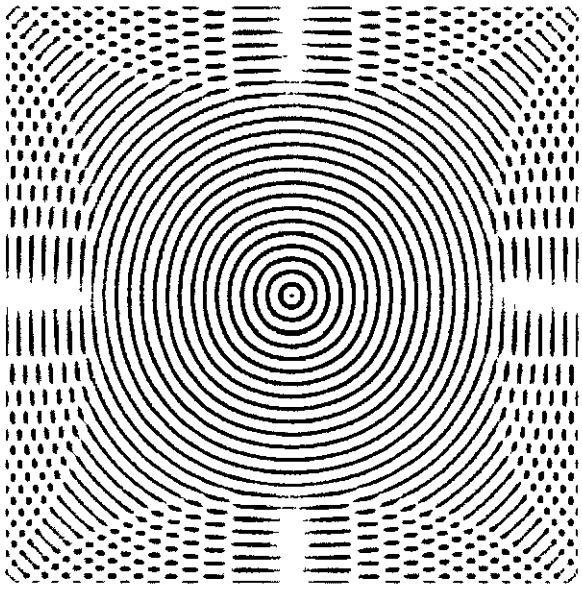

Figure 3.14: A 200 node square mesh excited with a 115 kHz sinusoid showing spherical propagation where boundaries perfectly reflect, i e. ρ=+1

Figure 3.14 shows boundary conditions where ρ=+1 meaning waves propagating on to the boundary will be perfectly reflected.

3.7 Excitation, measurements and the TLM routine

In order to inject wave energy into the TLM mesh, it is necessary to select a suitable method and excitation waveforms. In this section some issues relating to excitation

along with the techniques for measuring pressure from the mesh.

3.7.1 Excitation waveforms

The simplest technique involves exciting the node simply by equally adding voltages to each link-line. An important issue to consider in the excitation waveform is dispersion. Whilst dispersive propagation is associated with high frequencies and can be filtered out, it should remembered that the mesh data is represented inside a computer as floating point numbers. If high frequency, dispersive waves dominate the response, the useful signals maybe lost in the noise floor. There are consequently benefits in band limiting the signal fed to the mesh so as to avoid exciting high frequencies beyond the cutoff of the mesh.

Broadband Excitation

This is achieved by introducing an impulse on to a node for a single time step, a Delta pulse. It is broadband due to the wide frequency range that this pulse will excite. A theoretical Fourier Transform of the signal shows an infinite number of excited frequencies. To add a 1-volt pulse on to a 2D node each of the four link-lines should be excited simultaneously with a 0.5-volt positive signal. From the equation for node voltage (3.11) the 1-volt excitation can be seen as: $0.5 \times (0.5 + 0.5 + 0\ 5 + 0.5)$. One possible use for this signal is when looking for resonant frequencies in cavities as an infinite number frequencies are introduced.

Narrowband Excitation

This is simply achieved by introducing a sinusoidal wave on to a given node.

$$f(t) = \sin(2\pi f t) \tag{3.23}$$

f is the frequency and t is the time (iteration number multiplied by the time step, implementing negative iterations in this case). This only excites one frequency which gives control over frequencies around the mesh cutoff. It is useful for testing whether a mesh is constructed properly and gives an easily visible signal when observing the propagation over a period of time. Any obvious discrepancies will clearly be seen such as unwanted voltage sources from calculation errors or inaccurate absorbing boundary conditions for instance.

Gaussian Signal

This is a narrowband excitation which gives a short impulse time like that of a Delta spike but has control over the cutoff frequency reducing dispersion.

$$f(t) = Ae^{-\frac{t}{\sigma}^2} \tag{3.24}$$

Equation 3.24 shows a mathematical description of the signal where A is the amplitude of the signal, t is time (iteration number multiplied by the time step) and σ is the standard deviation which determines the width of the signal.

Filtered Excitation

A low-pass filtered source is suitable for band-limiting excitation of the mesh. The situation modelled can be examined over a wide frequency range with the simulation only being run once. A suitable filter response can be obtained by convolving a (wide) low-pass rectangular Sinc function (Equation 3.25) with a (narrow) Gaussian filter (Equation 3 26) to improve roll off. A solitary low-pass rectangular function is much less effective as this time-domain roll rate off is too low.

$$H(t_{SINC}) = 2f_c\frac{\sin(2\pi f_c t)}{2\pi f_c t} \tag{3.25}$$

$$H(t_{GAUSS}) = e^{-(\pi f_g t)^2} \tag{3.26}$$

f_{op} is the desired output frequency to be used in the mesh, f_c is the cutoff frequency of the filter ($= 1\ 3 \times f_{op}$), f_g is the Gaussian frequency ($= 0.2 \times f_{op}$) and t is time (iteration $\times$ time step).

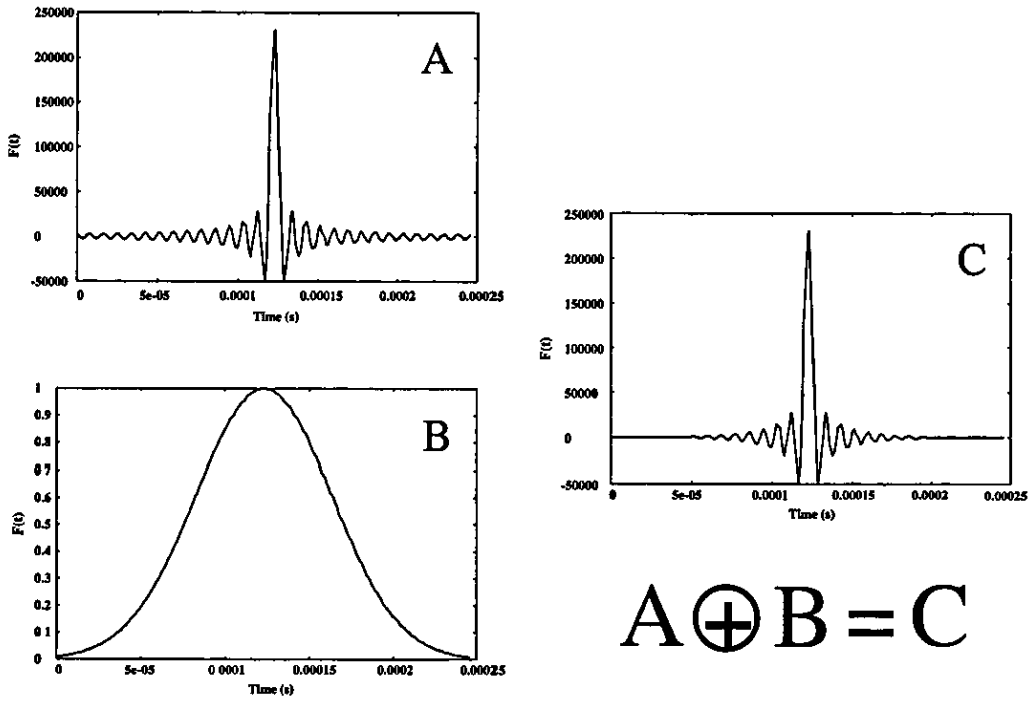

Figure 3.15: Time domain response of the individual low pass filter components

Figure 3.15(A) shows the time domain response of a Sinc function with a filter cutoff frequency of 115 kHz and time step of 1.23×10^{-6} s. Figure 3.15(B) is a Gauss pulse with the same parameters and Figure 3.15(C) is calculated by convolving the Sinc and Gauss functions

Figure 3.16(A) shows the frequency domain equivalent of the Sinc function where as (B) shows the frequency domain response for the complete convolved signal. It can be seen how the ripple and roll off is improved due to the Gauss pulse by comparing

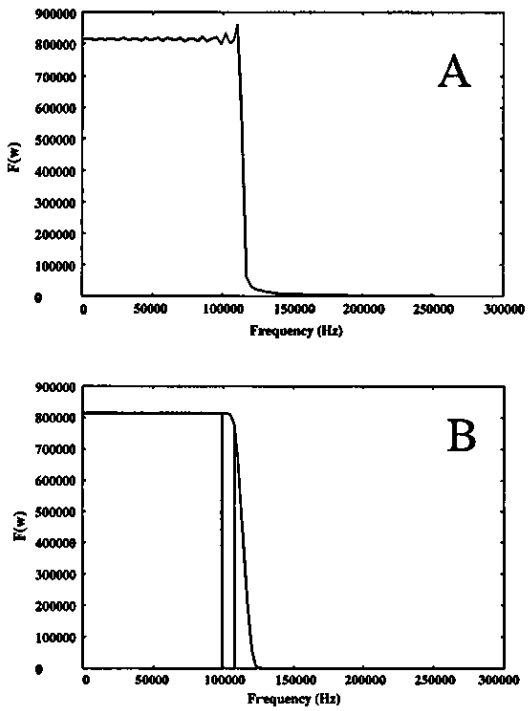

Figure 3.16: Frequency domain response of the individual low pass filter components

Figure 3.16(A) and (B). Since a Gaussian is never zero, there is no cut-off frequency. The Fourier transform of one Gauss with $\sigma = x$, is another Gaussian pulse with $\sigma = 1/x$ hence the frequency domain equivalent is missing from the relevant figure.

Plane wave excitation

A plane wave is one in which the wavefront has no effective curvature. This means the wave is seen to be in the far field by an observer or scattering object. The specialised situation can be recreated in TLM (Flint [3.30]) by exciting a line in 2D or an area of points in 3D as shown in Figure 3.17. A full mathematical description of the acoustic plane wave can be seen in [3.29].

Figure 3.17(A) shows a sinusoidal acoustic plane wave propagating in air and Figure 3.17(B) shows a Gaussian plane wave propagating in the same mesh. Figure 3.17(C)

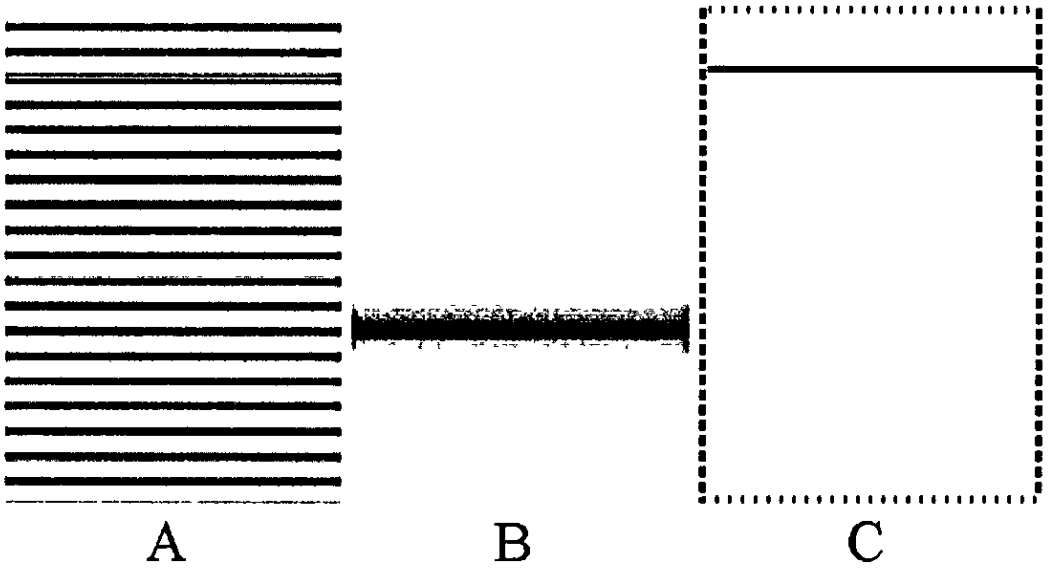

Figure 3.17: Plane wave propagation and details of mesh parameters

illustrates how the simple 2D mesh has been constructed. There are two different boundary conditions implemented, the first is absorbing represented by the lighter, horizontal, parallel and dashed lines. The second boundary implements a +1 reflection coefficient which is represented by the denser, vertically parallel and dashed lines. By definition, plane waves are infinitely large and have to be represented in a TLM mesh with those constraints, this is similar to that of a TLM mesh with absorbing boundaries which appears to be infinitely large themselves. Therefore, a plane wave has to be implemented across an entire axis of the model space meaning interaction with certain boundaries (vertical heavy dashed line in Figure 3.17(C)) need critical conditioning. If absorbing boundary conditions were implemented here, the edge of the wave would be effectively lost as it would propagate in to space. The use of a +1 reflection coefficient reintroduce any out going pressure back in to the mesh leading to a closed systems as the propagating waves are of equal pressure (represented by a consistent colour depth) in Figure 3.17(A). The solid line in Figure 3.17(C) is a row of excited nodes that stretches from one side of the mesh to the other, in this case a 55 kHz sinusoid was used in a mesh constructed for a maximum excitation frequency of 115 kHz.

3.7.2 Measurement and Results

Measuring the voltage on a node is equivalent to measuring the pressure at that point as discussed in the earlier analogy section. This thesis has used relative pressure as it has not been necessary to deal with absolute values. Pressure values are usually either taken at one point over a period of time or on every node in the mesh at certain time steps. Time domain results at a single point in the mesh can be Discrete Fourier transformed to examine the frequency domain, for example looking at resonance or for use in other calculations such as near-to-far-field transformations.

Particle velocity (U) is measured by calculating the magnitude of the vector voltages in each cartesian direction of the mesh. This is expressed for 2D meshes in Equation 3.27.

$$U = \sqrt{({}^{i}V_{xp} - {}^{i}V_{xn})^2 + ({}^{i}V_{yp} - {}^{i}V_{yn})^2} \tag{3.27}$$

The direction (D) of the velocity is vector calculated by Equation 3.28 with the positive vertical direction pointing south to north and the positive horizontal direction pointing west to east.

$$D = \tan^{-1}\left[\frac{({}^{i}V_{yp} - {}^{i}V_{yn})}{({}^{i}V_{xp} - {}^{i}V_{xn})}\right] \tag{3.28}$$

The mathematical relationship between the pressure and particle velocity of the wave is shown in Equation 3.29 where P is the acoustic pressure, ρ is the medium density and c is the speed of sound in the material.

$$U = \frac{P}{\rho c} \tag{3.29}$$

This expression only holds true in the far field as the fraction: P/U is not constant in the near field due to the highly variable pressure, hence, each quantity must be considered separately.

Displaying results

Visualising propagation is possible if the pressure on every node is measured and mapped to image files such as a portable pixel map (ppm). Images in this thesis of propagating waves, for example Figure 3.13, are taken at a time to show significant propagation and features. If these images are created sequentially in time, animations can show waves physically propagating in time and space.

3.7.3 Memory Allocation

Memory allocation becomes a very important issue when 3D models are being considered. The number of nodes needed depends on how big a real life space is being modelled and the upper frequency limit of interest.

3.7.4 The TLM modelling routine

The TLM method is formulated using a programming language such as C or Fortran. Commercial tools are available such as Microstipes (http://www.microstripes com/) by Flomerics which concentrates on electromagnetic compatibility, antenna design and electromagnetics. There is greater versatility in producing a custom TLM solver but creating graphical results comparable to the commercial ones is very challenging.

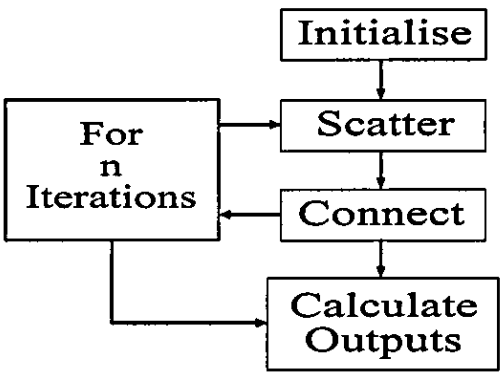

Figure 3.18: The TLM algorithm

The basic TLM algorithm is depicted in Figure 3.18. Variables are declared and the mesh is created. If inhomogeneous materials are being modelled then the stub impedances are stored for each cell. If an acoustical baffle is being modelled then the geometry is added to the mesh. The mesh is excited and the series of scatter and connect is started for a given number of iterations in a loop. Finally an output is formed in terms of a graphical representation or time domain data set. The number of iterations depends on the situation. There are no constraints when simply visualising propagation but when Fast Fourier transforming time domain results, the number of iterations must be of the form 2^n, for discrete Fourier transforms this does not matter. If examining broadband signals any resonance should be allowed to decay to a low level before Fourier Transforming otherwise resonance could be missed.

3.8 Basic validation of the technique

Here several examples using the TLM method are described. They include simple resonant cavities and a case study in bioacoustics: The Harbour Porpoise melon.

3.8.1 Resonant Cavities

Resonant cavities are a useful benchmark for comparing TLM computed results with analytical solutions. Simple meshes in two and three dimensions were constructed for the computer program used in this thesis. Perfectly reflecting boundary conditions were implemented with an impulsive excitation. The results were then compared with analytical solutions calculated using Equation 3.30 for 2D meshes and 3.31 for 3D.

2D Resonant Cavity

The analytical expression for the resonant frequencies of a 2D cavity.

$$f_{mn} = c\sqrt{\left(\frac{m}{2a}\right)^2 + \left(\frac{n}{2b}\right)^2} \tag{3.30}$$

Where m and n are termed "mode indices" and used to represent each mode, a and b are the lengths of each side of the cavity and c is the speed of sound taken as 330 m/s.

The mesh designed for the 2D resonant cavity was 60 nodes wide by 30 high and had a node separation of $\Delta\ell = 0\ 006628$ m and a time step, $\Delta t = 0\ 006628$ s, which meant that due to dispersion the maximum frequency of the mesh was 5 kHz. A delta pulse was introduced to the corner of the mesh and the simulation undertaken for 2048 time steps. The fast Fourier Transform (FFT) was taken for the second 1024 samples of the simulation giving the results in Figure 3.19.

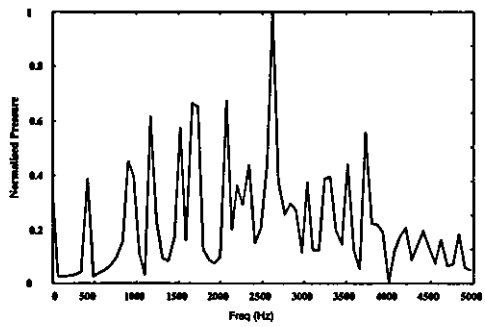

Figure 3 19· Resonant frequency response of a 2D rectangular cavity

The resonant frequencies found here are in good agreement with the analytical ones found using Equation 3.30. A comparison of resonant frequencies can be seen in Table 3.2.

3D Resonant Cavity

In the 3D situation, a rectangular cavity with rigid walls of lengths; 20 cm, 30 cm and 40 cm, and node separation of $\Delta\ell = 0\ 02$ cm and time step, $\Delta t = 3.48853 \times 10^{-5}$ s was excited with a delta pulse and pressures taken at every time step for a total 10,000. The resonant frequencies from the TLM mesh in Table 3.3 agree within roughly 0.5% of the analytical ones calculated using Equation 3.31.

Mode	Theory (Hz)	TLM (Hz)	Error (%)
10	416.667	413.8	0.69
21	1178.51	1172.43	0.52
31	1502 31	1517.26	-1.0
02	1666.66	1655.19	0.69
12	1717.96	1724.19	-0.36
32	2083.33	2068.99	0 69
23	2635.23	2620.72	0.55
43	3068.09	3034.52	1.11
71	3298.82	3310.38	-0.35
24	3498.13	3517.28	-0.55
72	3693.78	3724.18	-0 82

Table 3.2. The analytical and TLM resonant frequencies of a 2D rectangular cavity

$$f_{nml} = c\sqrt{\left(\frac{l}{2d}\right)^2 + \left(\frac{m}{2b}\right)^2 + \left(\frac{n}{2a}\right)^2} \tag{3.31}$$

Where l, m and n are termed "mode indices" and used to represent each mode, a, b and d are the lengths of each side of the cavity and c is the speed of sound taken as 330 m/s.

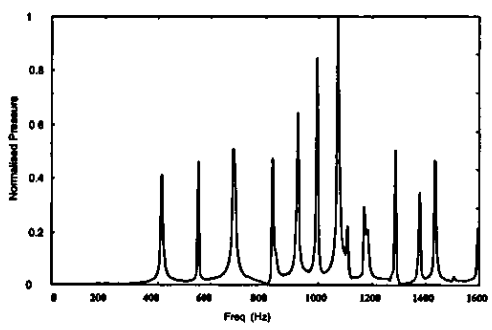

Figure 3.20. Resonant frequency response of a 3D rectangular cavity

Figure 3.20 shows the frequency response of the cavity used in the example.

Mode	Theory (Hz)	TLM (Hz)	Error (%)
001	413.8	412.9	0.22
010	551.7	552.87	-0.21
011	689.6	685.84	0.55
002-100	827.5	825.81	0.2
101	925.2	923.79	0.15
012	994.5	993.77	0.07

Table 3.3: The analytical and TLM resonant frequencies of a 3D rectangular cavity

3.8.2 *Using TLM to investigate the Melon of the Harbour Porpoise* Phocoena phocoena

McBride [3.31] first provided evidence in 1947 that marine mammals used echolocation to navigate their surroundings and hunt for food. The emission and reception methods are very complex but the use of TLM has allowed engineers to visualise sound propagation developing a much fuller understandings. In this example, wave propagation is considered in the head of the Harbour Porpoise.

The sound originates from the monkey lips dorsal bursae (MLDB) region of the head and is baffled by air sacs close by before travelling through the melon and out of the head. The melon is a structure made from fatty acids and lipids that has a graded index nature which varies the speed of sound propagation through it. Norris *et al.* [2.11] performed experiments on sections of the melon and measured the speed of sound through them and discovered that sound travelled faster towards the exterior of the melon than the interior. In practical terms this acts to beamform the sound before it emerges from the porpoise head.

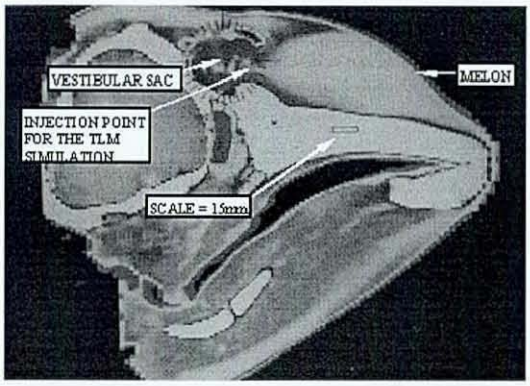

Figure 3.21: X-ray CT scan of the head of a Harbour Porpoise showing key anatomical features [3.32]

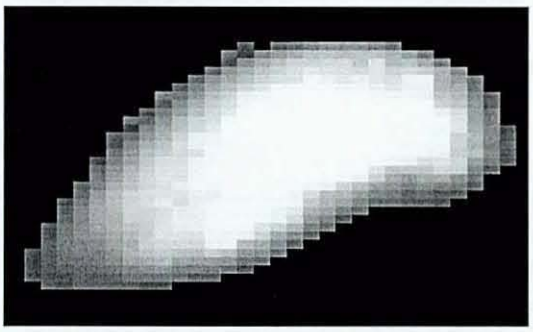

Figure 3.22: The digitised Harbour Porpoise melon as extracted from the x-ray CT data and mapped to a TLM mesh

This variation in melon density can be seen from computed tomography (CT) scans of the porpoise head performed by Ted Cranford [3.32] (see Figure 3.21). The CT scanner uses the point of intersection of two projectors to determine the attenuation of tissue at a particular point in a subject body. Depending on the resolution of the scanner the subject is split into voxels of a given size and a unit (known as "Hounsfield units" after Sir Godfrey Hounsfield who originated the idea) applied to it. This value is then converted into an impedance value for the stub in the TLM node. Figure 3.22 shows the melon as has been extracted from the full head scan in Figure 3.21 where the darker areas show faster propagation and the lighter ones slower.

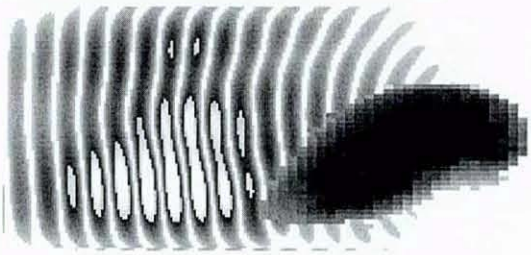

Figure 3.23: TLM simulation results showing propagation through the melon of the Harbour Porpoise

Figure 3.23 shows the wave propagation through the melon as obtained using 2D lossless TLM. The results show two phenomena, firstly the main beam of energy, depicted by the intense white areas is directed towards the bottom half of the melon. This increased signal directionality gives a greater spatial resolution which will assist hunting. Secondly, the emerging wavefronts are planar rather than spherical which implies the apparent acoustic far-field has been achieved before the click has left the melon. When operating at very close range the problem of fluctuating near-field diffraction is overcome due to this near field signal conditioning performed by the melon [3.33].

3.9 Discussion

In this chapter a number of issues relating to TLM implementation in bioacoustics have been reviewed. TLM is a multi-functional method which is capable of carrying out the task set in the thesis. TLM has the benefit of being a highly accurate method which has been proven in the study of bioacoustics in 2 dimensions. The remainder of this thesis will seek to implement a 3D model of bat hearing.

References

[3.1] V. Trenkic, C. Christopoulos, and J. G. P. Binner, "The application of the transmission-line modelling (TLM) method in combined thermal and electromagnetic problems," *Proceedings of the International Conference on Numerical Methods for Thermal Problems (Swansea)*, pp. 1263–1274, 1993.

[3.2] G. J. Partridge, C. Christopoulos, and P. B. Johns, "Transmission line modelling of shaft dynamic systems," *Proceedings of the Institute of Mechanical Engineers*, vol. 201, pp. 271–278, 1986.

[3.3] E. E. Kitsios and R. F. Boucher, "Transmission line modelling of a hydraulic position control system," *Proceedings of the Institute of Mechanical Engineers*, vol. 200, no. b4, pp. 229–236, 1986.

[3.4] D. de Cogan, *Transmission Line Matrix (TLM) Techniques for Diffusion Applications*. Gordon and Breach Science Publishers, 1998.

[3.5] P. B. Johns and R. L. Beurle, "Numerical solution of 2-dimentional scattering problems using a transmission-line matrix," *IEE*, vol. 118, pp. 1203–1208, September 1971.

[3.6] G. Kron, "Equivalent circuit of the field equations of Maxwell I," *Proceedings of the Institute of Radio Engineers*, vol. 32, pp. 289–299, May 1944.

[3.7] S. Akhtarzad and P. B. Johns, "Generalised elements for t l.m. method of numerical analysis," *Proceedings of the IEE*, vol. 122, no. 12, pp. 1349–1352, 1975.

[3.8] P. B. Johns, "A symmetrical condensed node for the TLM method," *IEEE Transactions on Microwave Theory and Techniques*, vol. 35, pp. 370–377, April 1987.

[3.9] S. Akhtarzad and P. B. Johns, "Solution of 6-component electromagnetic fields in three space dimensions and time by the t.l.m. method," *Electronic Letters*, vol. 10, no. 25/26, pp. 535–537, 1974.

[3.10] D. H. Choi and W. J. R. Hoefer, "The simulation of three-dimensional wave propagation by a scalar TLM model," in *MTT Symposium Digest, (San Francisco, CA, USA)*, pp. 70–71, IEEE, 1984.

[3.11] A. H. M Saleh and P. Blanchfield, "Analysis of acoustic radiation patterns of array transducers using the TLM method," *International Journal of Numerical Modelling: Electronic Networks, Devices and Fields*, vol. 3, no. 39-56, 1990.

[3.12] J. A. Portí and J. A. Morente, "A three-dimentional symmetrical condensed TLM node for acoustics," *Journal of Sound and Vibration*, vol. 241, no. 2, pp. 207–222, 2001.

[3.13] D. de Cogan and A. de Cogan, *Applied Numerical Modelling for Engineers.* Oxford Science Publications, 1st ed., 1997. Chapter 4.

[3.14] C. Christopoulos, *The Transmission-Line Modeling Method.* IEEE Press / Oxford University Press, 1995.

[3.15] L. E. Kinsler, A. R. Frey, A. B. Coppens, and J. V. Sanders, *Fundamentals of Acoustics.* Wiley, 4th ed., 1999.

[3.16] P. B. Johns, "The solution of inhomogeneous waveguide problems using a transmission line matrix," *IEEE Transactions on Microwave Theory and Techniques*, vol. 22, no. 3, pp. 209–215, 1974.

[3.17] J. Nielsen and W. J. R. Hoefer, "A complete dispersion analysis of the condensed node TLM mesh," *IEEE Transactions on Magnetics*, vol. 27, no. 5, pp. 3982–3985, 1991.

[3.18] J. R. Hoefer and Y. Shih, "The accuracy of tlm analysis of finned rectangular waveguides," *IEEE Transactions on Microwave Theory and Techniques*, vol. 28, no. 7, pp. 743–746, 1980.

[3.19] G. Mur, "Absorbing boundary conditions for the finite-difference approximation of the time-domain electromagnetic-field equations," *IEEE Transactions on Electromagnetic Compatibility*, vol. EMC-23, no. 4, pp. 377–382, 1981.

[3.20] J. A. Morente, J. A. Portí, and M. Khalladi, "Absorbing boundary conditions for the TLM method," *IEEE Transactions on Microwave Theory and Techniques*, vol. 40, pp. 2095–2099, November 1992.

[3.21] W. J. Hoefer, "The discrete time domain Green's function or Johns' matrix-a new powerful concept in transmission line modeling (TLM)," *International Journal of Numerical Modelling: Electronic Networks, Devices and Fields*, vol. 2, pp. 215–225, December 1989.

[3.22] A. Banai, F. Farzaneh, F. Ndagijimana, and P. Saguet, "An interpretation of instabilities in the absorbing conditions in TLM method and an improved matched termination wall," *International Journal of Numerical Modelling: Electronic Networks, Devices and Fields*, vol. 11, pp. 243–254, 1998.

[3.23] J.-P. Bérenger, "A perfectly matched layer for the absorption of electromagnetic waves," *Journal of Computational Physiology*, vol. 114, pp. 185–200, 1994.

[3.24] J.-P. Bérenger, "Perfectly matched layer for the FDTD solution of wave-structure interaction problems," *IEEE Transactions on Antennas and Propagation*, vol. 44, no. 1, pp. 110–117, 1996.

[3.25] N. Peña and M. M. Ney, "A new TLM node for Bérenger's perfectly matched layer," *IEEE Microwave and Guided Wave Letters*, vol. 6, no. 11, pp. 410–412, 1996.

[3.26] Q. H. Liu and J. Tao, "The perfectly matched layer for acoustic waves in absorptive media," *Journal of the Acoustical Society of America*, vol. 102, p. 20722082, 1997.

[3.27] L. Zhao and A. C. Cangellaris, "A general approach for the development of unsplit-field time-domain implementations of perfectly matched layers for FD-TD grid truncation," *IEEE Microwave and guided wave letters*, vol. 6, no. 5, p. 209, 1996.

[3.28] D. de Cogan, M. Morton, D. Peel, and V. Sant, "Hybrid modelling for echo location and surface characterization," *International Journal of Numerical Modelling: Electronic Networks, Devices and Fields*, vol. 14, no. 2, pp. 145–154, 2001.

[3.29] A. T. De Hoop, *Handbook of Radiation and Scattering of Waves: Acoustic Waves in Fluids, Elastic Waves in Solids, Electromagnetic Waves.* Academic Press, 1995.

[3.30] J. A. Flint, S. C. Pomeroy, and D. D. Ward, "Compact partial Huygens' surface for TLM," *Electronic Letters*, vol. 35, no. 2, pp. 132–133, 1999.

[3.31] A. F. McBride, "Evidence for echolocation by cetaceans," *Deep-sea research*, vol. 3, pp. 153–154, 1956.

[3.32] T. W. Cranford, *Functional Morphology of the Odontocete Forehead: Implications for Sound Generation.* PhD thesis, University of Santa Cruise, June 1992.

[3.33] A. D. Goodson, J. A. Flint, and T. W. Cranford, "The Harbor Porpoise *(Phocoena phocoena)*- modeling the sonar transmission mechanism," in *Echolocation in Bats and Dolphins* (J. A. Thomas, C. F. Moss, and M. Vater, eds.), pp. 64–72, Chicago: University of Chicago Press, 2004.

CHAPTER 4:
AN INVESTIGATION INTO FAR FIELD ACOUSTICS

THERE are many instances where acoustical pressure can be captured in the near field where far field measurements are actually required. For finite modelling methods it is often infeasible to model sufficient space around the object to establish far field conditions. Usually the reason for this is limitations in computer memory. Near to far field transformations are one way of achieving the desired result. This chapter details the methods used in extrapolating near field acoustical data to far field directionality patterns and details a novel way of calculating the directionality index of the particular radiator being modelled.

4.1 Near field extrapolation techniques

The near field extrapolation used in this thesis originated in 1959 by Horton, Innis and Baker at the Defence Research Laboratory (DRL) of the University of Texas after the US Navy found that far field measurements of low frequency underwater acoustics needed huge masses of water to take accurate measurements, this theory has been documented in the following reference [4.1]. They based their theory on formulae by Kirchhoff and Helmholtz and the method has been adapted by Aroyan who used the method to examine far field reception patterns of the Common Dolphin [2.3].

4.1.1 Near to far field transformation methods

The original formula (DRL method) can be seen in Equation 4.1 which relates to Figure 4.1 where S is an imaginary surface that encompasses the near field region where

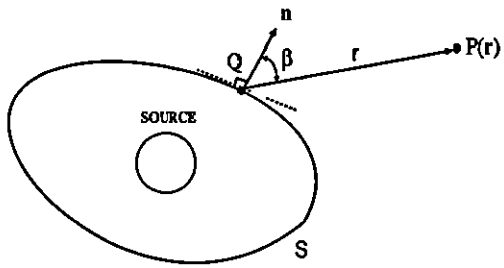

Figure 4.1: Geometry used in the DRL near to far field transformation

sound pressure levels are measured. The system can be used on both physically measured scenarios or ones in the mathematically computed domain such as those described in this thesis. It is important that a closed surface is chosen of known size and that orientation of the surface normals are known. For each point, Q, on the imaginary surface, S, the near field complex pressure, $p(Q)$, and differential complex pressure $\frac{dp(Q)}{dn}$ are extrapolated in order to calculate the far field pressures. The term $\left(\frac{e^{jkr}}{r}\right)$ represents the wave field of a point source and is necessary to ensure phase is considered at the far field point. Note that this equation is in the frequency domain, so in time domain methods such as TLM a suitable Fourier technique must be used prior to implementation

$$P(r) \equiv \oint_s \left[P(Q)\frac{\partial}{\partial n}\left(\frac{e^{jkr}}{r}\right) - \left(\frac{e^{jkr}}{r}\right)\frac{\partial P(Q)}{\partial n}\right] dS(Q) \tag{4.1}$$

The full derivation of Equation 4.1 can be seen in Aroyan's PhD thesis [2.3] where several assumptions and simplifications have been made including normalisation of the far field pressure. Here, k $(= \frac{2\pi}{\lambda})$ is the wave number and r is the absolute distance between the point on the imaginary surface and that in the far field.

$$P(\mathrm{R}) \approx \oint_s \left[\imath k\hat{\mathrm{R}} \cdot \hat{\mathrm{n}} P(Q) + \frac{\partial P(Q)}{\partial n}\right] e^{-\imath k\hat{\mathrm{R}}\,\sigma} dS(Q) \tag{4.2}$$

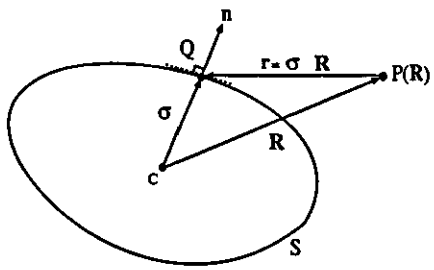

Figure 4.2: Geometry used in the Aroyan simplification of the near to far transformation

Figure 4.2 shows the geometrical layout of Aroyan's transform. The significant difference is the use of 3D vector mathematics to describe the positioning of each point. The implementation for TLM is described in the upcoming section.

An interesting alternative to this particular transformation was carried out by Hindmarsh [4.2] who investigated a hybrid routine that modelled the near field using traditional TLM methods but transformed the pressures on a 'bubble' surrounding the space using ray tracing techniques to achieve far field results. This work was unique as the 'bubble' was moving as used to investigate the effects of Doppler shift.

4.1.2 *From near to far pressure fields*

The TLM routine has been separated from the extrapolation technique in this method where near field data is calculated and stored for use in the transform. Khalladi *et al.* [4.3] published work on this matter but in the electromagnetic domain where they used the Kirchhoff integral and also a transformation based on the equivalence principle which is similar.

Near field TLM data

The near to far field transformation is easily implemented within the TLM method as a regular, cubic imaginary surface (see Figure 4.3) can be placed around the meshed area of interest. Within the software a simple cartesian indexing system can be used to move from point to point and record the necessary data. **n**, the unit normal vector is simplified in this instance with only six varying vectors, labelled, n_{xp} and n_{yn} for example on Figure 4.3. These vectors are predefined rather than calculated as required as this could become more intensive with more complicated surfaces such as an arbitrary ellipse.

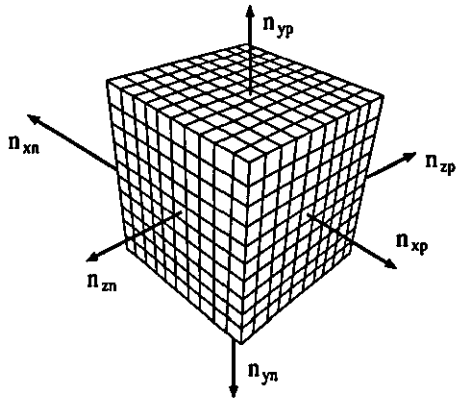

Figure 4.3: Imaginary surface indexing with normal pressure directions indicated

The complex pressure is obtained using a discrete Fourier Transform (DFT) as shown in Equation 4.3. The DFT requires less memory than an FFT (Fast Fourier transform) as the pressure at each time step does not need to be stored, only the ongoing summation need to be kept in memory. At every time step, on every point on and adjacent to the imaginary surface the complex pressure is summed as directed by the equation and the value stored. The main criteria for selecting n, the number of time steps is to ensure the steady state is reached. For sinusoidal excitation this is as soon as the initial turn on transient has passed, or for impulse excitation, when the impulse has decayed sufficiently.

$$P(Q) = \sum_{0}^{n} P(t)e^{j-2\pi ft}dt \tag{4.3}$$

A less computationally expensive method than a DFT for calculating the complex pressure is achieved using the "two equation-two unknowns method" as described by Furse [4.4]. Rather than performing a calculation on every point at every time step, just two pressure values on the same point are captured at two different time steps. It is necessary to excite just one sinusoid in the mesh of the form $P = A\sin(\omega t + \theta)$. The method works by writing a simultaneous equation for two unknowns; 2 pressures at 2 predetermined times and solving to calculate the magnitude and phase of the complex pressure. This only has to be performed once at the end of the simulation for each point on the imaginary surface.

$$\theta = \tan^{-1}\left[\frac{q_2\sin(\omega t_1) - q_1\sin(\omega t_2)}{q_1\sin(\omega t_2) - q_2\sin(\omega t_1)}\right] A = \left|\frac{q_1}{\sin(\omega t_1 + \theta)}\right| \tag{4.4}$$

Equation 4.4 shows the equation where t is one of the two time points, q is the respective pressure at each time point and ω is the standard angular frequency.

The differentiated complex pressure $\frac{dp(Q)}{dx}$, is obtained by subtracting the complex pressure at a point on the imaginary surface from the complex pressure of a normal, adjacent point, then diving by the distance between the points ($\Delta\ell$).

Near field data is captured on the imaginary surface and saved in a file for use with the far field transform. Equation 4.2 was used in this thesis where parameters in Table 4.1 were captured directly from the mesh during the numerical simulations

The far field extrapolation

Azimuthal and elevation increments were used when determining the far field pressure at point P. Figure 4.4 shows the coordinate system and Equation 4.5 describes the vector between the centre of rotation and the point P. For the far field calculator in this

Parameter	Decription
n_x, n_y, n_z	Surface normal for each point on the IS
i, j, k	Cartesian index of the point on the IS
$p(Q)$	The complex pressure on the surface
$\frac{dp(Q)}{dn}$	Derivative of the complex pressure at the surface

Table 4.1: Parameters for the near to far field transform

thesis pressure for every point was calculated using the DFT method and the integral technique already described 4.2.

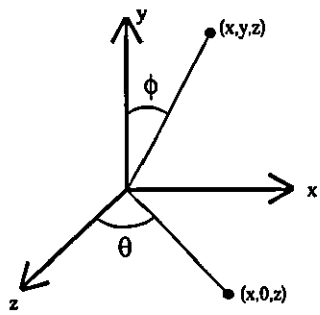

Figure 4 4: The spherical coordinate system

$$\hat{\mathrm{R}} = (\sin\theta\cos\phi, \sin\theta\sin\phi, \cos\theta) \tag{4.5}$$

4.2 TLM and near to far field transformation validation

In order to validate the TLM routine and near to far field transformation it is necessary to test the code against analytical bench marks. This section compares far field directionality patterns of acoustic dipoles and tripoles, from results calculated using analytical and numerically modelled techniques.

4.2.1 Analytical directionality patterns from point sources pressure addition and mathematical expressions

For any number of point sources, the total pressure at a point in the far field can be found by summing the contribution of each individual radiator (see Equation 4 6).

$$\sum \frac{P_n}{|R_n|} e^{j(k|R_n|-\omega t)} \tag{4.6}$$

An example of the layout for two point sources representing a dipole can be seen in Figure 4.5, where d is the separation between the two radiators and PC is the phase centre that has to be included when calculating the vectors R_0 and R_1.

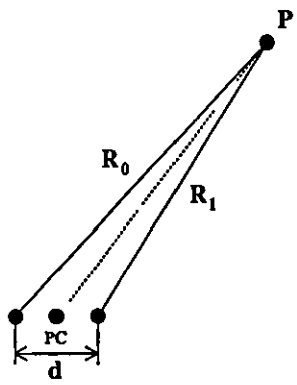

Figure 4.5: Geometry for summing pressures from two points sources in the far field

With the magnitude and phase of pressure P and time t assumed to be 1 then Equation 4.6 simplifies to Equation 4.7 for a dipole.

$$e^{j(R_0-\omega)} + e^{j(R_1-\omega)} \tag{4.7}$$

The expression for R_0 can be seen in Equation 4.8 where points are identified by their location in cartesian coordinates. R_1 is similar to this with the difference being the addition of $\frac{d}{2}$ rather than subtraction. In this equation, p_x represents the x cartesian coordinate of the far field point P, and P_{cx} represents the x cartesian coordinate of the point at the centre of rotation. This is similar for the other two directions; y and z.

$$R_0 = \sqrt{\left[P_x - \left(P_{cx} - \frac{d}{2}\right)\right]^2 + \left[P_y - \left(P_{cy} - \frac{d}{2}\right)\right]^2 + \left[P_z - \left(P_{cz} - \frac{d}{2}\right)\right]^2} \tag{4.8}$$

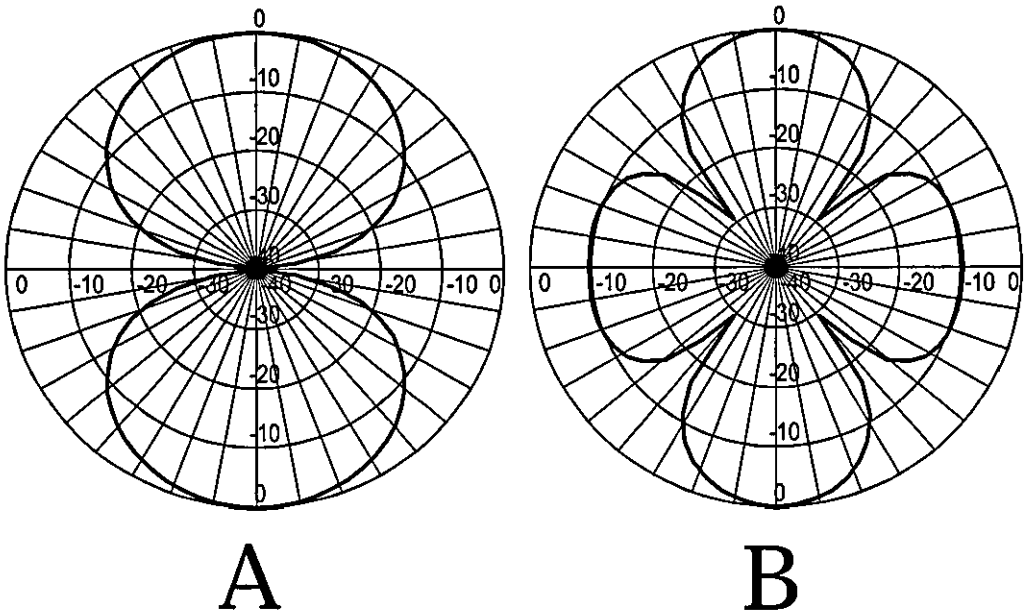

Figure 4.6. Half lambda separated dipole (A) and lambda separated tripole (B) directionality patterns from adding the pressure of point sources

Figure 4.6 shows the 2D cross section of the directionality pattern of a half lambda separated dipole and a lambda separated tripole. Analytical expressions for these directionality patterns are often simplified and quoted in text books. For example the equation describing the directionality ($d(\theta)$) of a lambda separated dipole is defined by Nagy [4.5] and is shown in Equation 4.9, a tripole is shown in Equation 4.10.

$$d(\theta) = \cos\left(k \sin\theta \frac{d}{2}\right) \tag{4.9}$$

$$d(\theta) = \frac{1}{3}\left[2\cos\left(k\sin\theta\frac{d}{2}\right) + 1\right] \tag{4.10}$$

These 2D patterns will be used to validate the TLM method in the forthcoming section.

4.2.2 Directionality patterns using the TLM method

In order to show the TLM routine working accurately in conjunction with the near to far field transformation, analytical directionality patterns are plotted along side the numerically generated ones. Data sets are collected from the near field TLM routine and transformed into the far field using the Helmholtz equation where 2D directionality patterns can be created allowing for visual comparison of the two methods.

Figure 4.7 shows the directionality pattern for a lambda separated dipole generated using an analytical expression (Equation 4.9) and numerically using the mathematical TLM and near field extrapolation routines. Figure 4.8 displays data from the identical methods but for a half lambda separated dipole. The errors at 90° and 270° in Figure 4 8 are due to difficulties with the plotting program in handling $\log(\alpha)$ as $\alpha \rightarrow 0$ and $log(\alpha) \rightarrow -\infty$. There is excellent agreement between the numerically generated and analytical solutions. The discrepancies seen are mainly due to dispersion in the mesh as the maximum frequency allowable was used to excite the mesh. The mesh implemented was of cubic shape with 180 nodes in each cartesian direction. The excitation source was a single sinusoid on one node in the centre of the mesh at 115 kHz with a node separation of 0.29 mm. The imaginary surface was placed half way between the centre and the mesh edge so any inaccuracies in the boundary conditions would not affect the result.

4.3 Pinna performance metrics

This section details the parameters needed to quantitively describe performance of the pinna in question. Calculating these parameters gives a means to allow the comparison

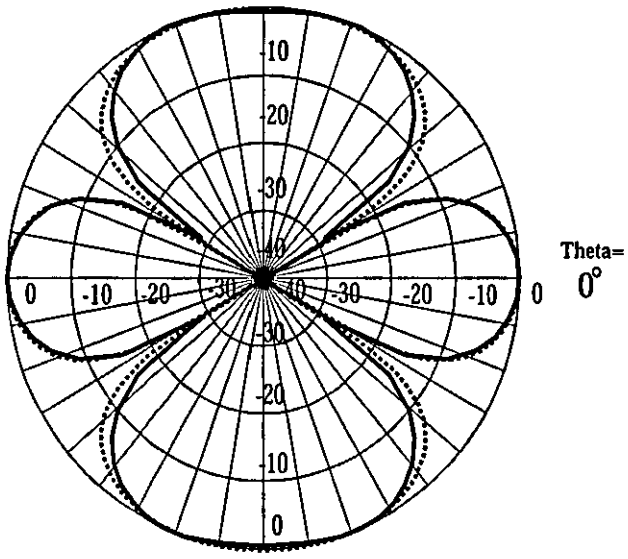

Figure 4.7: Directionality of a lambda separated dipole from analytical solution (dashed line, Equation 4.9) and near field TLM modelling with NFFF transformation (full line)

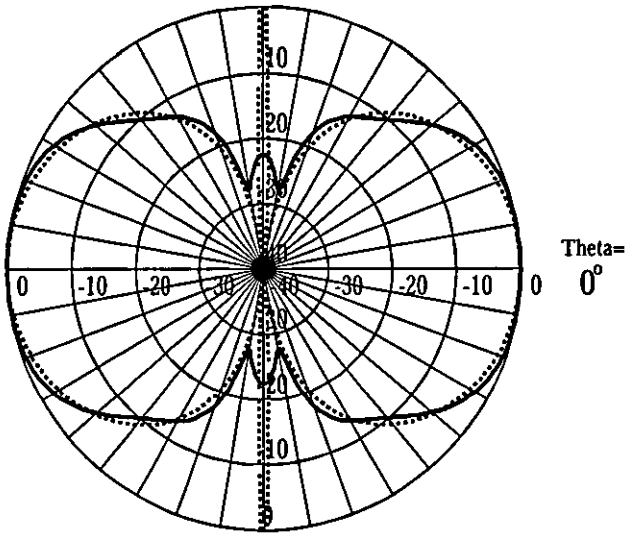

Figure 4.8: Directionality of a half lambda separated dipole from analytical solution (dashed line, Equation 4 9) and near field TLM modelling with NFFF transformation (full line)

between other pinna and geometric shapes acting as radiators.

4.3.1 Directionality index

Directionality describes the nature of the receiving or transmitting energy distribution of an acoustic baffle, in other words, "is the beam more concentrated in one direction than another?" Baffles are classified by way of three categories depending on the nature of their directionality; *directional* devices radiate or receive more energy in some directions than others, *omnidirectional* devices are a specific type of directional device in which there is directionality in one plane (azimuthal or elevation) but not the other, and *isotropic* radiators are hypothetical devices which radiate uniformly is all directions.

4.3.2 Devising directionality from beamwidth

Beamwidth is directly related to directionality, in simplistic terms it describes the amount of radiation spread. This is typically defined as the angle between the two half power points (the -3dB points) on a polar plot of the device being measured, although -10 dB is sometimes used and indicated in the units. Values for both the azimuthal and elevation plane can be measured which in turn allows a value of directionality index to be approximated, Figure 4.9 shows how this is achieved by approximating the area of the plot above the -3 dB half power point. A rectangle (Figure 4.9(A)) with lengths of sides a and b or an ellipse (Figure 4 9 (B)) with two differing radii a and b can both be used in order to approximate a directional beam.

From Figure 4.9 the lengths a and b are described by the following: $a = r \sin \mathrm{BW}_\theta$ and $b = r \sin \mathrm{BW}_\phi$. The resultant areas are also described by the following; area of rectangle (Figure 4.9(A)) $= a \times b$ and the area of the ellipse (Figure 4.9(B)) $= \pi \times \frac{a}{2} \times \frac{b}{2}$.

Table 4.2 summaries three popular equations describing the directionality index of a directionality pattern with a given azimuthal and elevatory half power beamwidth. These approximations will later be used to estimate the directionality of the bat pinna under

Approximation	Directionality
A: Elliptical approximation	$= \frac{4\pi}{\sin\theta \sin\phi}$
B: Rectangular approximation	$= \frac{16}{\sin\theta \sin\phi}$
C: Circular Approximation	$= \frac{4}{tan^2(\frac{\alpha}{2})}$
D: Stegens improvement	$= \frac{32600}{\sin\theta \sin\phi}$

Table 4.2. Three approximations for estimating directionality

investigation. Stegen [4.6] among others describes the inaccuracies in the approximations and notes the important assumption of minimal sidelobes in the directionality patterns. He improved the approximation for a radiating line array which can be seen in Table 4 2(D).

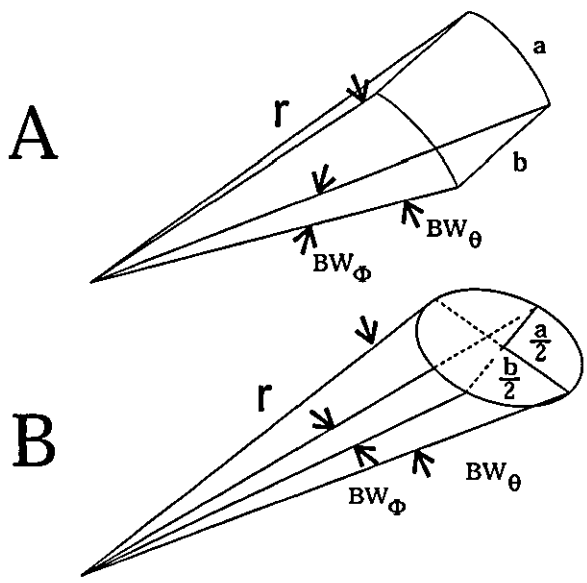

Figure 4.9. Azimuthal (BW_ϕ) and elevation (BW_θ) beamwidth of a directionality pattern

Directionality is an important feature when used in SONAR and echolocation as it limits spatial resolution. The smaller the beamwidth the better the spatial resolution, a phenomena similar to that of image quality where the more pixels per square inch the better the quality. Other advantages include an increase in signal range as energy

density is greater and there is less susceptibility to external noise sources due to a narrower angle of reception. The converse aspect of this is that more emissions have to be scanned in order to cover an equivalent area to a less directive device.

4.3.3 Comparing TLM results to directionality estimations

In this section an example will be given where directionality will be calculated using a TLM routine and compared with analytical (precise) results. This example will use a radiating line of length, L where directionality ($d(\theta)$) is described using Equation 4.11 (where k is the wave number).

$$d(\theta) = \frac{\sin(\frac{1}{2}kL\sin\theta)}{\frac{1}{2}kL\sin\theta} \tag{4.11}$$

Figure 4.10 shows the polar plot of a 4λ long radiating line source in three different guises. Figure 4.10(A) refers to sound pressure (absolute value), Figure 4.10(B) refers to sound power (RMS value) and Figure 4.10(C) refers to the dB value (pressure normalised to the maximum pressure). For this type of radiator the directionality pattern is symmetrical meaning azimuthal and elevation beamwidth is identical, in this case approximately 12.5° which can be measured from each plot.

Urick [4.7] describes Equation 4.11 along with an exact analytical expression for directionality (Equation 4.13). Stegen [4.6] goes on to derive equations for the half power beamwidth of the radiator (Equation 4.12) and an expression to convert the directionality from the 2D case to 3D (Equation 4.14).

$$BW = 50.9\frac{\lambda}{L} \tag{4.12}$$

$$G_\theta = G_\phi = \frac{2L}{\lambda} \tag{4.13}$$

$$G_{3D} = \pi G_\theta G_\phi \tag{4.14}$$

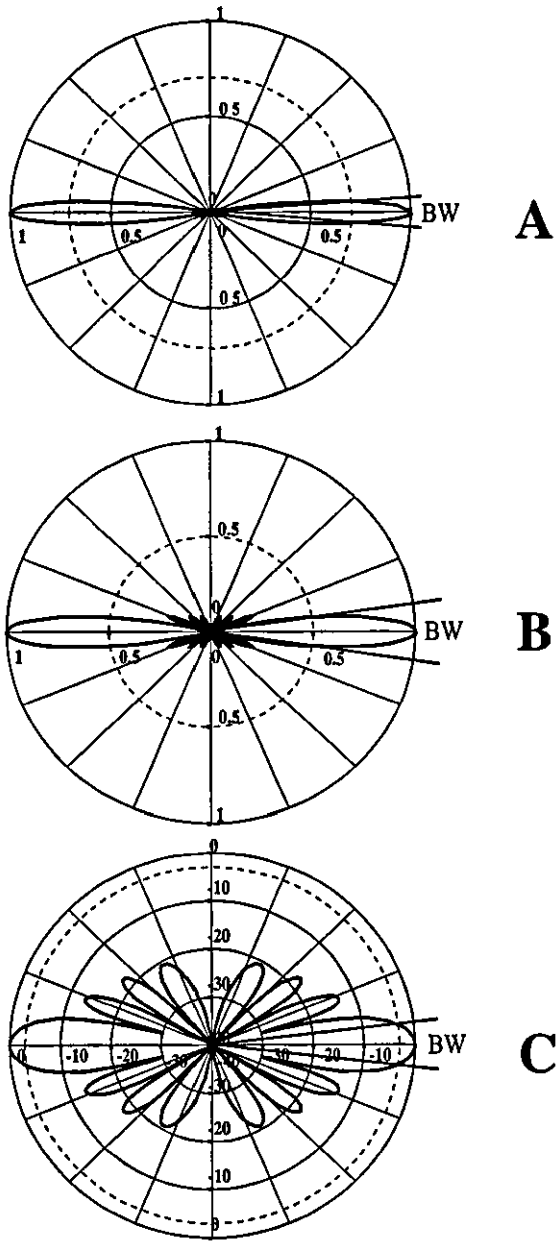

Figure 4.10. An example polar plot of the analytical solution of a 4λ long radiating line array showing A; sound pressure, B; sound power and C, sound power on a decibel scale (results are obtained from the analytical expression).

Beamwidth and directionality for the radiator are summarised in the following two tables:

- Table 4 3 simply compares the measured beamwidth with an analytical value (Equation 4.12) which is used in the directionality calculations.
- Table 4.4 summarises the directionality values calculated from the three methods as indicated:

1. The analytical solution from Equation 4.13 and Equation 4.14.
2. An estimation using the measured beamwidth and the expression in Table 4.2(A).
3. An improved estimation using Stegen's work (Table 4.2(D)).

Source	Beamwidth
Measured	12.5°
Analytical	12.7°

Table 4.3: Comparing the measured and analytical beamwidth of a radiating line array

Method	Directionality
1. Analytical (Equations 4.13 and 4.14)	23.03 dBi
2. Approximation using Table 4.2(A)	24.22 dBi
3. Stegen's approximation	23.2 dBi

Table 4.4. Comparing the directionality estimates from different methods

4.3.4 *Acoustic directionality index*

Numerically calculating directionality of radiators such as acoustic transducer arrays and horns from first principles, begins with calculating pressure at points on an imaginary sphere in the far field. The traditional method for defining these points is to increment phi and theta linearly which would give a point distribution like that in Figure 4.11. Note how this creates a non-uniform point distribution where each point is not

equidistant from neighbouring ones and area representation by each point is again, not equal. From Figure 4.11 it can be seen how points near the pole of the sphere are more densely packed than those around the equator. The consequence of this distribution is the summation of the pressures in the far field could be inaccurately estimated dependant on the direction of any main lobes. For instance, a main lobe pointing towards a densely packed area of far field points (ϕ and θ = 0°) would equate to a higher value of total pressure than if it was directed towards a lower density (ϕ and θ = 90°). This is due to a higher proportion of points tending to a maximum pressure being summed together, rather than the sum of low pressure values. Two methods of overcoming this issue will be discussed, one is well established whereas the other has been developed during this study.

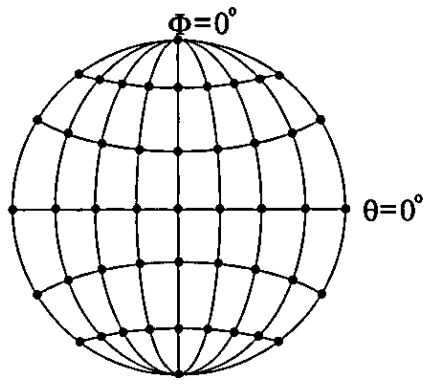

Figure 4.11. Showing the unequal area representation of points as defined by longitudinal and latitudinal line intersections

Overcoming the unequal area issue traditionally

The traditional method of overcoming the problem of an unequal pressure density is to weight those far field points determined by linearly incrementing phi and theta by a given factor. By applying a coefficient; $\sin(\theta)$ to the pressure at a point in the far field, pressure density becomes evenly distributed as illustrated from the equality, $0 < \sin(\theta) < 1$, as theta shifts from zero towards 90°. In short, points in a densely packed area are given a coefficient that tends to zero with the converse being true

for those points in a more sparse area. A brief derivation follows starting with Equation 4.15 that describes the directionality of a radiator as the ratio of sound intensity in a given direction to the sound intensity integrated over the whole sphere. Note this thesis chooses the given direction as that which gives a maximum intensity as described using the $'$ notation in the parameters of the numerator. The integral in the denominator represents the total power radiated in every direction which can be described numerically: $r^2 \sin\theta d\theta d\phi$ and introduces the weighting factor $\sin\theta$.

$$d(\theta', \phi') = \frac{I(r, \theta', \phi')}{\frac{1}{4\pi r^2} \oint I(r, \theta, \phi) \cdot ds} \tag{4.15}$$

The exact average intensity is given in Equation 4.16 with the numerical version shown in 4.17.

$$I_{Av} = \frac{1}{4\pi r^2} \int_{\phi=0}^{\phi=2\pi} \int_{\theta=0}^{\theta=\pi} I(r, \theta, \phi) r^2 d\theta d\theta \tag{4.16}$$

$$\sum_{\phi=0}^{M} \sum_{\theta=0}^{L} P^2(\theta, \phi) \sin\left[\frac{\pi\theta}{L}\right] \left(\frac{\pi}{L}\right) \left(\frac{2\pi}{M}\right) \tag{4.17}$$

The numerical equivalent (Equation 4.17) introduces M and L which are the number of increments in the planes represented by ϕ and θ respectively and P which is pressure (P^2 is acoustical power). A given example determines the directionality of an acoustic dipole. The exact value determined by Equation 4.16 is $\frac{1}{3}$ where the numerical approximation (Equation 4.17) gives 0.325 for values of 10 and 20 for L and M respectively. The approximation improves as M and L increase although the computation time does too.

A novel way of calculating directionality index

From the definition of directivity index in the previous section (Equation 4.15) the average power per unit area is to be calculated. This new method takes a different approach to calculating this value by placing far field points in an equal area segment before

pressure is calculated. This simply means that the average power is proportional to the sum of all the power over the number of points. This calculation is not valid when phi and theta are linearly incremented for the reasons already summarised. A crucial part of the investigation deals with the distribution of these points and whether every point is equidistant from neighbouring ones. This is discussed in the next section (4.3.4).

$$d(\theta,\phi) = \frac{nP(\theta,\phi)^2_{max}}{\sum_{N=0}^{N=n-1} P(\theta,\phi)^2_N} \tag{4.18}$$

The new method is described in Equation 4.18 where N is the number of points and P is the pressure. A brief implementation of the method describes the directivity of the same dipole used in the previous section and calculates to be 0.336 using 100 equally space points. Again, this estimation improves as the number of far field points increases and is slightly more accurate than the traditional method. A much more comprehensive validation is undertaken with data extracted from TLM simulations in a later section.

Comparing the two methods

There are several advantages to be considered of the new method over the traditional one. These include:

- It gives the same accuracy of result in the directive gain calculation, regardless of the boresight direction. This is particularly appealing when the direction of maximum directivity is not along one of the coordinate axis.
- It is more efficient as high point densities are not needed near to the z-axis.
- The individual contributions can simply be summed to generate the integral avoiding the need to perform extra calculations to include the weighting factor.

However, there are several disadvantages:

- The coordinates are not conveniently positioned, meaning in mechanical and visualisation circumstances it would be necessary to find a logical method for

traversing the points. There is no such issues for numerically computed far field radiation patterns since pressure can be calculated at any point on the sphere.

- The computations are expensive for generating the point coordinates. However, this need only be executed once for a given number of desired far field points.

Alternative far field points

Although the idea sounds simple, there has been some debate about the best way to space N points, equally on the surface of a sphere. Two popular methods use trigonometry (the Fejes Tóth Problem) and the theory of repelling charges (known as the Thomson Problem), but all appear iterative and in general rather inefficient. Other specific methods are "the Hypercube rejection method" and "archimedes hatbox". Edmundson [4 8] looks specifically at the charge on points and how it varies depending on the number of points.

$$E = \sum_{i>j}^{N} \frac{1}{\mid x_i - x_j \mid} \tag{4.19}$$

Equations 4.19 describes the simple relationship between total charge and the inverse of distance between two point charges where the summation combines the total energy of the system as formulated by Thomson [4.9]. E is the total charge, $x_i - x_j$ represents the distance between two points and N is the number of charges, when the expression is a minimum all points are equally spaced.

The method implemented for the purposes of this thesis used the repelling nature of identically charged particles. The algorithm initially distributes N number of points on a sphere, randomly with a fixed radius from the centre and common charge on each allowing mutual inverse-square repulsion. By performing calculations involving charge and distance between every point, the force as a function of distance will eventually become equal and the system will become stable as the position of each particle converges to a fixed location. Damping methods were utilised to prevent charges from oscillating and further decreasing efficiency and a check method for identical positioning was

also implemented. The algorithm stopped iterating when the convergence factor between each point was suitably low enough when the varying distance between points was negligible.

Validating the new directionality index calculation

Three test routines for the validation of the numerical integration method are presented here. Two estimate the directionality index of a radiating array of n, half lambda spaced point sources and the other predicts the DI of a radiating continuous line of different lengths. An analytical expression describing the directionality index of radiating point sources is described in Waite [4.10] and can be seen in Equation 4.20. Equation 4.21 shows the expression used to determine the polar plot of such a radiator, where n is the number of points and d is the separation between them.

$$d = 10 \log n \tag{4.20}$$

$$d(\theta) = 10 \log \left[\frac{\sin(n\pi d \backslash \lambda \sin\theta)}{n \sin(\pi d \backslash \lambda \sin\theta)} \right] \tag{4.21}$$

Pressure at equi-spaced far field points with coordinates, (θ, ϕ), is calculated using either the analytical expressions for far field pressure, or using the TLM routine and near field extrapolation. As the radiator is symmetrical, ϕ is actually ignored although it is referred to due to the patterns being calculated in three dimensions. Table 4.5 shows the estimated directionality index using the analytical method and a variable number of points in the far field for the n element radiating array. It can be seen how the estimation tends towards the analytical value as the number of the points increases. This is due to the increase in resolution as more points allows more of the pattern features to be extracted.

Figure 4.12 shows the polar pattern for each of the element configurations. The increase in directionality index can be visually seen as the number of points increase and the beamwidth reduces.

n	Analytical DI (dBi)	DI(10) (dBi)	DI(50) (dBi)	DI(100) (dBi)	DI(500) (dBi)	DI(1000) (dBi)	DI(2000) (dBi)
2	3	3.74	3.16	3.1	3.03	3.02	3.015
3	4.77	6.25	4.98	4.9	4.8	4.78	4.78
5	6.99	8.45	7.28	7.17	7.04	7.01	7.00
7	8.45	9.02	9.1	8.45	8.51	8.48	8.47
9	9.5	8.63	10.56	9.45	9.62	9.58	9.56

Table 4.5: Directionality indexes of five different, n element, half lambda spaced radiating point source arrays using varying numbers of equi-spaced, far field points distributed on an imaginary sphere

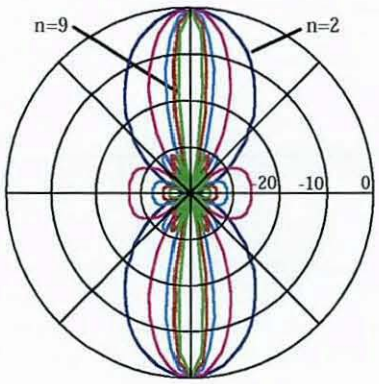

Figure 4.12: Polar plots of n=2, 3, 5, 7, and 9 radiating, half lambda separated elements distributed on an imaginary sphere

Table 4.6 compares the estimated directionality index with the analytical values for the radiating line. Analytical values were calculated using 10 log (Equation 4.13). Again it can be seen how the approximation improves with a greater number of far field points and that with only 10 points, the estimation is highly unpredictable.

Figure 4.13 shows the polar pattern for each length of line determined using Equation 4.11. The increase in directionality index can again be visualised as the length increases and the beamwidth reduces.

Table 4.7 compares analytical directionality and the equal-area method directionality

L	Analytical DI (dBi)	DI(10) (dBi)	DI(50) (dBi)	DI(100) (dBi)	DI(500) (dBi)	DI(1000) (dBi)	DI(2000) (dBi)
1	3.01	4.29	3.62	3.55	3.47	3.46	3.46
2	6.02	8.5	6.51	6.41	6.28	6.26	6.25
4	9.03	8.91	10.04	9.07	9.21	9.18	9.16
8	12.04	7.17	12.7	10.97	12.02	12.16	12.13

Table 4.6: Directionality indexes of four radiating continuous lines of different lengths (L) using varying numbers of equi-spaced, far field points

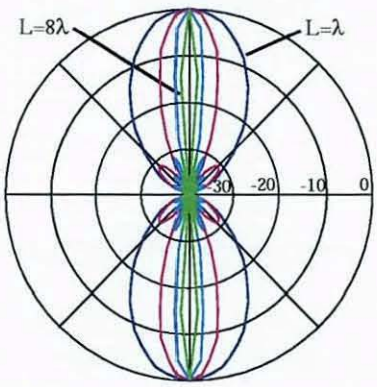

Figure 4.13: Polar plots of line length, L=1, 2, 4, and 8 lambda long continuous line radiators

using data captured from the TLM method, for the n-element array in question. The TLM mesh was 81 nodes in each cartesian direction with a cutoff frequency of 115 kHz. Half-lambda separated elements were 5 nodes apart and the mesh was excited at the maximum frequency with a continuous sinusoid. The near to far field transformation used 2000 equi-spaced points on the surface of the far field sphere. Directionality was calculated using Equation 4.6 and the DI calculation were as described previously.

Figure 4.14 visually shows the similarity between values calculated using the new, equal area method and the analytical expressions. The method itself is an approximation which will lead to differences against the analytical solutions. Other sources of error include dispersion in the TLM mesh and numerical errors in the TLM routine and far field extrapolation.

n	Analytical DI (dBi)	Calculated DI (dBi)
2	3	3.68
3	4.77	5.2
5	6.99	6.92
7	8.45	9.25
9	9.5	9.88

Table 4.7: Directionality index of five different, n element, half lambda spaced radiating point source arrays using the equi-spaced point method with 2000 points

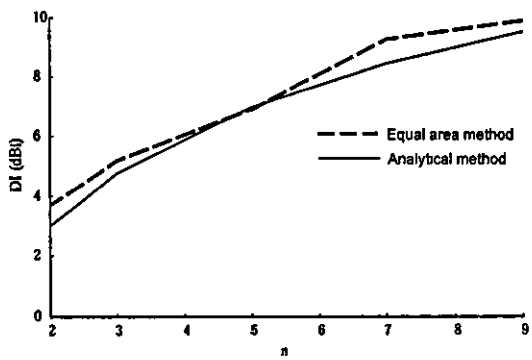

Figure 4.14: A graph comparing analytical and approximated DI of an n element, half lambda spaced radiating point source arrays using the equi-spaced point method with 2000 points

4.4 Discussion

It has been shown that patterns calculated via TLM and far field extrapolation techniques are in good agreement with analytical solutions. The facility to model in the near field and project the data is essential for the specimens to be simulated in this research.

References

[4.1] R. J. Bobber, *Underwater Electroacoustic Measurement*, pp. 193–195. Peninsula, 1988.

[4.2] D. Hindmarsh, *Modelling of the Automotive Pass-By Noise Test Using Transmission Line Matrix Techniques*. PhD thesis, School of Computing Sciences, The University of East Anglia, 2004.

[4.3] M. Khalladi, J. A. Morente, J. A. Portí, and G. Gimenez, "Two near- to far-zone approaches for scattering problems using the TLM method," *IEEE Transactions of Antennas and Propagation*, vol. 41, pp. 502–505, April 1993.

[4.4] C. M. Furse, "Faster than Fourier: Ultra-efficient time-to-frequency-domain conversions for FDTD simulations," *IEEE Antennas and Propagation Magazine*, vol. 42, pp. 24–34, December 2000.

[4.5] P. B. Nagy, "Acoustic radiators." http://www.ase.uc.edu/ pnagy/ClassNotes/. Lecture notes from the internet.

[4.6] R. J. Stegen, "The gain-beamwidth product of an antenna," *IEEE Transactions on Antennas and Propagation*, vol. 12, pp. 505–506, July 1964.

[4.7] R. J. Urick, *Principles of Underwater Sound*. California: Peninsula Publishing, 3rd ed., 1967.

[4.8] J. R. Edmundson, "The distribution of point charges on the surface of a sphere," *Acta crystallographica*, vol. A48, pp. 60–69, 1992.

[4.9] J. J. Thomson, "On the structure of the atom," *Philosophical Magazine*, vol. 7, p. 237, 1904.

[4.10] A. D. Waite, *SONAR for Practicing Engineers*. Thomas Marconi Sonar Limited, second ed., 1996.

CHAPTER 5:

INVESTIGATING THE DIRECTIONALITY OF BAT PINNA

NUMERICALLY modelling and analysing the antenna properties of the Rhinolophus rouxii pinnas require the implementation of the previously discussed theories and techniques. The TLM mesh must incorporate the pinna geometry, have accurate absorbing boundary conditions and pass precise data of the pressure and pressure derivative to the near to far field transformation routine.

It will be shown that by comparing pinna directionality with that of radiating aperture approximations, pinna can be explained by standard theory in many cases. This chapter reviews the aperture approximation theory and utilises data from Obrist *et al.* [5.1] to investigate pinna as radiating apertures- the theory of reciprocity [5.2] is used to discuss the reception properties of bat pinna. The theory states that the mutual impedance of a first circuit due to a second is the same as the mutual impedance of the second circuit due to the first. Or in terms of acoustic theory, the relationship between an oscillating object and the resulting pressure field is unchanged if there is an interchange between the points where the object is placed and where the field is measured.

Physically reproducing the pinna has allowed measurements to be made on these specimens where directionality index and beamwidth can be measured. These results are discussed and compared to those achieved from the numerical modelling techniques.

5.1 Bat pinna approximated as a radiating aperture

The complex shape and vast range of sizes and diversity of geometrical features between species makes the study of bat pinna fascinating yet highly daunting. The receiving system of echolocating bats begins at the pinna where sound is directed towards the middle and inner ear for neural processing. The pinna can be examined as an antenna type device or acoustical horn from where it can be described quantitatively in terms of directionality index and beamwidth. The factors determining these features lie with the geometric shape and wavelengths of sound applied. Obrist *et al.* [5.1] performed a very thorough analysis of the properties of post mortem ears which entailed measuring the directionality, and aperture height and width of pinnae from many species of bat. Their analysis has emphasised the wide degree of variability in operating frequency and morphology between species and this is reflected in the differing directional properties measured. One thing missing from Obrist *et al.* [5.1] was an attempt to carry out basic calculations of the acoustic performance in order to compare with their measurements.

A similar approximation has also been undertaken by Guppy and Coles [2.22] who investigated the amplification of the incoming sound wave by the pinna of the Australian false vampire bat (*Macroderma gigas*) and Gould's long eared bat (*Nyctophilus gouldi*). From pressure measurements at the mouth of the pinna and at the tympanic membrane region they calculated the directionality using the ratio of the values. Measurements were taken from both the pinna specimen and conical horn approximations as defined in Beranek [5.3] and the results compared. They found at low to medium frequencies the result trends were similar with the pinna behaving like an acoustical horn. These specimens have relatively large pinna compared to other bats which have been developed for their gleaning type of hunting [5 4]. These larger pinna allow the detection of lower frequencies of sound as they are able to receive longer wavelengths. This also improves their hearing range as these lower sound frequencies travel further in air than higher ones.

5.1.1 The aperture approximation

Figure 5.1 illustrates the parameters for approximating the directionality of a rectangular ($D(Rec)$) and circular ($D(Circ)$) aperture respectively, where d_λ represents the diameter of the circle in terms of wavelengths and a_λ and b_λ represent the lengths of the sides of the rectangle in terms of wavelength.

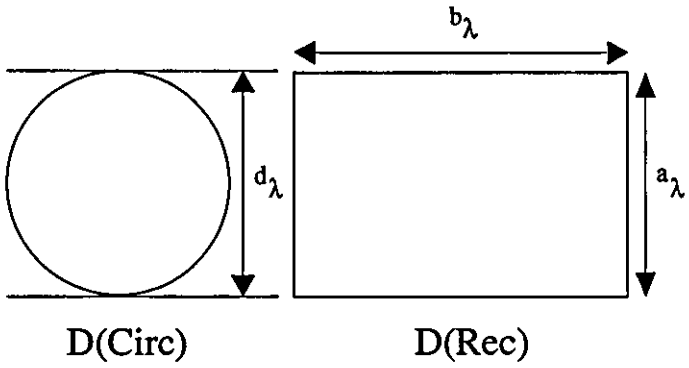

Figure 5.1: Approximations for a circular and rectangular radiating aperture

Equations 5.1 and 5.2 show the directionality for the circular and rectangular aperture respectively where D is expressed in terms of decibels over the equivalent isotropic case, dBi.

$$D(Circ) = 10\log_{10}(\pi^2 d_\lambda^2) \tag{5.1}$$

$$D(Rec) = 10\log_{10}(4\pi a_\lambda b_\lambda) \tag{5.2}$$

These aperture approximations were used to estimate the directionality index of each pinna from the appropriate dimensions measured by Obrist *et al.* [5.1]. In Table 5.1 the measurements are reproduced alongside these estimates based on a circular aperture with diameter a corresponding to the height, D(H); a circular aperture with diameter

corresponding to width, D(W); and a rectangular aperture with width and height identical to the pinna width and height, D(Rec). The species tabulated in Table 5.1 are a subset of those covered in [5.1] and were selected by virtue of the species being a known transmitter of CF (continuous frequency) signals. F in the table represents the frequency at which the directionality index were measured.

It is not being claimed that pinna can be fully classified by this simple approximation but it can be seen how the measured directionality of several species closely matches that of the approximation; this data is reproduced for visual comparison in Figure 5.2 where the numbers on the x-axis refer to the species as labelled in Table 5.1.

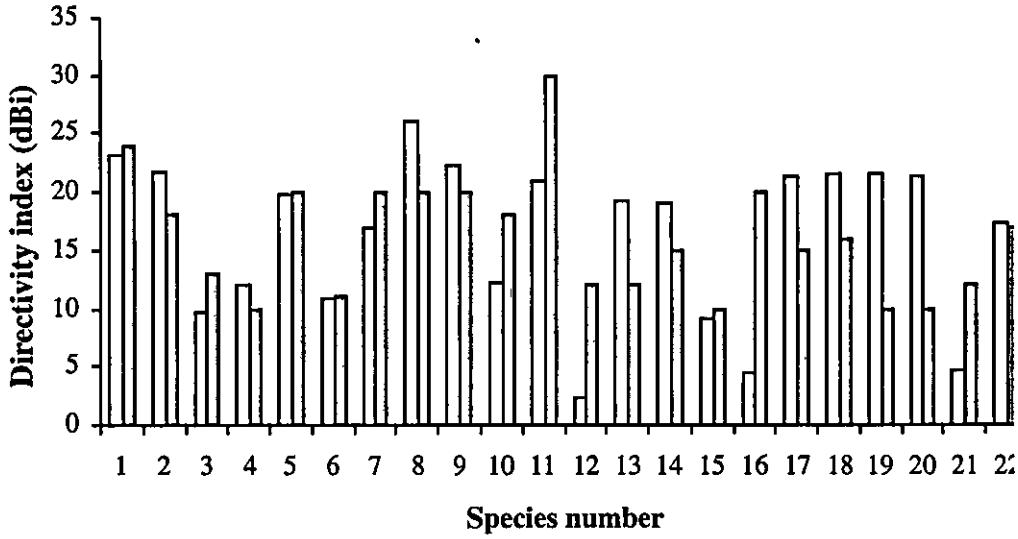

Figure 5.2: Graphical comparison between the directionality of a rectangular aperture (white bars) and the measured directionality (shaded bars). The species numbers correspond to those quoted in Table 5.1

5.1

Where the directionality of species is significantly different from that of the approx-

No.	Species	D(H)	D(W)	D(Rec)	D(M) [5.1]	F (kHz)	CF Range (kHz)
1	*Rhinolophus rouxii*	23.48	20.74	23.17	24	85	72-79
2	*Rhinolophus eloquens*	8.87	8.41	9.7	13	15	80-100
3	*Rhinolophus clivosus*	12.11	9.78	12.01	>10	25	70/100
4	*Rhinopoma hardwickei*	20.67	17.02	19.90	20	65	35
5	*Saccopteryx bilineata*	13.03	6.59	10.87	<10	45	45-50
6	*Rhynchonycteris naso*	18.56	13.03	16.86	11	105	105
7	*Asellia tridens*	25.96	24.09	26.09	20	135	111-124
8	*Cloeotis percivali*	20.55	21.96	22.31	20	165	212
9	*Hipposideros caffer*	10.43	12.01	12.28	18	35	145
10	*Hipposideros lankadiva*	20.91	19.06	21.04	30	45	70
11	*Otomops martiensseni*	12.84	7.57	11.27	12	14	13-15
12	*Tadarida brasiliensis*	19.97	16.45	19.24	12	70	45
13	*Tadarida macrotis*	23.14	12.94	19.10	15	55	21/35
14	*Tadarida pumila*	8.72	7.51	9.17	≤ 10	25	35-55
15	*Mormoops megalophylla*	4.28	2.62	4.51	20	20	50-60
16	*Pteronotus gymnonotus*	23.20	17.47	21.40	15	105	50-55
17	*Pteronotus parnellii*	23.71	17.16	21 50	16	95	60
18	*Pteronotus personatus*	19.04	14.72	17.94	<10	82	82
19	*Noctilio albiventris*	23.90	16.60	21.31	10	75	65-75
20	*Noctilio leporinus*	7.42	≈ 0	4.75	12	15	56-59
21	*Myotis evotis*	19.7	12.94	17.38	17	55	50-63

Table 5.1: Pinnae directionality approximations produced by assuming a circular or rectangular aperture

imation, there is an indication that there are more complex explanations arising and that further investigation is necessary. A species such as the subject of this thesis, the Rufous Horseshoe bat (species number 1) show good correlation between rectangu-

lar approximation and measured directionality and these results will be compared with directionality calculated from numerical modelling. Species such as *Mormoops megalophylla* has a significantly higher directionality than the predicted one which would suggest either that there are problems with the physical measurements, or that there are some other factors. This particular species of bat was chosen as the main subject for several reasons; firstly part of it's emission was constant frequency meaning sets of simulations were only undertaken for one frequency. A simple sinusoid could be used for the excitation of the TLM mesh and a single frequency used in the DFT for the near to far field transform. Choosing an ideal single frequency from a modulated call could have proved difficult when trying to conclude findings of the pinna in question as each frequency would have given a different frequency response. The measured and approximated gains by means of radiating aperture were very similar. This suggested the response of the pinna was unlikely to supply and abnormal results which would have made validating numerically modelled results difficult. It can be seen how the tragus can be a major anatomical feature of some bat pinna. If the tragus was to be such a determining factor to the directionality pattern, would aperture approximations be invalid as they do not take into account this feature?

5.2 Pinna data for numerical modelling

3D images of the subject bat pinna to be modelled were captured using x-ray computer tomography. This technique of using x-ray data for modelling was adopted previously in bioacoustics on the melon of the common dolphin by Aroyan [2.3] using data provided by Cranford [3.32]. There is an interesting comparison between the two models of a dolphin melon and bat pinna. Although both models have a maximum frequency of the order of 10^5 Hz, the dimensions differ significantly due to the transmission media. The dolphin model was in water ($c \approx 1500$ ms^{-1}) giving λ in the order of 15 mm whereas the bat ear in air gives λ in the order of 3 mm. Thus the accuracy needed to capture the geometry in the CT scan needs to be particulary high in the bat ear case. Figure 5.3 shows the orientation of the bat pinna within the mesh.

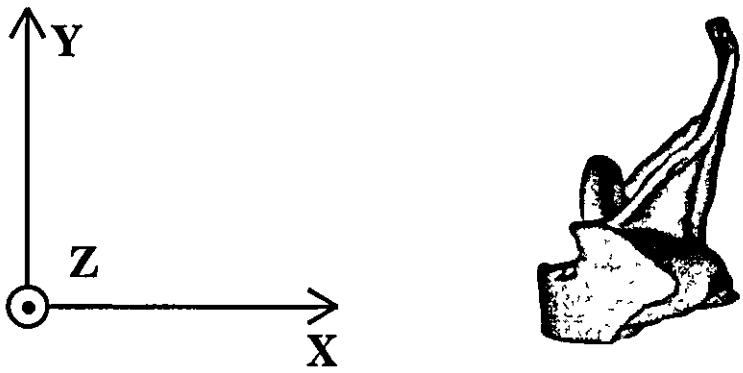

Figure 5.3. Coordinate definition of the TLM mesh and orientation of the bat pinna within it

The CT scanner used supplied data by means of 2D slices as it scans from top to bottom of the 3D object. Each slice was 1024 pixels wide (x) by 1024 deep (z) with each pixel being 18 μm wide. For scanning practicality the voxel size was decreased when measuring in the third dimension (y) to 72 μm giving 256 pixels along the height of the pinna. Hence the actual distance scanned was in each direction was 18.4 mm Figure 5.4(A) shows one slice of data as captured by the scanner which includes the x and z axis, scanner name in the bottom right hand corner and the holder in which the pinna was supported. By measuring pixels on the images it was found the absolute pinna size was 13.5 mm (750 pixels $\times$ 18 μm) across the maximum diameter of the base and 18.36 mm high (256 slices $\times$ 72 μm).

5.2.1 Data preprocessing

For implementation in a numerical modelling routine the image needed pre-processing to remove unwanted information, such as the sample holder used to hold the specimen. This was carried out with in an image processing package which was also used to remove noise from the image. The processed image can be compared in Figure 5.4(B) with the original (A). The image size was reduced using a bilinear method to 256 by 256 in the 2D slice to equalise the voxel size in all three cartesian directions (72 μm). This was also necessary to reduce the amount of computer memory used when modelling. Figure 5.5 graphically shows the image reduction with respect to the voxel size. The

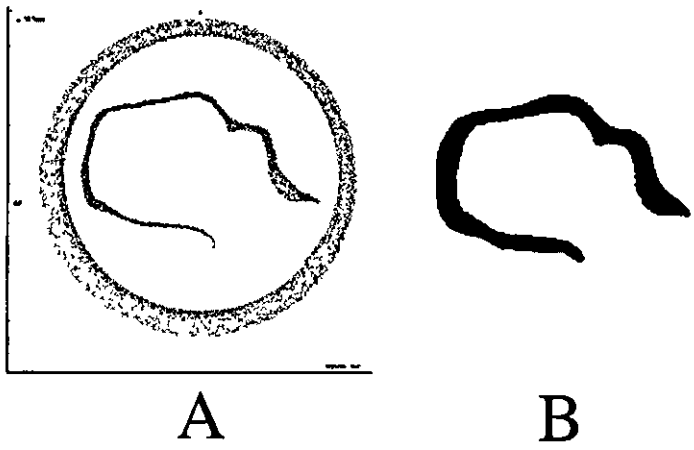

Figure 5.4: Image slices of the pinna before (A) and after image processing (B)

number of images in the third axis remains constant and with the original voxel size of 72 μm.

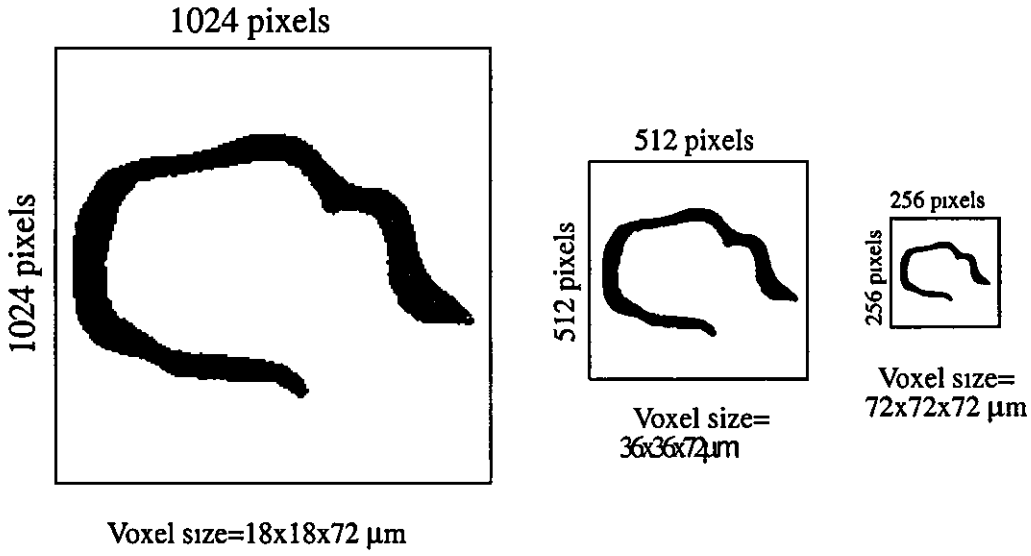

Figure 5.5: Image and voxel resizing for use in the TLM mesh

For 1:1 mapping between TLM nodes and this common voxel size (assuming 10 nodes per wavelength), this scale model would have an upper frequency (f_{max}) of: $\frac{331}{(10\times72\times10^{-6})}$ which is equal to 460 kHz which significantly exceeds the maximum frequency of 85 kHz required. The disadvantage of having a high acoustic cutoff frequency can be seen as this would lead to a computational mesh comprising of 16 8 million nodes which does not include free space to allow the absorbing boundaries conditions to perform as well as desired. Hence, there is a need to work to a smaller, more realistic maximum frequency.

5.3 TLM model construction

For increased computer processing efficiency the node described by El-Masri *et al.* [5.5] was used to model the pinna as the scattering matrix involved significantly less computation than the one by Portí and Morente [3.12]. This node was suitable as the node separation ($\Delta\ell$) in each cartesian direction was constant. A 3D mesh of free space nodes was generated before the geometry of the pinna was inserted. Each slice of data was imported into the TLM program via a portable pixel map (PPM) format where each pixel could easily be read and mapped to a node in the mesh. A flag was then set in the code depending if a part of the pinna was to be represented or not. For these results the pinna was assumed to be totally reflecting which simplified the scatter routine allowing the sound source to propagate and scatter from the pinna geometry. In the real world the pinna would absorb some of the sound due to the nature of the pinna material, however this cannot be currently modelled as the parameters needed to achieve these results are not available.

As was already mentioned the resolution of the pre-processed CT data exceeded what was necessary. Therefore it was possible to downsample the data further. A factor of 4 increased the node separation to 288μm (4$\times$72μm) but decreased the cutoff frequency to 114.58 kHz which is still higher than that utilised by the subject bat. This is also had the effect of reducing the number of nodes to 262,000, making the model more

practical.

From the absolute pinna size (13.5 mm $\times$ 18 36 mm) and minimum node separation, the new image size was calculated and mapped on to the TLM mesh. In the x and z directions the new image size was 47 nodes (13.5 mm $\div$ 288 μm) and in the y direction (height) it was 64 (18.36 mm $\div$ 288 μm).

The final mesh was 180 nodes in all 3 directions which allowed extra space on every side of the mesh for waves to become approximately planar as they reached the boundary which is a necessary criteria to allow them to absorb as effectively as possible. This created 5.8 millions nodes which computed successfully on a standard Pentium 4 desktop PC running Windows 2000 Professional with a 2.4 GHz processor and 1 GB of DDR RAM.

5.3.1 Excitation and near field data extraction

By applying the theory of reciprocity the pinna has been examined as a transmitter rather than receiver as its intended operation. This implies directionality patterns are theoretically identical for both transmission and reception. The modelling implementation was therefore much more practical as a simple point source could be used to excite the mesh, waves emerging from the pinna could then be sampled in the near field. The alternative approach would be to run a huge number of simulations, each using a plane wave impinging on the pinna from different angles.

Figure 5.6 details the mesh topology. The point of the grey arrow indicates the excitation point for a single point source, the inner dashed line is the encapsulating imaginary surface for the near field extrapolation and the outer continuous black line indicates the edge of the mesh and the absorbing boundaries. The source used in the major simulations was a simple sine wave mathematically described by: $f(t) = sin(\omega t)$ excited upon a single node. An alternative would have been to use a piston source over the whole area of the ear canal opening, although this may have proved erroneous in this

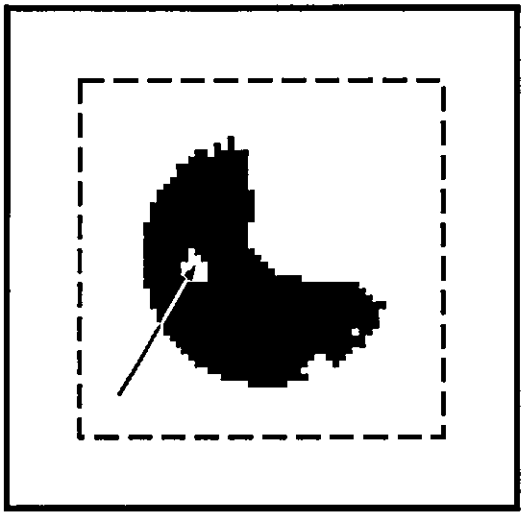

Figure 5.6: Point source injection location for the model

situation as can be seen in Figure 5.6 that the ear canal opening is not perfectly circular due to discretisation of the pinna.

Complex pressures along with the differential of this pressure were captured on every node on the imaginary surface and written to a data file for use in the near to far field extrapolation.

5.4 Near field results

A range of excitation frequencies were used in the simulations including that of the primary constant frequency component used by the bat when echolocating. Figure 5.7 shows a time snapshot the near field pressure for a simulation at 80 kHz where the darker areas represent higher pressure and vice versa for the lighter areas. The pinna geometry is defined by the constant grey colour order to aid visualisation.

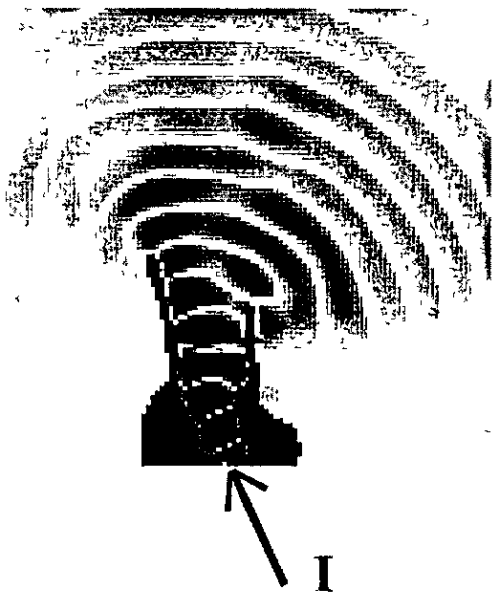

Figure 5.7: Example of the near field pressure from TLM simulations incorporating pinna geometry, excited with an 80 kHz point source sinusoid at point I

5.5 Far field directionality patterns and directionality index calculations

In order to compare the simulation output quantitively with the measurement and analytical results, a number of strategies were adopted. One particular problem is to visualise the results in 3 dimensions. In this section a number of the performance metrics explained earlier were simulated and measured, along with the graphical simulation results.

5.5.1 Far field data

Far-field data surfaces such as those in Figure 5.8 were constructed in MATLAB where the 3D rendering and rotation facilities gave an excellent means to visualise the patterns. Figure 5.8(A), (B) and (C) represent 55 kHz, 85 kHz and 110 kHz respectively and it can be seen how the size and number of sidelobes increases with frequency. This

is due to diffraction and interaction of a shorter wavelength of sound causing more interference regions as it scatters from smaller pinna features. The size and number of these sidelobes is important when trying to approximate the directionality index from known beamwidths as will be discussed. The area above the half power point of each pattern is shown by the deep red area on each lobe and on (C) it can be seen how the level of the sidelobe is such that it is over this point. This causes other problems which will be discussed. The effect of varying the frequency in the azimuthal axis appears negligible, however in the elevation axis the angle varies more significantly although it may not be obvious from the figure. Between Figure 5.8(A) and (C), the elevation angle varies by 18° and is not linear as at 85 kHz (half way between the two) the angle has only increased by 3°. This shows the steering that occurs at differing frequencies. Also not obvious from the diagram is how the sidelobe is steered by the tragus. From simple cone shapes with no tragus, the directionality patterns is symmetrical where as in this case, the side lobe appears off center.

The half power area of the patterns can also be visualised in 2D and it is this that is used to estimate the half power beamwidths. One traditional method of measuring this is to take slices through the pattern where the pressure is a maximum and measure the angle between the origin and the -3dB point. This proved extremely difficult in this case as the main lobe was of an unknown orientation so it was difficult to be certain that it was the correct angle being measured. The method used can be described from Figure 5.9 which shows a two dimensional profile of all the points on the surface above the half power threshold with the colour of each dot proportional to a pressure level. From this the beamwidth in azimuth and elevation can be approximated by measuring the maximum distances (representing an angle) in each axis.

5.5.2 Directionality index

Directionality has been calculated using two different approaches; the first used a traditional technique of measuring the azimuthal and elevatory beamwidth at the half power point and an approximate formula for calculating the directionality index. The second

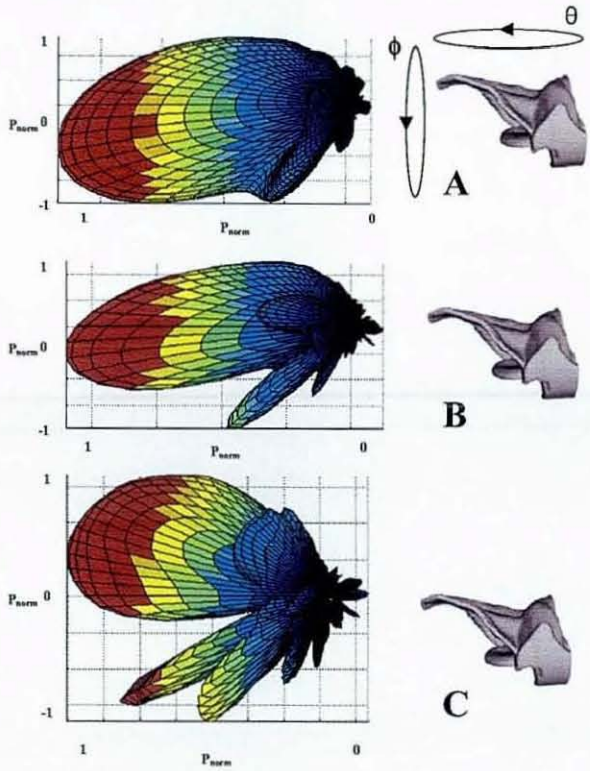

Figure 5.8: Far field directionality surfaces for the pinna of the Rufous Horseshoe bat excited sinusoidally at: 55 kHz (A), 85 kHz (B), and 110 kHz (C).

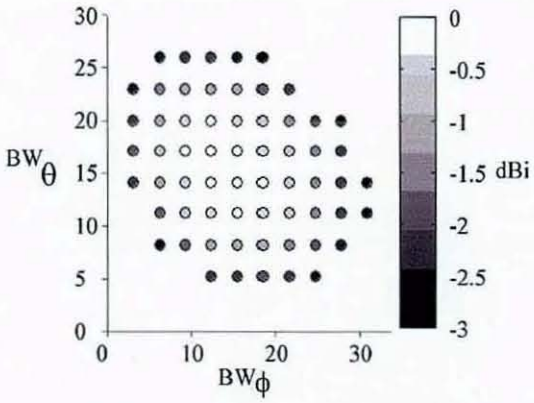

Figure 5.9: A profile of the half power region of the far field pattern at 85 kHz

uses the new technique as described in Chapter 4, referred to as the equal area method here.

F (kHz)	BW_θ	BW_ϕ	DI(a)	DI(b)	DI(c)
100	18	24	19.8	19.47	16.79
95	21	27	18.62	18.41	19.07
90	24	31	17.44	17.16	17.88
85	21	27	18.62	18.41	17.99
80	24	24	18.55	19.47	18.18
75	27	27	17.53	18.41	18.2
70	30	30	16.61	17.46	18.18
65	30	33	16.2	16.59	17.56
60	36	33	15.41	16.59	16.54
55	36	39	14.68	15.04	15.69
50	36	36	15.03	15.79	14.77
45	39	45	13.71	13.68	13.4
40	42	45	13.39	13.68	13.71
35	51	48	12.27	13.05	13.35

Table 5 2: Directionality of the pinna of the Rufous Horseshoe bat at various frequencies obtained using various approximations (DI(a): Table 4.2(A), DI(b): Table 4.2(C), DI(c): equal area method)

Table 5.2 shows for each frequency the azimuthal and elevatory half power beamwidth, directionality approximation using the elliptical method (DI(a), Table 4.2(A)), circular approximation (DI(b), Table 4.2(C)) based on the angle theta, and directionality index using the equal area method (DI(c)).

Figure 5.10 compares each value of directionality for each method implemented for each frequency. The three approximations agree well in most cases, simulations were performed over 100 kHz but these results were surprising and considered inaccurate. This was because sidelobe levels increase with frequency and the approximations are

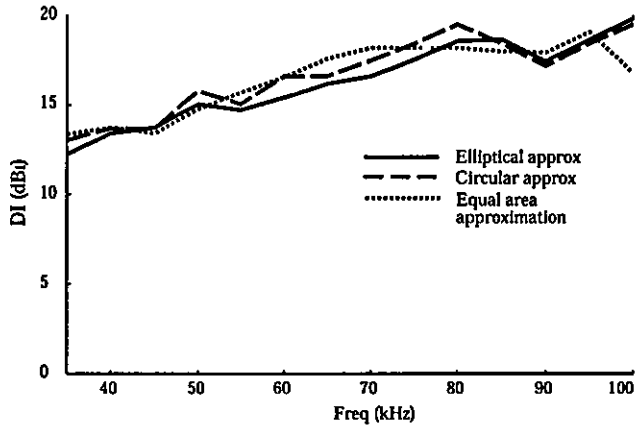

Figure 5.10: Graphical representation of the directionality of the pinna of the Rufous Horseshoe bat at different frequencies using different calculation methods

only valid with low sidelobes which is not the case at the frequencies in question. It could be suggested the equal area method alleviates the effects of sidelobes.

5.6 Measuring the directionality of physical pinna specimens

In order to validate the modelling results, physical measurements were taken from manufactured pinna of the target species. Artificial pinna were created using rapid prototyping (RP) manufacturing techniques from the 3D data. An experimental rig was manufactured to allow controlled rotation of a pinna for the calculation of directionality patterns.

5.6.1 3D data file format

The sliced data used in the TLM software for predicting the directionality patterns of the bat pinna was also available in a high definition 3D geometry object. The specific file format was VTK (Visualisation toolkit [5 6]), see Figure 5.11. VTK is an open source toolkit for three-dimensional computer graphics, image processing and visualization. It consists of a C++ core, but has interface layers/bindings enabling it to be

used from several other languages as well. VTK is a powerful and ever increasingly popular tool although is not yet interpretable by the Rapid Manufacturing Research Group (RMRG) of Loughborough University. The favoured file format used by RMRG are stereolithography (STL) files which are a popular, versatile and consistent 3D format used in many applications. ViSit [5.7] is another powerful graphics tool used for the visualisation of 3D images that can use distributed architectures so the processing of large, unstructured files can be processed in parallel. ViSit was developed by the Lawrence Livermore National Laboratory (LLNL) at the University of California in the USA and has the ability to convert between various file types including VTK and STL which was used in this project.

Figure 5 11: A 3D render from x-ray CT data of the pinna of the bat species in question

5.6.2 *Rapid prototyping*

Rapid prototyping is a term that generalises the manufacturing of objects directly from CAD data. Typically the object is built up in layers on a computer controlled machine that reacts to data in an image file. The theory is converse to that of traditional subtraction manufacturing (Computerised numerically controlled, CNC) associated with mills and lathes. The major advantage of RP over CNC is the ability to create complex geometries. However CNC is quicker, cheaper and often more accurate. There are several variants of RP such as selective laser sintering (SLS), fused deposition mod-

elling (FDM), laminated object manufacturing (LOM) and stereolithography apparatus (SLA) which was used to create the bat pinna in this project. Stereolithography is the most widely used rapid prototyping technology and works by building plastic parts or objects layer by layer by projecting a laser beam on to the surface of a vat of liquid photopolymer. This type of material originally developed for the printing and packaging industry quickly solidifies wherever the laser beam strikes the surface of the liquid. As one layer is completed, the object is lowered allowing the laser to trace the next level. The properties of the material are as such that each layer sticks to the next creating a complete object. The model used in this instance is the SLA 7000 series manufactured by 3D Systems and has the ability to create layers 0.0254 mm thick. The material used is Accura Bluestone which is a type of resin that gives added stiffness compared to many other polymers.

5.6.3 Measuring apparatus

Measurements were performed in a wide open space with attention paid to minimising reflections and reverberation. The pinna were scaled to offer a selection of measurement frequencies close to that of the actual emission range of the bat and that of the properties of the commercially available transducer to be used. The act of scaling objects due to a limited ability to measure or generate specific sound frequencies or space limitation is common practice. Companies such as S & V Solutions (http://www.svsolutions.com/) and Kirkegaard & Associates (http://www.kirkegaard.com/) build scale models of concert halls before they are built. Often measurements are taken from these models and compared with numerical results obtained from mathematical simulations representing the situation.

The pinna

The size of the pinna in the data files was of real size, given the limited frequency range of the transducer the manufactured pinna had to be scaled in size to accommodate the variation in frequency to be simulated.

Pinna	Frequency (kHz)	Scale
A	76-78	2.005348
B	78-80	1.955833
C	80-82	1.906318
D	82-84	1.856803
E	84-86	1.807289

Table 5 3: Frequencies and scaling factors of the manufactured pinna used in the measurement experiment

Table 5.3 shows the the scaling factors that were needed to represent a real frequency used by the bat given the transducer had a bandwidth of 2 kHz and a measured centre frequency of 40392 Hz. In simplistic terms, a pinna approximately tuned to the aforementioned transducer would need to be doubled in size to represent an approximate frequency of 80 kHz as used by the bat.

Frequencies; 75 kHz, 77.5 kHz, 80 kHz, 82.5 kHz, and 85 kHz were chosen as excitation frequencies for the experiment as they were close to the operating frequency of the bat. From the transducer specification and manufactured pinna selection, a further set of scaling factors were required that would determine the frequency the transducer would be driven at to replicate the frequency of the chosen species, these are summarised in Table5.4.

Required frequency (kHz)	Pinna scale	Centre frequency (kHz)	Transducer output (Hz)
75	2.005348	77	39394.7
77.5	2.005348	77	40641.33
80	1.955833	79	40903.29
82.5	1.856803	83	40122.73
85	1.807289	85	40392

Table 5.4: Transducer output frequencies given a pre-scaled manufactured pinna

The transducer output frequencies (TO) were determined from Equation 5.3 where RF is the required real frequency, PF is the predetermined frequency that the pinna was pre-scaled to, where PS is that actual pinna scale.

$$TO = \frac{RF + 2(79000 - PF)}{PS} \tag{5.3}$$

Measurement arrangement

A schematic diagram of the arrangement for the measurement apparatus can be seen in Figure 5.12. The dashed line indicates the alignment of the transmitter and receiver and angle ϕ and θ describe the azimuthal and elevatory angles of rotation respectively. Perhaps the most important point of interest is the centre of rotation which appears where the dashed line meets point of excitation on the actual apparatus. In this implementation, as with the numerical modelling, the line of reception was always directed towards the point of excitation, no matter the orientation of the pinna. This ensures the phase centre is consistent which is essential for accurate results for both phase and magnitude. Unlike the modelling arrangement, the pinna acted as the receiver as there was very little difference in the results whether it acted as a transmitter or receiver.

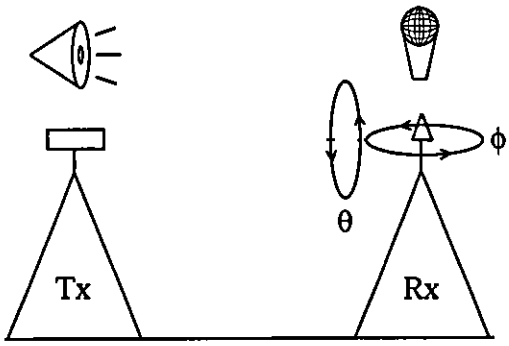

Figure 5.12: Schematic diagram of the measurement apparatus

Photos of the complete system can be seen in Figure 5.13. The main body of the device has been engineered from high density plastic for added stability and rotation in both

degrees of freedom is performed using servos controlled using software created for standard desktop PC's. In order to increase accuracy, laser levels were to used to align the transmitter and receiver. Two red laser beams were directed perpendicular to one another which can be seen in the figure and intersect at the centre of rotation, this has been highlighted with an added black and white cross on the image.

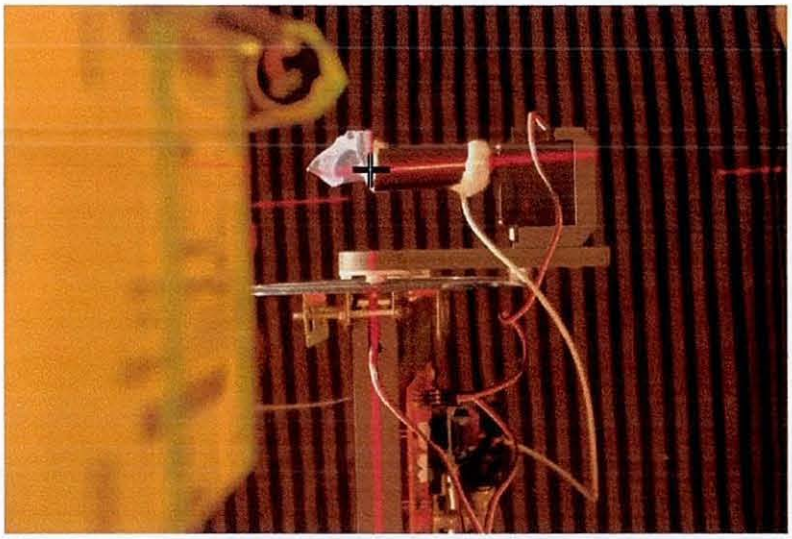

Figure 5.13: Photograph of the measurement apparatus

The transducers (see Figure 5.14(B)) were 40 kHz, standard, ultrasonic, piezoelectric, open type ones made by Murata or SANWA for example. The pair implemented in this experiments are a transmitting and receiving pair, model numbers SCS401T and SCS401R respectively with a tolerance of ± 1 kHz and beamwidth from the data sheet as 30°. All cables were rated at 50 Ω's as were the BNC connectors and connections on the signal analyser.

The signal analyser used in the experiments was a Hewlett Packard 35660a, this was used to both excite the transmitting transducer and process the receiver signal. Excitation was either by broadband chirp for examining the response of the transducer or a single frequency for examining the pinna directionality.

The transducer was coupled, (see Figure 5.14(A)) to the pinna by means of a large diameter plastic tube that encased the transducer housing which then fed a small diameter

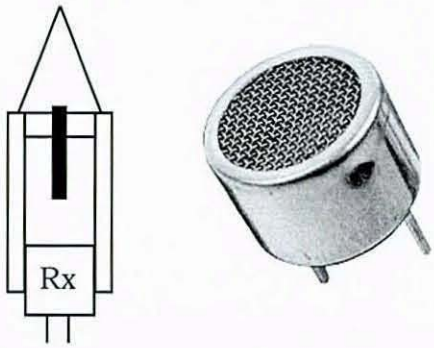

Figure 5.14: Transducer coupling configuration (A) and the experimental standard open type 40 kHz ultrasonic transducer (B)

copper tube (blacked out line on the diagram) that acted to direct incoming sound to the receiver. This was found to be the most successful method for matching the aperture of the transducer to that of the pinna which was considerably smaller. The diameter of the copper pipe was less than half a wavelength of sound at 85 kHz which meant only a plane wave would propagate down it.

Near and far field regions

The near field, or *Fresnel* zone is an area where propagating waves are not plane and may have phase shifts that do not vary linearly with distance from the phase centre. This suggests physical measurements taken within this region are unreliable and it is advantageous to measure in an area where wave propagation is constant. At a known distance from the source wave propagation is planar, this region is known as the far field zone or *Fraunhofer* region and begins when the pressure begins to decay as a function of $1/r$ where r is the distance from the radiator. This happens when the size of the radiator is small compared to this distance, r and it is assumed all propagating wave fronts arrive at the far field point in phase. The two regions can be seen in Figure 5.15 where the grey region is in the near field and the white region is in the far. In practice there is a transition region between the two zones although this will be over looked as

the measurements will be taken with the receiver situated substantially into the far field.

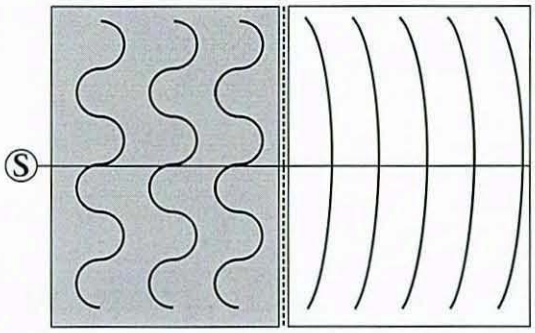

Figure 5.15: Near and far field propagation variations

Equation 5.4 shows how the distance of the near field region from a spherical transducer, N, is directly proportional to the maximum dimension (D) of the radiator and inversely proportional to the wavelength of sound used. The maximum dimension of the radiator in this case is taken as the largest diameter of the pinna aperture.

$$N = \frac{D^2}{4\lambda} \tag{5.4}$$

For Equation 5.4 to be valid the following identity must be true: $D > \lambda$. A frequency of 40 kHz has a wavelength of 8.3 mm which is significantly less than the a maximum pinna aperture which has been measured at 35 mm. For this given scenario the near field zone ends at approximately 74 mm away from the phase centre.

5.6.4 Results of the measurements

Five frequencies ranging from 75 kHz to 85 kHz were used to excite the pinna with two planes of interest chosen that would demonstrate the directionality and sidelobes of the directionality pattern. These planes can be seen in Figure 5.16 which also indicates the centre of rotation/phase centre as the intersection between the two lines of axis. It was important this matched that of the modelling method so like for like results were compared.

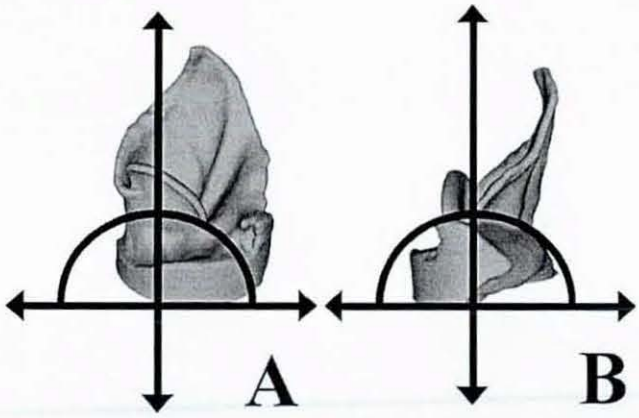

Figure 5.16: Location of the measurement plane used in the pinna experiment

Figure 5.17 shows the corresponding results for plane A in Figure 5.16 for (A) 80 kHz (Pinna A, Table5.4) and (B) 85 kHz (Pinna E, Table5.4) respectively, where the full lines are the measured results and the broken line are those from the numerical modelling routines. It can be seen there is very good agreement between the two methods which is also true at other experimental frequencies that are not shown in this thesis. Figure 5.18 shows the same information as the previous figure, for the plane described in Figure 5.16(B).

In order to compare the shape of the directionality pattern more easily, the measured data was shifted by a few degrees so both traces lined up. The largest shift was 4.86° which can be accounted to human error when attempting to arrange and prepare the experiment. There were several areas for error including the alignment of the transmitter and receiver and when attaching the pinna to the servo. The amount of shift is considered small and does not detract from the result similarities.

The largest discrepancy in the results is when the main beam is perpendicular to the line of reception, when angles tend to 0° and 180°. This is due to the difference in the modelled and measured physical arrangement where the numerical model contains only the pinna which is free to rotate in an infinite amount of free space. The measurement arrangement however, is quite different and has many surfaces that could lead to reflections. One significant and common area is around the base of the pinna where it

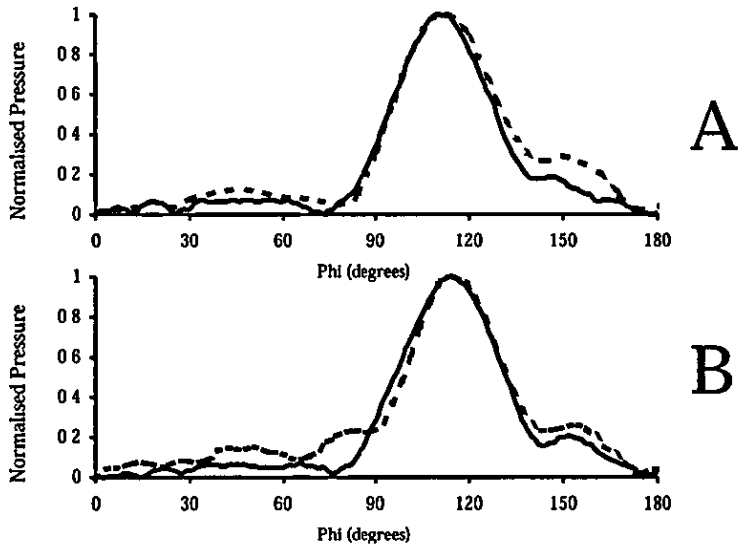

Figure 5.17: Pinna response determined from measured (solid line) and numerically modelled (dashed line) experiments incrementing ϕ (azimuthal) at A, 80 kHz and B, 85 kHz

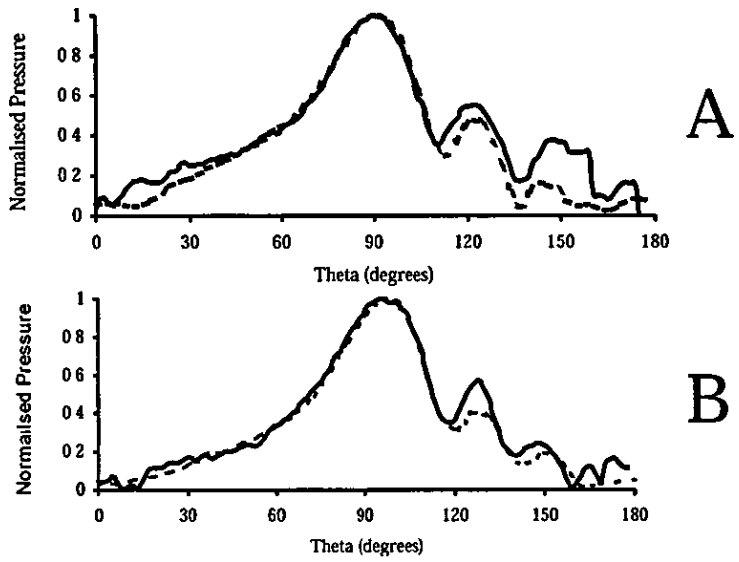

Figure 5.18: Pinna response determined from measured (solid line) and numerically modelled (dashed line) experiments incrementing θ (elevation) at A, 80 kHz and B, 85 kHz

is connected to the rig. Sound can creep around this base and reflect off the transducer housing and servo which could be detected by the receiver.

As with the modelled directionality patterns in this case, it is impractical to measure the beamwidth of the signal as the main beam is not on any predetermined line of axis. This means it cannot be guaranteed that the chosen points, -3dB for instance, are taken on the correct plane. The problem can be visualised by thinking of cutting a cylinder in half, if the line of cut is not parallel to the ends of the cylinder itself, i.e. the cross section is not spherical, angles could be over estimated as the radius is not common around the cut.

5.7 Modelled and measured results

Here comparisons are made between aperture approximations for both Obrist *et al.* [5.1] and the thesis specimen and the measured directionality index for both specimens. The estimated directionality index from the TLM models are also supplied for comparison at the relevant frequencies. The dimensions supplied for the pinna by Obrist *et al.* [5.1] are 18.5 mm by 15 mm where as the thesis pinna is slightly smaller at 15 mm by 12 mm, which can partly explain the variation in measured directionality index. There is good agreement between the modelled and measured directionality for the specimen of the thesis although the measured directionality by Obrist *et al.* [5.1] is considerably higher.

Table 5.5 compares the directionality of two different *Rhinolophus rouxii* pinna at 85 kHz estimated from various methods

5.8 Discussion

The TLM routine combined with the near to far field transformation technique has provided excellent visual representation of the beam patterns of the pinna in question. Moreover, they have been smooth, precise surfaces with very little noise on the main lobe allowing the pattern to be easily recognisable. The results have indicated varying directionality and sidelobe prominence with frequency as expected, although the calculated DI varies from the published, measured results.

Origin of data	Directionality (dBi)
Measured (Obrist *et al.* [5.1])	24
D(Rec) (Obrist *et al.* [5.1])	23.17
D(W) (Obrist *et al.* [5.1])	20.74
Measured (Thesis specimen)	18.14
D(Rec) (Thesis specimen)	21.7
D(W) (Thesis specimen)	19.71
TLM model (measured beamwidth)	approx 18.5
TLM model (equal area)	17.99

Table 5.5: Directionality index estimates for *Rhinolophus rouxii* pinna at 85 kHz determined using different methods

The measurements show an excellent agreement between themselves and the models.

References

[5.1] M. K. Obrist, M. B. Fenton, J. L. Eger, and P. A. Schlegel, "What ears do for bats: a comparative study of pinna sound pressure transformation in chiroptera," *Journal of Experimental Biology*, vol. 180, pp. 119–152, 1993.

[5.2] A. D. Pierce, *Acoustics*. New York: McGraw - Hill, 1981.

[5.3] L. L. Beranek, *Acoustics*. Electrical and Electronic Engineering Series, McGraw - Hill, 1954.

[5.4] A. Guppy and R. B. Coles, "Acoustical and neural aspects of hearing in the Australian gleaning bats, *Macroderma gigas* and *Nyctophilus gouldi*," *Journal of computational physiology*, vol. 162, no 5, pp. 653–668, 1988.

[5.5] S El-Masri, X. Pelorson, P. Saguet, and P. Badin, "Development of the transmission line matrix method in acoustic applications to higher modes in the vocal tract and other complex ducts," *International Journal of Numerical Modelling: Electronic Networks, Devices and Fields*, vol. 11, pp. 133–151, 1998.

[5.6] Kitware, "The visualization tookit." http://www.vtk org.

[5.7] L. L. N. Laboratory, "ViSit." http://www llnl.gov/visit/.

CHAPTER 6:
ARTIFICIAL PINNA

GIVEN the performance of bat echolocation, it is worth considering baffles as a receiver for use on synthetic robots or autonomous vehicles in the human world. As a means to understand their operating parameters and performance better, it is worth considering their shape in its most basic form; as a flat triangular patch or a more consistent 3D geometry that does not incorporate the physical features and detail of the real pinna. In this chapter the scattering of acoustical waves by simple geometrical shapes, such as a triangle and circular disc will be discussed. A candidate geometry is presented which is formed by wrapping an equilateral triangle around an imaginary cylinder to represent a pinna.

6.1 Scattering from geometrical shapes

Scattering is defined as the irregular reflection, refraction and diffraction of waves in many directions as they interact with obstacles in the path of propagation. The magnitude of this phenomena depends on the relationship between the wavelength of sound and the size of the scattering object. Analytical solutions to explain the scattering of waves by geometrical shapes have been derived from first principles and results for these discs appear in many books including "Electromagnetic and Acoustical Scattering by Simple Shapes" [6.1].

The experiment to model this scattering effect is arranged such that a broadband plane wave with normal angle of incidence upon a disc is used as an excitation source. In terms of a TLM routine, a plane wave excitation is used as described in Section 3.7.1,

using a variant subset of typical absorbing boundaries conditions meaning standing waves caused by the mesh are not measured. The mesh was 180 nodes in each cartesian direction with a node separation of 0 0001 m giving a maximum frequency of 300 kHz. In both cases the scatterers were assumed to be hard and lossless and were therefore given a +1 reflection coefficient to represent this in the TLM routine.

The circular disk has analytical scattering solutions ([6.1]) which enables the TLM model to be validated. From the validated TLM mesh, confidence can be given to the results for the triangular patch which can then be developed in to a 3D geometry that has a similar appearance to the real pinna.

6.1.1 The circular disc

The results shown in Figure 6.1(solid line) are from the aforementioned book and are for low frequency approximations to the problem. The graph shows the normalised magnitude of the signal against ka. a in the case of the coded TLM was 1.9 mm and 1 m in electromagnetic TLM and k is the wavenumber.

The result shown in Figure 6.1(dashed line) is calculated from TLM simulations. Only normalised pressure magnitude is shown as phase is notoriously difficult to calculate accurately due to its sensitivity at small time steps such as in these experiments. Time domain results were captured one node away from the disc on the centre axis and were then transformed using the Fast Fourier Transformation (FFT) routine in MS Excel and the normalised magnitude of the resultant complex pressure plotted ($| V |$).

Electromagnetic equivalent

A validation experiment was undertaken to compare the respective results of an acoustically hard and perfectly conducting circular disc. Figure 6.2 (dashed line) shows analytical results from [6.1] and those from commercially available software: MicroStipes (solid line).

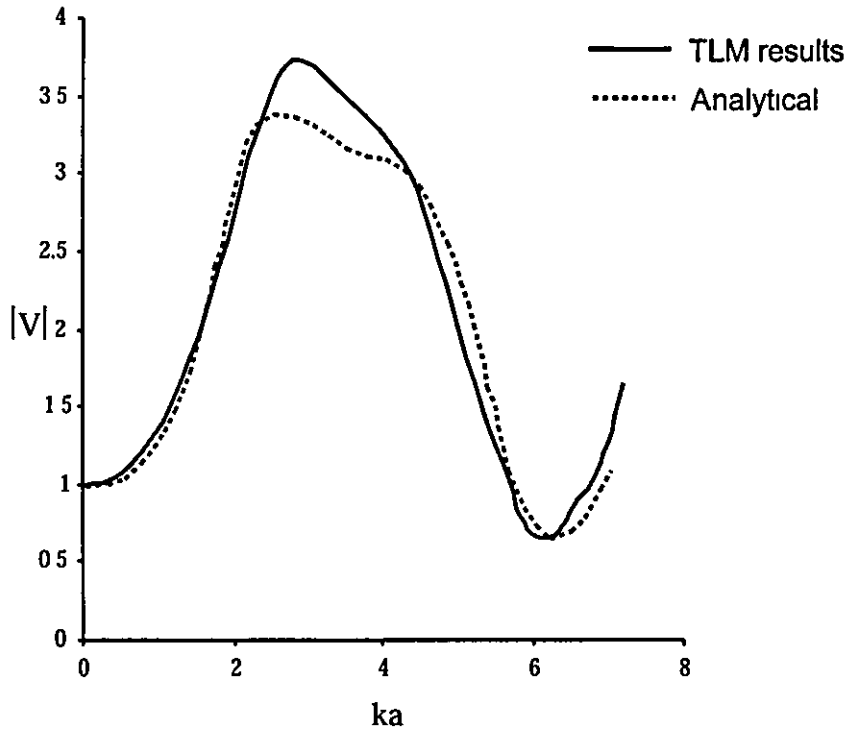

Figure 6.1: Analytical scattering from an acoustically hard disc

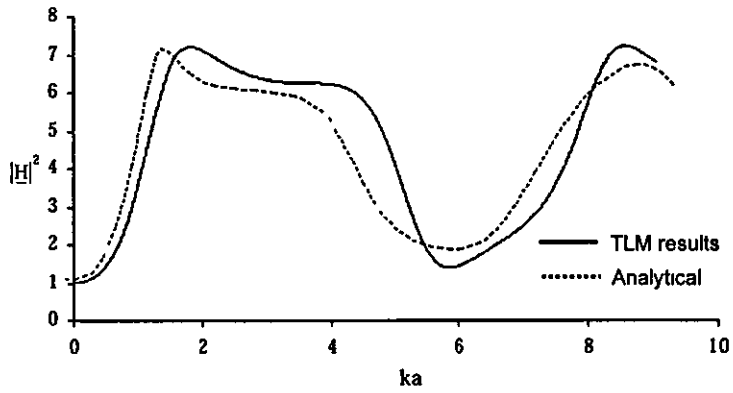

Figure 6 2: Electromagnetic scattering from a perfectly conducting disc

The results from the TLM software show good agreement with the analytical ones with the discrepancy down to dispersion in the TLM mesh and the discretised nature of the circular disc in a cubic mesh.

6.1.2 The equilateral triangle

An equilateral triangle replaced the circular disc in these experiments and a similar method was used to investigate the scattering. Figure 6.3 shows the measuring points for the coded TLM routine and the one implemented in Microstripes. The length of each side of the triangle was 2.8 mm in the coded TLM and 0.5 m in Microstripes.

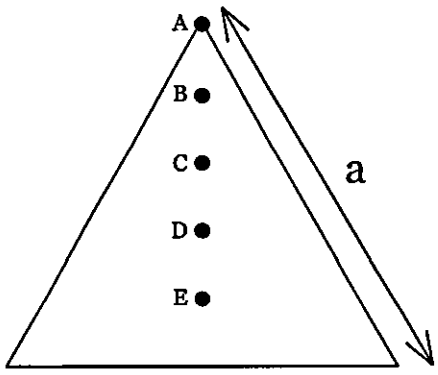

Figure 6.3: TLM measuring points for the equilateral triangular patch

Figure 6.4 shows the scattering from an acoustically hard triangular patch using acoustical TLM routines.

Figure 6.5 shows the scattering from a perfectly conducting triangular plate using MicroStripes. There are basic similarities in the results between the two methods although the coded version looks slightly noisier.

TLM is known to be erroneous around sharp edges such as the corner of a cube, these edges are enhanced when investigating single node thick structures as the disc and plate are in these experiments. Other errors in the results have been discussed such as dispersion in the mesh and discretising the geometry.

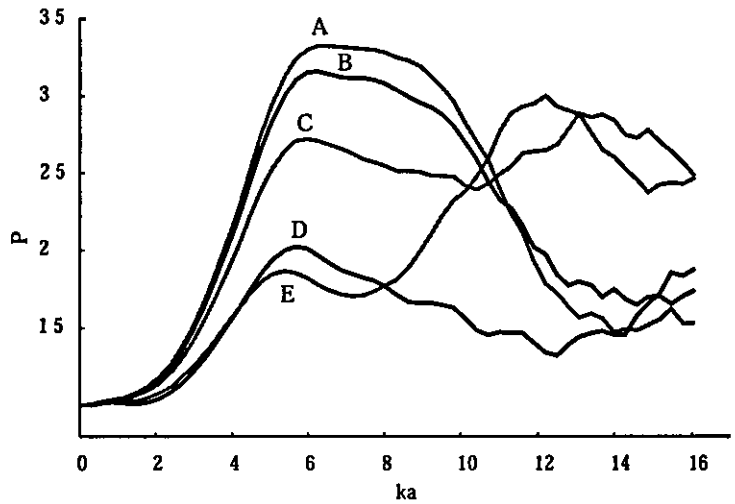

Figure 6.4: Acoustical scattering from a rigid triangular patch using acoustical TLM routines

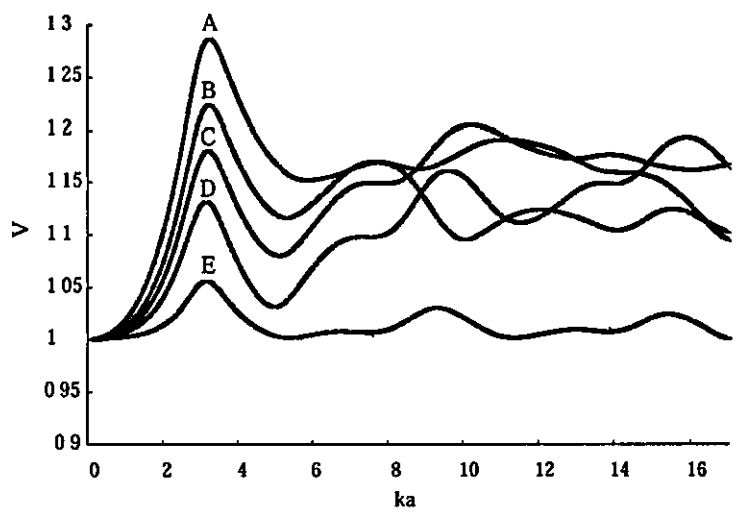

Figure 6.5: Electromagnetic scattering from a perfectly conducting triangular patch

6.1.3 The enclosed equilateral triangle

The pinna shape of the Rufous Horseshoe bat resembles a triangle wrapped around an imaginary cylinder with a circumference equal to the length of the base of the triangle. One example of this kind of shape can be seen in Figure 6.6. Two possible scenarios

regarding the shape of the geometry are to be considered:

1. The triangle is equilateral. This would give a tall, narrow geometry similar to the pinna of the Long Eared bat (*Plecotus auritus*) for instance.

2. The diameter of the base of the geometry is similar in length to that of the height. To achieve this, a shorter, wider triangle must be wrapped around a cylinder that would give a more accurate representation of the real pinna in this study. (See Appendix B for a pictorial representation of this)

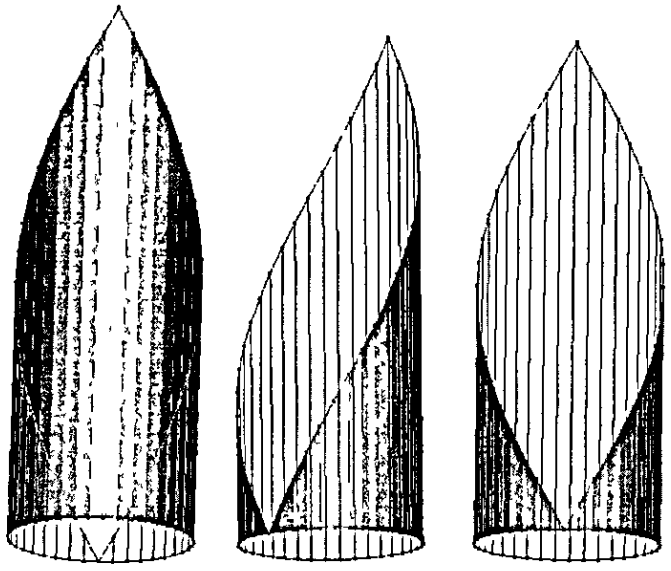

Figure 6.6. 3D CAD data of an equilateral triangle wrapped around an imaginary cylinder

For modelling purposes the enclosed triangle geometry has to be mapped to the TLM mesh in order to limit propagation in and around the geometry locality. There are at least two possible routines for achieving this; one is by creating the geometry in 3D CAD software and slicing the image into a series of 2D images that can be read and arranged by the software, the other is by way of geometrical algorithm. Figure 6.7 shows the theory of this geometrical algorithm as an assembly of a series of circles, starting with 360° (A in the image) of rotation, acting as the base of the geometry,

gradually decreasing to approximately 0° (B in the image) for the top. The number of increments required to progress from a full circle to the top of the geometry depends on the required height, this in turn controls the rate at which angle θ increases which determines how quickly the circles tends to 0°.

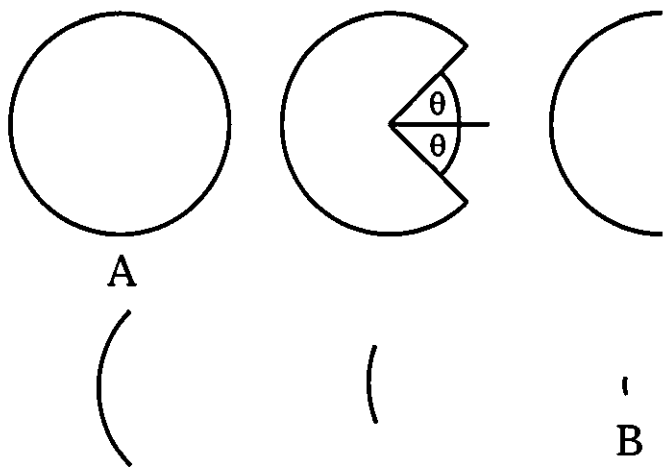

Figure 6.7: Graphical representation of the implementation of the enclosed triangle algorithm

The algorithm utilises two parameters; alpha (α) and beta (β). α describes the height of the geometry and is predefined by the user. For a TLM mesh the value given is the number of nodes meaning the actual length of the geometry is $\alpha \times \Delta\ell$. β is directly proportional to α and is a scaling factor that determines the radius of the base of the geometry. For an equilateral triangle of height α, the radius of the geometry can be seen in Equation 6.1. For a geometry of height α that is equal to the diameter of the base, the relationship between height and radius can be seen in Equation 6.2. A full derivation of this system is available in Appendix B.

$$\beta = \frac{\alpha}{\pi\sqrt{3}} \tag{6.1}$$

$$\beta = \frac{\alpha}{2} \tag{6.2}$$

The actual algorithm implements a polar coordinate system to create the segments of circles and convert them to cartesian coordinates for mapping on to a 3D TLM mesh.

$$P_x = \beta R \sin\theta \tag{6.3}$$

Equation 6.3 describes the x-coordinate (P_x) of the circle section at an angle (θ). R is the radius of the circle and β is as mentioned, the scaling factor for creating a pinna approximation with the desired dimensions.

Two values of α have been considered in this thesis which relate to the geometry as described in Equation 6.1 (an equilateral triangle); one which is equal to the height of the specimen species (18.4 mm), $\alpha = h$ and one which is half that of the pinna height $\alpha = h/2$. This geometry scenario has been chosen as it is formed from a basic geometrical shape, the equilateral triangle which has been investigated earlier in this thesis. To suggest an accurate alternative geometry for the pinna of the Rufous Horseshoe bat is beyond the scope of this thesis as the variation in possible shape formats is infinite. This section is intended to act as a brief introduction.

Modelling and results

A significant difference between the morphology of the pinna and synthetic geometry is the large open base on the geometry. A large circular baffle, equal in circumference to that of the length of side of the equilateral triangle was needed at this base to close off the end. This is in comparison to the real geometry where the injection point was inside the ear canal which measures a fraction of a wavelength in diameter. The injection point used in these simulations was in the centre of the enclosed triangle, one node from this circular baffle. The TLM mesh was 180 nodes in each cartesian direction and was excited in the center. The cut off frequency of the mesh was again, approximately 115 kHz.

6.1.4 Results

Here, both near and far field results are shown for the enclosed triangle experiment. Figure 6.8 shows near field propagation in one plane for the geometry at three different frequencies which demonstrates the off axis direction of the maximum pressure. The double beam at 115 kHz will be discussed later.

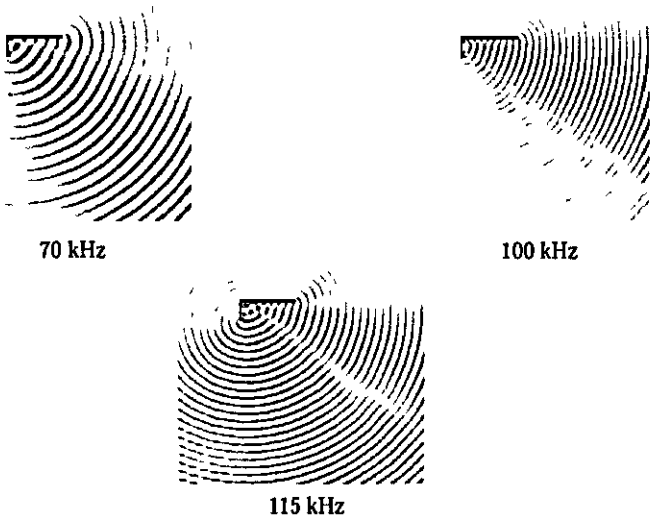

Figure 6 8: Near field propagation generated using the TLM method of the enclosed triangle at various frequencies performed in a 180 node, cubic mesh

An example of a far field directionality patterns from the enclosed equilateral triangle at 85 kHz can be seen in Figure 6.9 which shows the directionality and sidelobe. Only one frequency has been displayed as it is extremely difficult to take measurements directly from this type of surface although the deep maroon colour does indicate pressures above the half power points.

Figures 6.11 and 6.12 are the polar plot showing the elevatory 2D directionality for the geometry of $\alpha = h$ and $\alpha = h/2$ respectively. Beamwidths reduce with frequency in both cases and the size of sidelobe also varies with frequency as would be expected, although this is more obvious where $\alpha = h$. The beamwidth is particularly narrow at

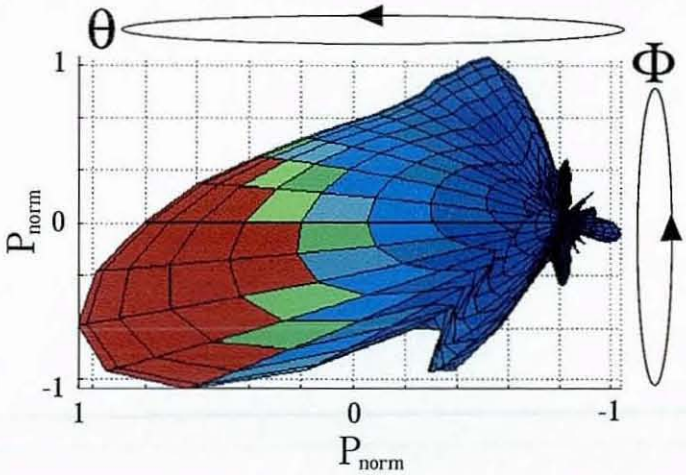

Figure 6.9: An example far field directionality surface at 85 kHz for the enclosed triangle

99 and 115 kHz in this plane although it will be seen how the azimuthal beamwidth is very wide giving a very interesting pattern.

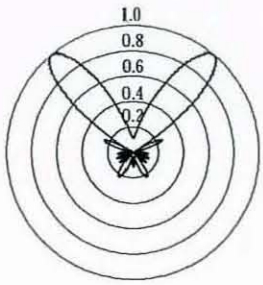

Figure 6.10: A weighted antenna array showing two equal main lobes in the directionality pattern

The most extraordinary result appears at 115 kHz where $\alpha = h/2$ where the sidelobe is in the same order of magnitude as the main lobe, in fact it is difficult to discriminate between the two. A further example of this kind of directionality can be seen in Figure 6.10 which shows the directionality of an adaptive antenna array that weights each individual elements with respect to the received signal. These are used in modern sonar systems where beam steering is required.

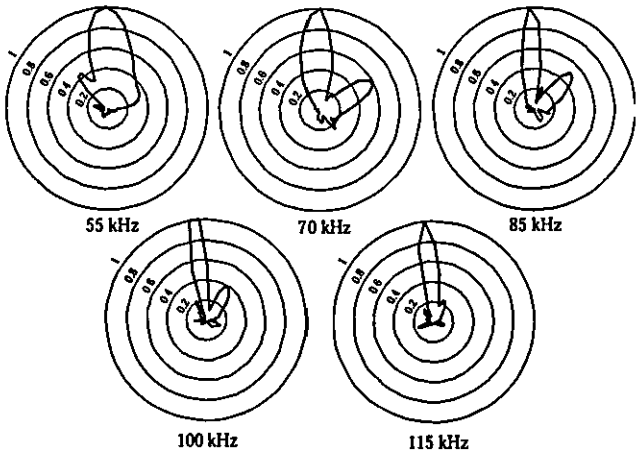

Figure 6.11: Normalised elevation polar plots for the enclosed equilateral triangle at various frequencies where $\alpha = h$

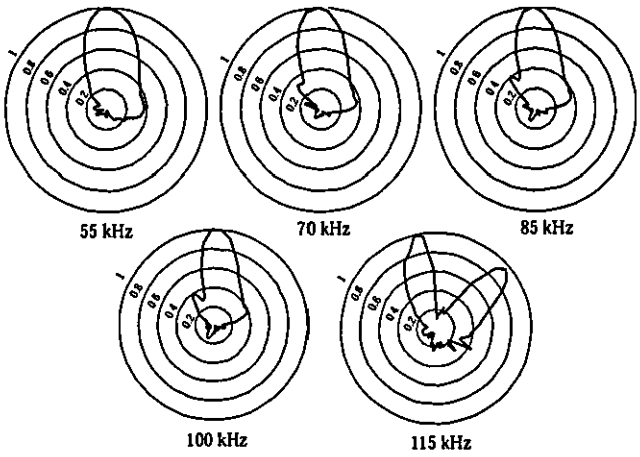

Figure 6.12: Normalised elevation polar plots for the enclosed equilateral triangle at various frequencies where $\alpha = h/2$

Figures 6.13 and 6.14 are the polar plot showing the azimuthal 2D directionality for the geometry where $\alpha = h$ and $\alpha = h/2$ respectively. All plots are symmetrical about the plane which cuts from front to back of the geometry where the points on the base of the triangle meet. Although the beam width do not vary linearly with frequency, it will be shown how actual directionality varies as expected.

Table 6.1 summarises the directionality indexes for the various frequencies and geome-

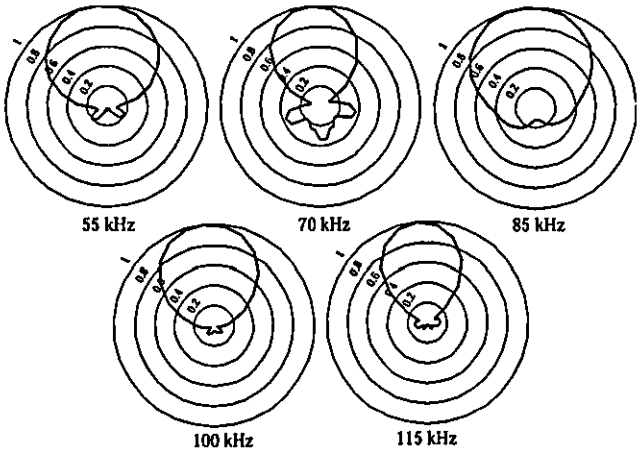

Figure 6.13: Normalised azimuthal polar plots for the enclosed equilateral triangle at various frequencies where $\alpha = h$

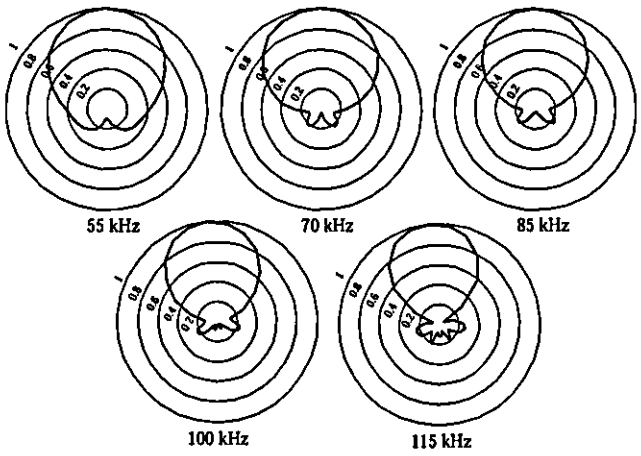

Figure 6 14: Normalised azimuthal polar plots for the enclosed equilateral triangle at various frequencies where $\alpha = h/2$

tries. Again, the basic approximation was taken from Table 4.2(A) which gives a useful indication to directionality if not completely accurate due to some patterns with relatively large sidelobes. The beamwidths were measured using the technique as described in the section relating to Figure 5.9. As would be expected, directionality increases with frequency, and there is a decrease in directionality as the aperture radius decreases as the overall geometry size goes down, this too is to be expected. Directionality can

also be compared with the modelled results. It can be seen how the α=h variation give similar values to that of the modelled results, where α=h/2 are quite different. This is slightly unexpected as the shape of this geometry is more similar to that of the real pinna than α=h.

Freq (kHz)→	55	70	85	100	115
α=h	15.29	16.2	16.72	18.03	18.43
α=h/2	13.9	14.9	15.29	17.2	18.1
Pinna model	15	17.5	18 3	18.3	N\A

Table 6.1: Table showing directionality indexes for two values of α at various frequencies

A further difference between directionality patterns of the real pinna and geometric shape is that of symmetry. Bat pinna are not symmetrical unlike the synthetic shapes generated and their directivities are asymmetrical as each individual ear has evolved for one particular side of the head in order for the bat to utilise biauralisation for target detection and localisation.

This initial idea is based on a simple triangle wrapped around an imaginary cylinder. It is not the most accurate representation of the pinna of the species of bat investigated in this thesis, but a means to stimulate ideas for possible future work, based on the algorithm described mathematically in Equation 6.2 which would appear to be a more accurate representation.

6.2 Discussion

Analytical and modelled results from the scattering circular disc compare well, both in acoustics and electromagnetics. Results from the equilateral triangle compare well between commercial software for the electromagnetic case and for the acoustical TLM code. The enclosed triangle results look similar to that of the pinna and show a prominent sidelobe that leads to the question over the tragus and how it affects the sidelobe

and reception. It would appear the simple geometry proposed could imitate the performance of a real (complex) ear, however there are some differences that have not been accounted for such as biauralisation.

References

[6.1] J. J. Bowman, T. B. A. Senior, and P. L. E. Uslenghi, *Electromagnetic and acoustical scattering by simple shapes.* Amsterdam: North-Holland Publishing Company, 1969.

CHAPTER 7:
CONCLUSION AND FURTHER WORK

THE aim of work in this thesis was to develop an understanding of the pinna of bats as a receiving acoustical horn. The mathematical modelling tool used to achieve this was the TLM method which has been fully validated and used successfully in the acoustic domain. One particular goal has been the examination of the far field properties of the pinna. The work has been partly assisted by the EU funded CIRCE project partners who have provided data and discussion during the study.

7.1 Contribution of this thesis

7.1.1 Bioacoustics

The modelling results obtained in this thesis are unique to the project even though acoustical TLM is well established. Indeed, the only other mathematical modelling of bat ear morphology has been carried out within the CIRCE project who implemented the FEA method. Near field TLM data has been thoroughly verified via far field extrapolation methods for use with non-standard radiators such as the bat pinna. Directionality polar patterns calculated using TLM have been verified with measurements in 2 dimensions in both the azimuthal and elevatory planes with discrepancies accounted to the difference between the modelled space and physical apparatus set up.

The relatively high directionality of the pinna of the Rufous Horseshoe bat suggests that the animal can achieve a high level of image resolution - an essential feature in the detection of small and highly mobile targets. The relatively high directionality found also emphasises the bat's need to pan and tilt the pinna whilst echolocating.

'Equal area' method for estimating directionality

From investigating several different varieties of antennae and horns a novel method has been developed for calculating directionality index which has been termed the equal area method. By studying the definition of directionality index, a numerical method has been employed that does not rely on the calculation or measurement of the half power beamwidth. The equal area method is particulary applicable to biomimetic antenna since it allows a good estimation of directionality to be produced without a prior knowledge of the main radiation direction. This thesis has validated the technique by sampling analytical expressions with known beamwidth. The method also has application to antennas in the electromagnetic domain, although these are not considered in this thesis.

7.1.2 Accurate modelling of the pinna

A simple approach to determining the directionality of the pinna is in terms of the aperture size. From the pinna dimension measurements made by Obrist *et al.* [5.1], the directionality of the pinna has been estimated using the theory of a radiating aperture and compared with the measured values. It has been shown for the Rufous Horseshoe that this is a reasonable approximation to the measured specimen in the reference.

There have been two approximation methods considered for estimating the directionality of the pinna from the TLM devised 3D far field data sets. The standard method using half power beamwidths appears to over estimate the directionality by 0.36 dBi compared to the measured value. The new, equal area method improves the estimation and reduces the overestimate to 0.15 dBi. This method performs better because the beam pattern is irregular and has no natural axial boresight. From the results it has been proven that TLM implemented in conjunction with the Helmholtz-Kirchhoff integral is a viable and accurate technique in bioacoustics. This thesis has contributed to improving the accuracy of the technique which paves the way for exploring the pinna shapes numerically for designing artificial baffles.

7.1.3 Artificial baffle structures

A novel development discussed in this thesis is the possibility to produce viable 'artificial ears' by considering simple 3D geometrical shapes. This work has lead to a geometry being proposed which consists of a flat triangular patch that has been wrapped around an imaginary cylinder giving it a similar appearance to that of the bat pinna. The aim of this is to develop a simplistic shape for uses in synthetic sonar systems based on the bat pinna. Similar features can be seen such as the off axis beam direction and sidelobes. It should be pointed out that this work is a preliminary study which does not consider the bat's tragus or any biauralisation effects.

7.2 Suggestions for further work

Possible further areas of investigation involve the development of the TLM method as a numerical modelling technique and using the method to investigate a greater range of pinnae. The following section suggests specific avenues of further work that would expand the current thesis and enhance knowledge of biosonar systems.

7.2.1 Source modelling

Improved realism of the model could be achieved several ways including the adaptation of source type and implementation and modelling a realistic pinna material. The actual tympanic membrane of the animal is currently approximated by a point source in the model. A true representation would involve including acousto-mechanical coupling from the sound wave to the vibrating membrane and the inner ear.

7.2.2 Time domain analysis

In order to make the model more representative it would be possible to inject the bats call signal into the mesh as a far field plane wave. The time domain signal received

at the tympanic membrane could then be studied for various discrete incident angles. This thesis has almost entirely considered frequency domain signals devised via FFT. However, it is acknowledged that in doing this some data has been lost. It is entirely feasible that the bat is processing in the time domain and this should also be modelled.

7.2.3 Pinna material modelling

Currently the pinna is assumed to be acoustically hard and perfectly reflecting, however real flesh, cartilage, and other tissue may not be. In reality the pinna would absorb some of the received sound depending on its frequency content which could alter the directionality patterns or gain. The modelling results in the thesis are still useful as the material used to recreate the pinna is consistent with the current modelling conditions and prototype measurements.

7.2.4 Dual ear model

A obvious yet highly complex adaptation of modelling a single pinna would be to model the left and right pair of pinnae and examine the biauralisation effects. By using a reflected signal from a target, IID and ITD could be modelled and compared to measured quantification as performed by Obrist *et al.* [5.1]. This would allow diffraction and scattering between the two pinnae to be examined for any effects they might have on the incoming signal and target detection processes. The logical progression from this would be to model the whole head in terms of emission and reception from targets placed in the model space. This model would be very challenging to create, optimise and simulate due to the huge amount of nodes that would need to be incorporated. Also there is no data set currently available of a whole bat head that is of sufficient resolution to carry out the study.

7.2.5 Moving boundary problems

With the development of moving TLM models, moving pinna could be examined and yet again enhance work carried out on investigating the tracking of moving targets. With more understanding of how each pinna moves during echolocating, biauralisation models could investigate the interaction between the directionality pattern of each pinna. Determining whether the patterns overlap could further enhance understanding of localisation as bat driven tracking algorithms could be developed to detect targets. Moving targets such as moths flapping their wings are sources of Doppler shift and some bats are known to make use of it.

7.2.6 Other bat species

Modelling other species of bat would enable a more complete understanding of the relationship between the echolocation calls emitted and the receiver properties of the pinna. Investigating different pinna-frequency relationships could enable the determination of an optimum shape for efficient, high resolution scanning, possibly for imaging in the target space. An issue to be resolved is that of explaining pinna with a measured directionality significantly higher than traditional approximations. Various specimens from Table 5.1 have a much higher directionality than the estimated value from aperture size and further modelling of these pinna may explain why this is so.

7.3 Closing remarks

The underlying motivation for this work is for the development of synthetic systems utilising SONAR type navigation methods. Engineers and scientists need to understand why biosonar systems are so efficient and accurate as a first logical step towards their synthesis. Numerical modelling is proving to be an invaluable tool as many experiments are either not feasible or not acceptable on live animals. The technical area addressed by this thesis has been the investigation into the pinna as an acoustic receiver in order to

assist in the decision of whether baffle shape like pinnae could be utilised on a human made echolocation systems.

AUTHOR'S PUBLICATIONS

A number of publications have resulted from the work in this thesis. These are as follows:

[1] G. Leonard and J. A. Flint, "TLM modelling of a bat pinna," in *Proceedings of Prep'2004*, (University of Hertfordshire, UK), pp. 111–112, 5–7 April 2004.

[2] J. A. Flint, A. D. Goodson, G. Leonard, and S. C. Pomeroy, "Transmission line modelling of the Harbour Porpoise (Phocoena phocoena) melon," *Journal of Acoustical Society of India*, vol. 30, no. 3-4, pp. 294–297, 2002.

[3] G. Leonard, J. A. Flint, and R. Muller, "On the directivity of the pinnae of the Rufous Horseshoe bat *(Rhinolophus rouxii)*," in *Symposium on Bio-Sonar Systems and Bio-Acoustics*, Institute of Acoustics, 2004.

[4] M. Garg, G. Leonard, S. A. Dible, J. A. Flint, and S. Datta, "TLM modelling of mammal vocal and auditory systems," in *First International Workshop on Generalised Applications of TLM and Related Techniques*, (Pegagocial University, Poland), 2004.

[5] G. Leonard and J. A. Flint, "Analysis of a geometrical approximation to the pinna of the Rufous Horseshoe bat (Rhinolophus rouxii)," in *NSA 2005*, Acoustical Society of India, December 2005.

[6] G. Farmer, J. A. Flint, and G. Leonard, "Measurements of a biomimetic antenna," *European Conference on Antennas and Propagation*, p. In press, November 2006.

APPENDIX A: PORTÍ AND MORENTE [A.1] NODE PARAMETERS

This appendix describes the mathematical parameters for the aforementioned node. It is important to reiterate the versatility of this specific method as the node can function with varying node separation in any cartesian direction. These varying lengths are shown by the different subscripts representing each direction.

$$a_x = \frac{1}{2}\frac{Z_x - 2}{Z_x + 2} - \frac{1}{2}\frac{Y + 2}{Y + 6} \tag{A.1}$$

$$b_x = -\frac{1}{2}\frac{Z_x - 2}{Z_x + 2} - \frac{1}{2}\frac{Y + 2}{Y + 6} \tag{A.2}$$

$$c = d = \frac{2}{6 + Y} \tag{A.3}$$

$$e_x = \frac{2Z_x}{2 + Z_x} \tag{A.4}$$

$$f = \frac{2Y}{Y + 6} \tag{A.5}$$

$$g = \frac{Y - 6}{Y + 6} \tag{A.6}$$

$$h_x = \frac{2}{Z_x + 2} \tag{A.7}$$

$$\jmath_x = \frac{2 - Z_x}{2 + Z_x} \tag{A.8}$$

The coefficients in the scatting matrix are found and must incorporate the 3D equivalents of Section 3.3.2; the acoustic analogy and energy conservation conditions.

In order to find the above coefficients the following properties are required; characteristic impedance (Z_o) and admittance (Y_o), impedance ($Z_{x/y/z}$) of each link line in a particular direction and general admittance (Y).

Equation A.9 describes the characteristic impedance and admittance of the transmission line in terms of the minimum nodal separation ($\Delta\ell$) and acoustical impedance (Z_A) of the transmission medium, in the case of air $410\frac{Ns}{m^3}$.

$$Y_o = \frac{1}{Z_o} = \frac{1}{Z_A\sqrt{3}\Delta\ell} \tag{A.9}$$

Equation A.10 describes the non-varying admittance of the transmission line in terms of characteristic admittance (Y_o), time step (Δt) and compressibility (σ) which is 7 63 $\times$ $10^{-6}\frac{m^2}{N}$ in air.

$$Y = \frac{2\sigma}{Y_o\Delta t} \tag{A.10}$$

Equation A.11 describes the impedance of the transmission line in each cartesian direction where $\Delta\ell$ if the node separation for the particular cartesian direction, ρ is the the density, $1.2\frac{kg}{m^3}$ in air, Z_o is the characteristic impedance and Δt is the time step.

$$Z_x = \frac{2(\Delta\ell_x)^2\rho}{Z_o\Delta t} \tag{A.11}$$

References

[A.1] J. A. Portí and J. A. Morente, "A three-dimentional symmetrical condensed TLM node for acoustics," *Journal of Sound and Vibration*, vol. 241, no. 2, pp. 207–222, 2001.

APPENDIX B: SYNTHETIC PINNA

The geometrical algorithm for synthetic pinna generation

This appendix details the derivation of the geometrical algorithm used in section 6.1.3 for generating shapes that represent the pinna. From a user defined height α, it is necessary to calculate the radius of the circles (seen in Figure 6.7) used to build the actual shape for use in a TLM mesh. It is the radius:height ($\beta : \alpha$) ratio that is a basic quantitative description of the desired geometry; for instance, it could be tall and thin or short and wide.

Pseudo code

The appendix begins with some pseudo code that demonstrates the implementation of the algorithm. In short it determines how much of the circle segment is to be mapped to a TLM mesh for a given height and shape characterisation. The actions of each line is then described below.

1: `for n is 0 to` α

2: `...for theta is 0 to` 2π

3: `.....if (theta<`2π`-n`$2\pi/\alpha$`)or(theta>=0+n`$2\pi/\alpha$`)`

4: `.....`$px = \beta \times R_x \sin\theta$

5: `.....`$py = \beta \times R_y \sin\theta$

Line 1 is responsible for building the actual geometry and is limited by the desired height as specified by the user. Line 2 increments theta from zero to a full 360° of the circle, where line 3 limits the segment of the circle to be created. Line 3 initialises

the segment decay at point x in Figure 6.7 (the reference point) and is responsible for gradually decaying the amount of the circle that is mapped to the mesh. The circles are mapped to a 3D mesh with coordinates (n, px, py) depending if the comparison statement in line 3 is true or false. For example, when $n = 0$, a complete circle is mapped and when $n = \alpha$, none of the circle is mapped. The radius of the circle (R), in lines 4 and 5 is preceded by a factor β which is to be derived and dependent on the desired final geometrical shape.

Deriving β

Beta is a coefficient used to control the radius of the circles being created. Firstly, Equation 6.1 is derived which describes a value of beta for an equilateral triangle wrapped around a cone (Figure B.1(A)) and secondly, Equation 6.2 is derived which creates a geometry where height is equal to the diameter of the circular base (Figure B.1(B)).

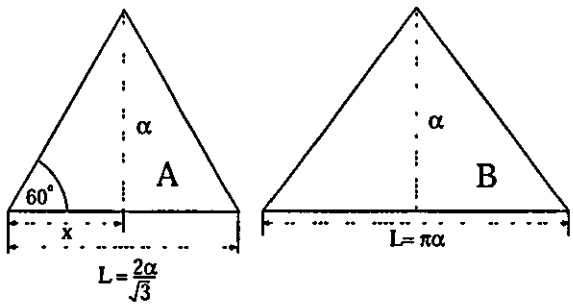

Figure 8.1: 3D geometries showing two enclosed triangles of different form and dimension

The wrapped around, equilateral triangle

From Figure B.1(A), x equals: $\alpha\ \sqrt{3}$. L is the length of one side of the equilateral triangle and is simply equal to $2x$. If L is also the circumference of the base of the geometry, then Ł $=\pi d = 2\alpha/\pi\sqrt{3}$. From a simple rearrangement, it can be seen that the radius coefficient for use in the algorithm , β is equal to $\alpha/\pi\sqrt{3}$.

Geometry where height equals circular base diameter

The derivation of the geometry in Figure B.1 is more simple than previous as the required shape is independent of the length of the triangle side, simply because the required geometry form has not requested any reference to the side length. With the stipulated geometrical form being $\alpha = d$, where d is the geometry base diameter, $\beta = alpha/2$ as the radius is simply equal to half the diameter. For this to be true, the triangle base has to be π times bigger than the height.